



**COMPARISON OF CLIMATOLOGICAL OPTICAL TURBULENCE PROFILES  
TO STANDARD, STATISTICAL AND NUMERICAL MODELS USING  
HELEEOS**

THESIS

Lieseбет E. Gravley, Civilian

AFIT/GAP/ENP/06-06

**DEPARTMENT OF THE AIR FORCE  
AIR UNIVERSITY**

**AIR FORCE INSTITUTE OF TECHNOLOGY**

**Wright-Patterson Air Force Base, Ohio**

APPROVED FOR PUBLIC RELEASE; DISTRIBUTION UNLIMITED

The views expressed in this thesis are those of the author and do not reflect the official policy or position of the United States Air Force, Department of Defense, or the United States Government.

AFIT/GAP/ENP/06-06

COMPARISON OF CLIMATOLOGICAL OPTICAL TURBULENCE PROFILES TO  
STANDARD, STATISTICAL AND NUMERICAL MODELS USING  
HELEEOS

THESIS

Presented to the Faculty

Department of Engineering Physics

Graduate School of Engineering and Management

Air Force Institute of Technology

Air University

Air Education and Training Command

In Partial Fulfillment of the Requirements for the

Degree of Master of Science (Applied Physics)

Lieseбет E. Gravley, BA

Civilian

March 2006

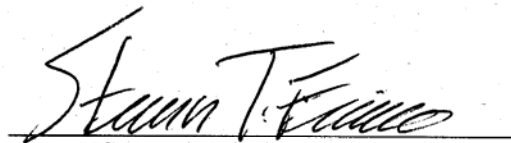
APPROVED FOR PUBLIC RELEASE; DISTRIBUTION UNLIMITED

AFIT/GAP/ENP/06-06

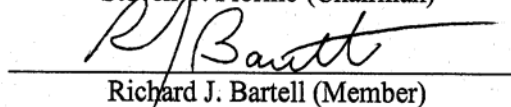
COMPARISON OF CLIMATOLOGICAL OPTICAL TURBULENCE PROFILES TO  
STANDARD, STATISTICAL AND NUMERICAL MODELS USING  
HELEEOS

Liesebet E. Gravley, BA  
Civilian

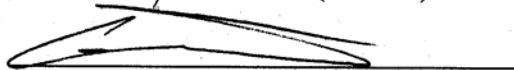
Approved:



Steven T. Fiorino (Chairman)



Richard J. Bartell (Member)



Glen P. Perram (Member)

14 MAR 06  
date

14 MAR 06  
date

14 MAR 06  
date

### **Abstract**

Optical turbulence within earth's atmosphere plays a significant role in electromagnetic radiation propagation from a high energy laser. The index of refraction structure constant,  $C_n^2$ , characterizes turbulent spatial fluctuations due to temperature gradients. These changes in the index of refraction affect the intensity of the laser wave front on its intended target. It is important to characterize this parameter throughout the atmosphere, the boundary layer and above, for its applications regarding the Airborne Laser (ABL) and the Advanced Tactical Laser (ATL). There are several ways to obtain values of optical turbulence, including standard and statistical models, physically-based numerical models, and climatological compilations of observed values. The purpose of this paper is to quantifiably compare standard, statistical, and numerical models of  $C_n^2$  to climatological values using the High Energy Laser End-to-End Operational Simulation (HELEEOS), to determine whether or not each model will yield values similar to that of actual measured optical turbulence data. The study shows that HELEEOS is a powerful tool in atmospheric optical turbulence prediction, not only because it has the capability to use standard optical turbulence profiles like Hufnagel-Valley 5/7 (HV 5/7), but it can also incorporate correlated, climatologically-derived turbulence profiles—a technique specifically developed for HELEEOS. The comparative analysis in this research appears to validate the HELEEOS method for correlating climatological  $C_n^2$  to other meteorological parameters. Worldwide dwell time estimates vary more than 4 s for tactical low altitude oblique scenarios using this new technique compared to HV 5/7.

## Acknowledgments

First and foremost, I'd like to thank both my advisor, Lt. Col. Fiorino and Rick Bartell for all of the help and insight that they have provided. I also want to thank Mark Houle and Lt. Col. Fiorino for getting me this job and thesis topic, and Dr. Perram for providing the money after a rough 2 months of unemployment. Next, I would like to thank Dr. Eric Magee for providing information and help with the statistical model and Sara Adair for her help with DEEST. A big thanks goes to the guys who programmed HELEEOS, especially Matt, who wrote so many Matlab scripts that were invaluable to me. I also want to recognize all of my teachers throughout the years, thank you for making me the student I am today.

I really want to thank my family, my brothers, and especially my mom and dad for supporting me both financially and emotionally through all of the stressful times this past year and a half. Last, but not least, I want to thank the best housemates ever, even though they were neglected most of the time. I love you, Tigerlily and Mr. Feynman!

Lieseбет E. Gravley

## Table of Contents

	Page
Abstract.....	iv
Acknowledgments.....	v
List of Figures.....	viii
List of Tables .....	xv
I. Introduction .....	1
1.1 Significance of the Problem.....	1
1.2 Problem Statement .....	3
1.3 Research Objectives.....	4
1.4 Organizational Overview .....	5
II. Background and Literature Review.....	8
2.1 Chapter Overview .....	8
2.2 Turbulence .....	8
2.3 Optical Turbulence.....	10
2.4 Thermosondes .....	11
2.5 Effects of Optical Turbulence .....	13
2.6 Optical Turbulence Models.....	18
2.6.1 <i>Hufnagel-Valley 5/7</i> .....	19
2.6.2 <i>CLEAR I</i> .....	20
2.6.3 <i>Statistical Model ATMtools</i> .....	21
2.6.4 <i>Directed Energy Environmental Simulation Tool</i> .....	23
2.6.4.1 <i>DEEST Boundary Layer Models</i> .....	24
2.6.4.2 <i>DEEST Upper Air Models</i> .....	26
2.6.5 <i>Navy Surface Layer Optical Turbulence</i> .....	26
2.7 High Energy Laser End-to-End Operational Simulation .....	28
III. Data and Methodology.....	33
3.1 Chapter Overview .....	33
3.2 Data .....	34
3.3 Methodology .....	38
IV. Results and Analysis.....	43
4.1 Chapter Overview .....	43
4.2 Validation of the HELEEOS Climatological Profile .....	43
4.3 Standard vs. Climatological models.....	48
4.4 Statistical vs. Climatological Models.....	53
4.5 Numerically Derived vs. Climatological Models .....	59
4.6 Air Force Applications.....	64
V. Conclusions and Recommendations .....	74

5.1 Conclusions .....	74
5.2 Recommendations .....	76
Appendix .....	79
Bibliography .....	96
Vita .....	99

## List of Figures

Figure	Page
<p>1. The difference in required dwell time between Hufnagel-Valley 5/7 and the climatological profiles for the 10<sup>th</sup> percentile relative humidity and a 10000 m slant range. The color bar distinguishes the difference in required dwell time in seconds. ....</p>	2
<p>2. Depicts the energy transfer through the system of eddies and depicts the various scale sizes. [Adapted from Fiorino, 2005a].....</p>	10
<p>3. Photograph of a thermosonde (left) and the boom (right) [Adapted from Adair, 2005] .....</p>	12
<p>4. Simulated intensity of a beam coming out of a Cassegrain-aperture, passing through 5km of strong optical turbulence. The picture on the left is the intensity directly after the transmitter-telescope, in the middle after 1km and on the right after 5km. The represented field is 0.512m x 0.512m, the aperture has an outer diameter of 20cm and an inner obscuration of 6cm diameter, wavelength is 1.064<math>\mu</math>m [Adapted from Fiorino, 2005a].....</p>	13
<p>5. Depiction of the beam, propagating wave front, windspeed vector, range, R, isoplanatic angle, <math>\theta_0</math>, and the Fried coherence length, <math>r_0</math>. [Adapted from Fiorino, 2005a].....</p>	15
<p>6. Depiction of the beacon and high energy laser beams' propagating wave fronts, coherence length, and isoplanatic angle. [Adapted from Fiorino, 2005a].....</p>	16

Figure	Page
7. Twenty random turbulence profiles corresponding to the same Fried coherence length and Rytov value. [Adapted from Whiteley, 2000].....	22
8. Plot showing the ranges of air-sea temperature difference in which NSLOT is valid, sensitive to small errors, or dominated by large errors [Adapted from Hammel et al., 2005] .....	27
9. The lognormal distribution for the East Asia summer site from 8,000-9,000 ft at 50-60 °F, which contained 905 different $C_n^2$ values. [Adapted from Gravley, 2004].....	31
10. HELEEOS display menus where the main menu is shown on top, and the atmosphere menu is on the bottom. [Adapted from HELEEOS].....	36
11. DEEST Analysis menu, which displays to the user, all of the input parameters to construct a desired scenario. [Adapted from DEEST].....	38
12. Hufnagel-Valley 5/7 profiles, standard (blue) and randomized (red) with 200 phase screens.....	41
13. Comparison of the East Asia summer thermosonde data, which was collected at night, to the HELEEOS correlated $C_n^2$ climatology. The top plot is each raw thermosonde profile, and the bottom contains the HELEEOS correlated climatology in comparison with the mean and standard deviation of $C_n^2$ over all of the thermosonde data. ....	45

Figure	Page
14. Comparison of the desert summer thermosonde data with the correlated $C_n^2$ climatology. The top plot is each raw thermosonde profile, and the bottom contains the correlated climatological profile with the thermosonde data mean and standard deviation.....	46
15. Mid-Latitude summer HELEEOS climatological profile, Hufnagel-Valley 5/7, and CLEARI superimposed over East Asia Summer thermosonde mean $C_n^2$ and Standard Deviation.....	49
16. Comparisons of the HELEEOS climatological profiles for the 50 <sup>th</sup> percentile RH with the standard models of Hufnagel-Valley 5/7 and CLEARI; East Asia Summer (top left), East Asia Winter (top right), Desert Summer (bottom left), Desert Winter (bottom right). The boundary layer height for the profiles is 1524 m. Note that the Mid-Latitude winter $C_n^2$ vertical scale is larger than the others. ....	50
17. Mid-Latitude and desert summer and winter optical turbulence profiles for 10 <sup>th</sup> percentile, 50 <sup>th</sup> percentile, and 95 <sup>th</sup> percentile relative humidity plotted against Hufnagel-Valley 5/7. ....	52
18. Enhanced Hufnagel-Valley 5/7 profile distributions for 100-400 m. ....	54
19. Two enhanced Hufnagel-Valley 5/7 $C_n^2$ distributions and the 30-35% relative humidity distribution for one of the desert winter locations in the boundary layer.....	55

Figure	Page
20. Enhanced Hufnagel-Valley 5/7 and CLEARI profiles with East Asia winter at 10-20 °F and East Asia summer at 40-50 °F from 9-10kft (the free atmosphere) for random distribution #4.....	57
21. Enhanced Mid-latitude Summer climatological profile with the corresponding East Asia thermosonde profiles.....	58
22. A comparison of the DEEST optical turbulence profiles for East Asia and Desert summer MM5 data, the HELEEOS correlated optical turbulence climatological profile for the corresponding ExPERT sites, and the Hufnagel-Valley 5/7 profile. ....	59
23. DEEST profile for 22:00 July 18, 2002 compared to corresponding balloon and scidar profiles. [Adapted from Adair, 2005] .....	60
24. Climatological profiles (right) for coastal desert summer and winter locations and NSLOT profiles (left) for oceanic locations near the ExPERT site. The geometry for this scenario is a 1 km slant range with the target and platform 10 m above the surface.....	62
25. Climatological profiles (right) for coastal mid-latitude summer and winter locations and NSLOT profiles (left) for oceanic locations near the ExPERT site. The geometry for this scenario is a 1 km slant range with the target and platform 10 m above the surface.....	64

Figure	Page
26. Worldwide map of required dwell times for all ExPERT Mid-latitude and Desert sites for the summer season, 1.06 $\mu$ m laser wavelength, 50 <sup>th</sup> relative humidity percentile, and 4000 m slant range. Hufnagel-Valley (top), Climatological (middle), and the Difference (bottom) .....	70
27. Dwell time difference plots between the climatological and Hufnagel-Valley profiles for a slant range of 4000 m (top) and 10,000 m (bottom).....	72
28. Worldwide required dwell time differences between Hufnagel-Valley 5/7 and the HELEEOS correlated climatological $C_n^2$ profiles for the summer season with variations in RH, 10 <sup>th</sup> percentile (top), 50 <sup>th</sup> percentile (middle) and 95 <sup>th</sup> percentile (bottom), a wavelength of 1.06 $\mu$ m, and a slant range of 10 km.....	73
29. Comparison of the East Asia winter thermosonde data to the corresponding HELEEOS correlated optical turbulence climatology. The top plot is each raw thermosonde profile, and the bottom contains the comparison between the HELEEOS correlated $C_n^2$ climatology and the thermosonde data mean and standard deviation. The boundary layer height for this scenario is 500 m.....	79
30. Comparison of the desert coastal winter thermosonde data to the corresponding HELEEOS correlated optical turbulence climatology. The top plot is each raw thermosonde profile, and the bottom contains the comparison between the HELEEOS correlated $C_n^2$ climatology and the thermosonde data mean and standard deviation. The boundary layer height for this profile is 500 m.....	80

Figure	Page
31. Comparison of the desert inland winter thermosonde data to the corresponding HELEEOS correlated optical turbulence climatology. The top plot is each raw thermosonde profile, and the bottom contains the comparison between the HELEEOS correlated $C_n^2$ climatology and the thermosonde data mean and standard deviation. The boundary layer height for this scenario is 500 m.....	81
32. Enhanced Hufnagel-Valley 5/7 and CLEARI profiles with desert winter at 10-20 °F and from 18-20kft for random distribution #2. ....	82
33. Enhanced Mid-latitude winter correlated $C_n^2$ climatology with the corresponding East Asia thermosonde profiles.....	83
34. Enhanced Desert summer correlated $C_n^2$ climatology and the corresponding ABL campaign thermosonde profiles. ....	84
35. Enhanced desert inland winter correlated $C_n^2$ climatology with the corresponding ABL campaign thermosonde profiles. ....	85
36. Enhanced desert coastal winter correlated $C_n^2$ climatology with the corresponding ABL campaign thermosonde profiles. ....	86
37. Enhanced Hufnagel-Valley 5/7 and East Asia winter ABL campaign thermosonde profiles with the HELEEOS correlated $C_n^2$ climatology.....	87
38. The difference in dwell time between Hufnagel-Valley 5/7 and the climatological profiles for the 10 <sup>th</sup> percentile relative humidity and a 4000 m slant range. ....	88

Figure	Page
39. The difference in dwell time between Hufnagel-Valley 5/7 and the climatological profiles for the 95 <sup>th</sup> percentile relative humidity and a 4000 m slant range. ....	88
40. The difference in dwell time between Hufnagel-Valley 5/7 and the climatological profiles for the 10 <sup>th</sup> percentile relative humidity and a 4000 m slant range. ....	89
41. The difference in dwell time between Hufnagel-Valley 5/7 and the correlated $C_n^2$ climatologies for the 50 <sup>th</sup> percentile RH and a slant range of 4000 m (top) and 10,000 m (bottom).....	90
42. The difference in dwell time between Hufnagel-Valley 5/7 and the correlated $C_n^2$ climatologies for the 95 <sup>th</sup> percentile relative humidity for a slant range of 4000 m (top) and 10,000 m (bottom) .....	91

## List of Tables

Table	Page
1. This shows how the magnitudes for the Fried coherence length, isoplanatic angle, and Greenwood frequency are affected by various turbulence strengths and propagation distances. [Adapted from Bartell et al. 2005].....	17
2. DEEST $C_n^2$ models and their regions of applicability [Adapted from Jumer et al., 2005].....	24
3. In the boundary layer the data were sorted by altitude, relative humidity range, and the corresponding optical turbulence values (top), and the upper air data were sorted in similar fashion, but by temperature. [Adapted from Gravley, 2004] .....	31
4. A list of atmospheric parameters and sample values from the AtmStruct calculation, atm=AtmStruct(61,366,0,150,'Cn2',HV57') .....	35
5. Table of the HELEEOS scenarios used in this study.....	40
6. The statistics for each log normal distribution.....	56
7. A tabular summary of required dwell times for an East Asia summer location using each of the standard and numerical profiles and the correlated $C_n^2$ climatology for 3 various scenarios: Low- altitude with a 10 km slant range; High-altitude with a 90 km slant range; Surface layer with a 5 km slant range. All scenarios use a 50 kW laser with a wavelength of 1.06 $\mu$ m with an aperture size of 0.5 m. ....	66
8. Boundary layer coefficients for the East Asia Summer campaign. ....	92

Table	Page
9. Upper air coefficients from 1-5 kft for the East Asia Summer campaign .....	92
10. Upper Air coefficients from 5-10kft for the East Asia Summer campaign .....	93
11. Upper air coefficients from 10-30 kft, and the temperatures are in °F for the East Asia Summer campaign. ....	94
12. A tabular summary of required dwell times for a desert summer location using each of the standard and numerical profiles and the correlated $C_n^2$ climatology for 3 various scenarios: Low- altitude with a 10 km slant range; High-altitude with a 90 km slant range; Surface layer with a 1 km slant range. All scenarios use a 50 kW solid state laser with an aperture size of .5 m.....	95

# COMPARISON OF CLIMATOLOGICAL OPTICAL TURBULENCE PROFILES TO STANDARD, STATISTICAL AND NUMERICAL MODELS USING HELEEOS

## I. Introduction

### 1.1 Significance of the Problem

Modeling electromagnetic wave propagation through the earth's atmosphere is of great interest to the Department of Defense. One reason for this interest is that many new defense systems use lasers to track and engage enemy missiles or ground targets.

Examples of these systems in development are the Airborne Laser (ABL) and the Advanced Tactical Laser (ATL). However, the modeling of this process is not trivial.

Unless the beam propagates in a vacuum, there will always be some type of effect to distort the beam. Due to atmospheric effects such as molecular and aerosol absorption and scattering, and optical turbulence, these distortions become more complex and non-linear.

Optical turbulence within earth's atmosphere plays a significant role in electromagnetic radiation propagation from a high energy laser. The index of refraction structure constant,  $C_n^2$ , is used to characterize and quantify the turbulent spatial fluctuations due to temperature gradients. These changes in the index of refraction affect the intensity of the laser energy wave front delivered to the intended target. Thus, it is important to characterize this parameter throughout the free atmosphere and the boundary layer for its applications regarding the ABL and the ATL.

This study examines the various methods for characterizing optical turbulence, which is significant because there has never been a quantitative comparison made between the numerous standard, statistical and numerical models and actual climatological optical turbulence. It is also important to properly characterize changes in simulations of high energy laser (HEL) system performance based on differences in modeled index of refraction ( $C_n^2$ ) profiles. A good example of the worldwide variations in system performance between simulations using different  $C_n^2$  profiles, characterized by the required dwell time on target, is illustrated in Figure 1.

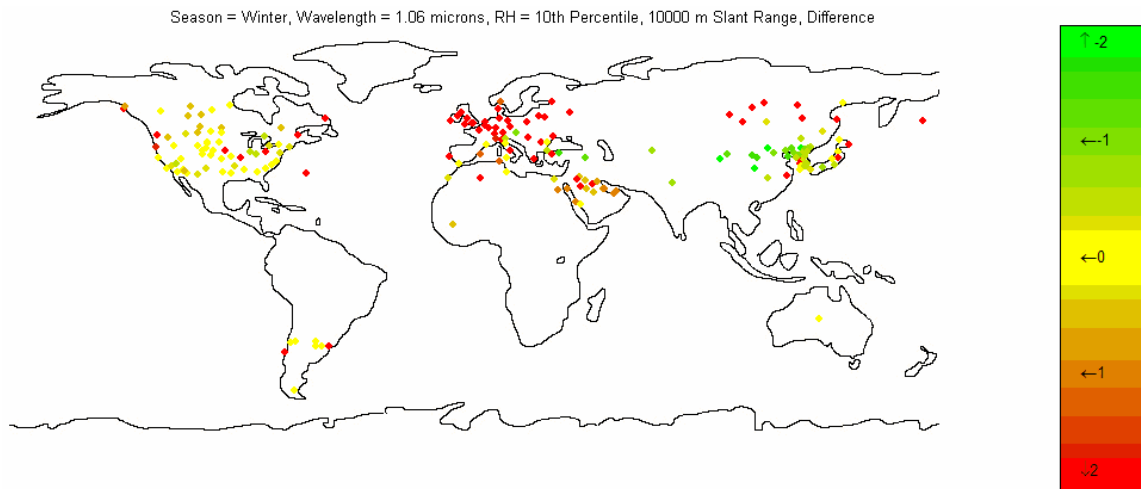


Figure 1: The difference in required dwell time between Hufnagel-Valley 5/7 and the climatological profiles for the 10<sup>th</sup> percentile relative humidity and a 10000 m slant range. The color bar distinguishes the difference in required dwell time in seconds.

Green sites indicate scenarios where the correlated climatological profile produces a shorter required dwell time than the Hufnagel-Valley 5/7 profile with a maximum difference of 2 s, and red sites indicate scenarios where the correlated climatological profile produced a longer required dwell time on target again with a maximum difference of 2 s. It is clearly shown in Figure 1 that there is a significant worldwide variation in

system performance simply based on the optical turbulence profile used in the calculation for the given scenario.

Due to the long slant ranges involved, it is essential to understand  $C_n^2$  for the ABL scenario and to have an accurate model for it. The ABL is a modified 747 that carries a chemical oxygen iodine laser (COIL) on board. Its mission is to damage enemy ballistic missiles in the boost phase and/or destroy the target near the launch site. To accomplish its task the ABL will fly above the clouds, to minimize the effects of most terrestrial weather. However, optical turbulence still plays a significant role in the beam intensity on target because of the long slant ranges over which this system operates. (Boeing, 2005)

Conversely, the ATL flies lower in the atmosphere, where optical turbulence is stronger but the slant ranges are much shorter. The Advanced Tactical Laser is expected to be a COIL mounted to a C-130, and it will operate at altitudes between 7,500 ft and 10,000 ft. With its rapid energy delivery at a high resolution (4 inch diameter beam from 9 miles away) coupled with its non-cooperative observations and surveillance capabilities, its mission is to engage stationary or moving ground targets. Since the ATL operates at lower altitudes, atmospheric parameters like molecular and aerosol extinction and terrestrial weather have greater impacts on the COIL beam distortion than optical turbulence. (GlobalSecurity.org, 2005)

## **1.2 Problem Statement**

There are several approaches to estimate the magnitude of optical turbulence vertical profiles. Suitable for realistic modeling and simulation, these methods include calculations from standard, statistical, numerical models or modified climatologies.

Examples of the various standard models, which are the simplest of the three, are Hufnagel-Valley 5/7, Critical Laser Enhancing Atmospheric Research (CLEARI), and Starfire Optical Range (SOR). Statistical models produce mathematically generated optical turbulence profiles, using climatology observations as a basis. Programs that utilize standard meteorological data to produce  $C_n^2$  profiles via empirical or physical relations are considered to be numerical optical turbulence models. Examples of this type of model include the Directed Energy Environmental Simulation Tool (DEEST) and Navy Surface Layer Optical Turbulence (NSLOT). A simulation model that accesses raw climatologies of  $C_n^2$  and correlates these data to other meteorological parameters for use in modeling and simulation is an example of a modified optical turbulence climatological model. The High Energy Laser End-to-End Operational Simulation (HELEEOS) is an example of an engagement simulation that provides a modified  $C_n^2$  climatology as an available option. The objective of this research is to quantifiably compare standard, statistical, numerical optical turbulence models and modified climatologies of  $C_n^2$  to one another. In doing this, one can learn whether or not each model will yield similar values to that of measured optical turbulence data, and quantify the effects these difference have on high energy laser system propagation performance.

### **1.3 Research Objectives**

The primary goal of this research is to compare the climatological model developed for HELEEOS to standard, statistical, and numerically derived optical turbulence models. One can do this using HELEEOS because this model contains these various optical turbulence profiles as an integral part of its programming. The main function of HELEEOS is to model HEL system performance under various atmospheric

conditions. It has the capabilities to model the irradiance delivered to a target considering molecular and aerosol absorption and scattering, clouds, and rain on a propagating laser beam front, and then utilizes this output to estimate the probability of a desired effect or the related parameters of required dwell time or effective range.

To accomplish this goal, several tasks are required. The modified  $C_n^2$  climatology data in HELEEOS are expanded within the boundary layer to better capture low altitude  $C_n^2$  behavior and the lower free atmosphere to accurately model optical turbulence profiles for varying boundary layer height. Then, HELEEOS's modified climatology and the standard models are compared to climatological thermosonde data, so that the differences between the profiles can be quantified and the validity of these profiles can be ascertained. Next, these profiles are enhanced using the statistical model to randomize the optical turbulence values of each one, so that the randomization technique can be compared to the climatological thermosonde data. Statistics are used to quantify the differences between the statistical model randomizations and the climatological thermosonde data. The final task is to compare the numerical profiles produced by DEEST and NSLOT to the HELEEOS climatology to determine how well these models compare to one another.

## **1.4 Organizational Overview**

Chapter 2 provides a brief background development of optical turbulence and the index of refraction structure constant,  $C_n^2$ . It begins with the theory of turbulence, and progresses through a description of the statistical mathematics used to quantify these random fluid motions. From here, the changes in the index of refraction due to turbulent flow in earth's atmosphere, optical turbulence, and the effects this property has on

electromagnetic radiation propagating through it are discussed. Finally, Chapter 2 provides summarized documentation concerning the various types of optical turbulence models used during this study. It explains, in detail, how and why each model was developed, and the specific technique each model uses to calculate optical turbulence vertical profiles.

The data and methodology used to produce and compare the optical turbulence profiles are discussed in Chapter 3. Each standard and HELEEOS climatological model produces an optical turbulence vector, which are then plotted together for straightforward comparisons. For the best comparison, the atmospheric conditions under which the different launches occurred are reproduced to the best of the HELEEOS program's capabilities. This is possible in part due to HELEEOS's robust atmospheric modeling capability. As for the statistical model, it also produces an optical turbulence vector from user-selected input parameters. However, the unique characteristic of this model is that the  $C_n^2$  values in the vector are randomized to better mimic climatological optical turbulence strength behavior. Since the standard and climatological profiles are smooth trends, their vectors are input data to the statistical model, and each of the randomized versions are plotted against raw thermosonde data to observe the two trends together. The final comparisons are made between the HELEEOS climatology and DEEST and NSLOT models. The DEEST data come from an outside source, but the NSLOT profiles are generated using HELEEOS.

Chapter 4 is a discussion of the results obtained from the various comparisons and the analysis used to quantify differences between the modeling approaches. It includes the validation of the modified  $C_n^2$  climatology, which was developed specifically for

HELEEOS. This section also contains the results from the comparisons between the standard models and the HELEEOS climatology. The next part of this chapter compares the statistical and climatological models, where it contrasts the randomization technique used by statistical model to mimic the physical irregularities of collected  $C_n^2$  profiles. The last profile comparison between the numerical models and the HELEEOS profile is made to determine the validity of numerically derived optical turbulence profiles produced by DEEST and NSLOT and climatological optical turbulence profile. This chapter concludes with plots of the required dwell times on a target based on assumptions of both the location-dependent correlated climatologies and the fixed Hufnagel-Valley optical turbulence profiles, and illustrates the differences between the two. This quantifiably clarifies which model predicts a “worst case scenario”.

Chapter 5 discusses the conclusions from the results of the study and recommends future research objectives. The two main conclusions are that the modified optical turbulence climatology developed for HELEEOS is a valid representation of thermosonde data, and all of this research can be done using HELEEOS as a tool. The comparative analysis validates the HELEEOS method for correlating  $C_n^2$  to meteorological parameters, and HELEEOS’ capability to identify the operational implications of differences in  $C_n^2$  profiles.

## II. Background and Literature Review

### 2.1 Chapter Overview

The purpose of this chapter is to provide a theoretical background and a detailed review of the literature concerning atmospheric optical turbulence and its effects on electromagnetic propagation. The first section of this chapter discusses the basic background of turbulent flow, pertaining specifically to the atmosphere. Next, is the development of atmospheric optical turbulence and the statistical structure constants, which quantify the fluctuations in temperature, index of refraction, and other atmospheric parameters. This is followed by a description of the thermosonde instrument because this illustrates how the statistical structure constants are physically measured. Then, an explanation of the effects of optical turbulence on a propagating optical beam is given. The chapter concludes with detailed descriptions of the various optical turbulence models that are commonly used throughout the Department of Defense.

### 2.2 Turbulence

There are two types of fluid flow; laminar flow is smooth and steady, and turbulent flow is unstable and random. Turbulence is a characteristic of the latter and is defined as irregular or random motions in a fluid. The transition between these two flows is defined by a dimensionless quantity called the Reynolds number

$$\text{Re} = \frac{vL}{\mu/\rho} \quad (1)$$

where  $v$  is the flow velocity ( $\text{m}^2 \cdot \text{s}^{-1}$ ),  $L$  is the characteristic length (m),  $\mu$  is the viscosity ( $\text{m} \cdot \text{s}^{-1}$ ), and  $\rho$  is the fluid density. When the Reynold's number is below 2000, the flow is

considered to be laminar, but when the flow is greater than 3000, the flow is turbulent. Turbulence is produced from a multitude of sources such as convection from hot surfaces, wind shear, or weather systems. This turbulent mixing generates local changes in temperature, humidity, and atmospheric composition, which can lead to changes in the index of refraction. (Fiorino, 2005)

Turbulence also behaves over a range of different scale lengths. Larger eddies transfer their kinetic energy to smaller eddies until all of the energy is dissipated by viscosity. This idea is critical to Kolmogorov's mathematical model for fluid velocity turbulence and is illustrated in Figure 2, where  $L_0$  is the non-homogeneous outer scale, which ranges from 10's to 100's of meters, and  $l_0$  is the homogeneous, isotropic inner scale, which is on the order of 0.1 to 10 mm. In earth's atmosphere, solar heating generates atmospheric kinetic energy over scale sizes that range from a few meters to a global scale. Other large scale energy transfers occur from infrared radiation exchange processes, gravity wave effects, and wind interactions with the ground. This kinetic energy is then dissipated through frictional heating, and near the earth's surface, it has a scale size less than one centimeter. The range over which this occurs is called the inertial sub range. (Hufnagel, 1985)

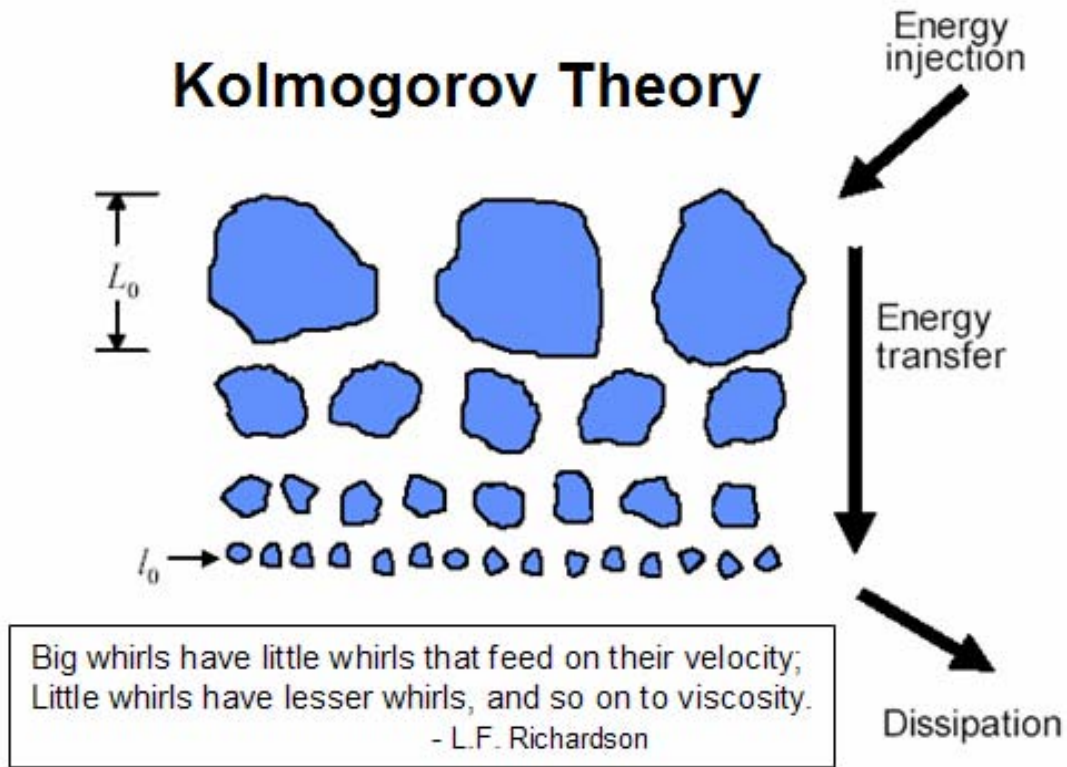


Figure 2: Depicts the energy transfer through the system of eddies and depicts the various scale sizes. [Adapted from Fiorino, 2005a]

### 2.3 Optical Turbulence

As described in the previous sections, atmospheric turbulence induces random irregularities in the index of refraction. Electromagnetic wavefronts propagating through this turbulence become distorted, which causes the beam to wander and spread.

Statistics are used to quantify these characteristics because the changes in the atmosphere's index of refraction are random. Thus, the end result is a quantitative description of the laser system's performance. (Hufnagel, 1985)

Since these optical phenomena depend on differential rather than absolute optical path lengths, the spatial statistics used to describe the random variations are given in

terms of structure functions. The structure function, the mean square difference in the index of refraction,  $n(r)$ , between two different locations in space,  $r_1$  and  $r_2$ , is defined as

$$D_n(r) = \left\langle |n(r_1) - n(r_2)|^2 \right\rangle \quad (2)$$

where  $r$  is  $r_1 - r_2$  and the subscript,  $n$ , indicates that the random variable is the index of refraction. Over the inertial sub range,  $l_0$  and  $L_0$ , Kolmogorov's theory further establishes the structure function in terms of a structure constant given by:

$$D_n(r) = \begin{cases} C_n^2 r^{2/3} & l_0 < r < L_0 \\ C_n^2 l_0^{-4/3} r^{2/3} & r < l_0 \end{cases} \quad (3)$$

The structure constant,  $C_n^2$ , quantifies the strength of the optical turbulence. A  $C_n^2$  value, that is on the order of magnitude of  $10^{-17} \text{ m}^{-2/3}$ , is considered to be weak turbulence, and strong turbulence values are on the order of  $10^{-13} \text{ m}^{-2/3}$ . For operational purposes physical  $C_n^2$  values are measured by an instrument called a thermosonde. (Hufnagel, 1985, Fiorino, 2005a)

## 2.4 Thermosondes

Thermosondes are balloon-borne instrument packages that measure *in-situ*  $C_T^2$ , the temperature structure constant. An image of a thermosonde is shown in Figure 3. This instrumentation consists of probes at the ends of a 1m long styrofoam boom. The changing resistance of a thin wire between them is used to calculate the root mean square temperature fluctuations using the Obukhov-Kolmogorov (Obukhov 1941, Kolmogorov 1941) turbulence theory.



Figure 3: Photograph of a thermosonde (left) and the boom (right)  
 [Adapted from Adair, 2005]

The equation for the temperature structure constant for Obukhov-Kolmogorov turbulence theory is,

$$C_T^2 = \left\{ \frac{[T(r_1) - T(r_2)]^2}{r^{2/3}} \right\}, \quad (4)$$

where  $r$  is  $|r_2 - r_1|$  (m),  $T(r_1)$  and  $T(r_2)$  are the temperatures at  $r_1$  and  $r_2$  ( $^{\circ}\text{C}$ ) respectively.

The temperature structure constant is vertically measured every seven to eight meters beginning from the surface to an altitude of 30 km above sea level. Due to the solar heating of the probes, these measurements are normally taken at night. Using an attached, modified rawinsonde package, the thermosonde also measures humidity,

pressure (p in mbars or hPa), temperature (T in Kelvin), and horizontal wind velocity.

(Roadcap et al. 2003) The thermosonde relays the temperature information to a ground station, which then calculates  $C_n^2$  as a function of altitude using the equation,

$$C_n^2 = C_T^2 \left[ 79 \times 10^{-6} \frac{p}{T^2} \right]^2 \quad (5)$$

(Jumper et al. 1997).

## 2.5 Effects of Optical Turbulence

The previous sections have discussed, in detail, the theoretical development of optical turbulence, where it comes from and how it is measured. For the Department of Defense the effects of optical turbulence on a propagating beam are more important to consider. Illustrated in Figure 4 is an example of the significant degradation effects optical turbulence has on a laser beam propagating through the atmosphere or some other turbulent medium.

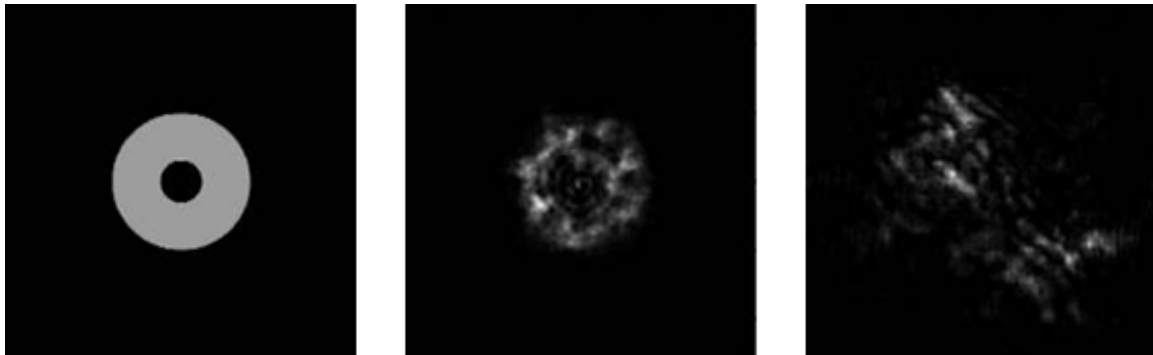


Figure 4: Simulated intensity of a beam coming out of a Cassegrain-aperture, passing through 5km of strong optical turbulence. The picture on the left is the intensity directly after the transmitter-telescope, in the middle after 1km and on the right after 5km. The represented field is 0.512m x 0.512m, the aperture has an outer diameter of 20cm and an inner obscuration of 6cm diameter, wavelength is 1.064 $\mu$ m

[Adapted from Fiorino, 2005a]

The optical system, that produced the images shown in Figure 4, did not use adaptive optics. Adaptive optics were developed to aid in the compensation for atmospheric turbulent fluctuations in the index of refraction and enhance performance. The system consists of a known source, called a beacon, which senses the phase distortions caused by the turbulence. From the beacon phase information, the conjugate of this phase can be applied to the outgoing laser beam. Problems, known as anisoplanatism, arise from the difference in turbulence along the beacon and outgoing laser paths. There are three different types of anisoplanatism, spatial, angular and temporal. (Beland, 1993)

Spatial anisoplanatism is described by the Fried coherence length,  $r_0$ . Since this parameter is one of the most important in characterizing the effects of turbulence on an optical system, it, therefore, serves as a convenient measure of the optical turbulence strength (Beland 1993). The coherence length represents the path-integrated effect of refractive-index fluctuations and is defined as

$$r_0 = \left[ \frac{2.905}{6.88} \left( \frac{2\pi}{\lambda} \right)^2 \int_{Path} C_n^2(z) \left( \frac{R-z}{R} \right)^{\frac{5}{3}} dz \right]^{-\frac{2}{3}} \quad (6)$$

where  $C_n^2(z)$  is the index of refraction structure constant as a function of altitude ( $m^{-2/3}$ ),  $R$  is the range (m), and  $z$  is altitude (m). Physically, the Fried coherence length is the radius of a circle in which the phase of the beam does not change significantly, as shown in Figure 5.

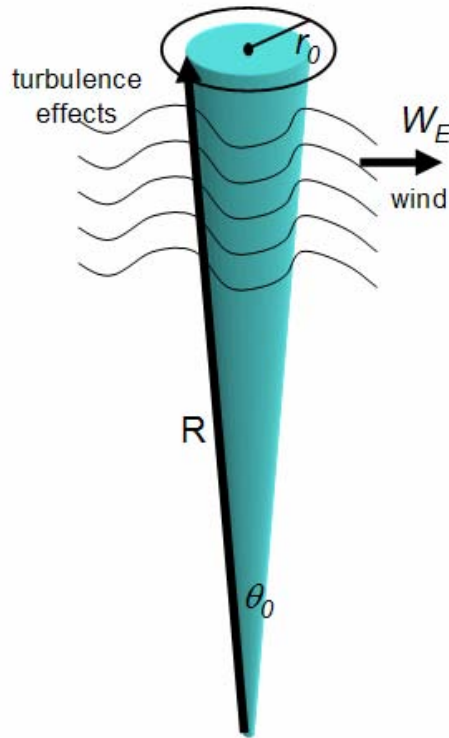


Figure 5: Depiction of the beam, propagating wave front, windspeed vector, range,  $R$ , isoplanatic angle,  $\theta_0$ , and the Fried coherence length,  $r_0$ . [Adapted from Fiorino, 2005a]

Fried developed  $r_0$  from an imaging perspective, and he found that the resolution of an image increased with aperture diameter until the diameter was equal to the coherence length. Without the use of adaptive optics, an increase in the aperture size greater than the coherence length does not result in an increase of image resolution. In terms of atmospheric propagation of a high energy laser, small values of  $r_0$  correspond to strong turbulence and greater beam distortion, while larger values represent weak turbulence and lesser distortion. (Bartell et al. 2005, Beland, 1993)

The measure of angular anisoplanatism is characterized by the isoplanatic angle,  $\theta_0$ . It represents the integrated effect of refractive index fluctuations along a vertical path, and is described by the equation

$$\theta_0 = \left[ 2.905 \left( \frac{2\pi}{\lambda} \right)^2 \int_{Path} C_n^2(z) \left( \frac{R-z}{R} \right)^{\frac{5}{3}} dz \right]^{-\frac{3}{5}} \quad (7)$$

where  $C_n^2(z)$  is the index of refraction structure constant ( $m^{-2/3}$ ),  $R$  is the range (m),  $z$  is altitude (m). Isoplanatic angle is defined as the maximum angle over which the phase difference between the beacon and laser beam wave fronts is small, and is illustrated in Figure 6.

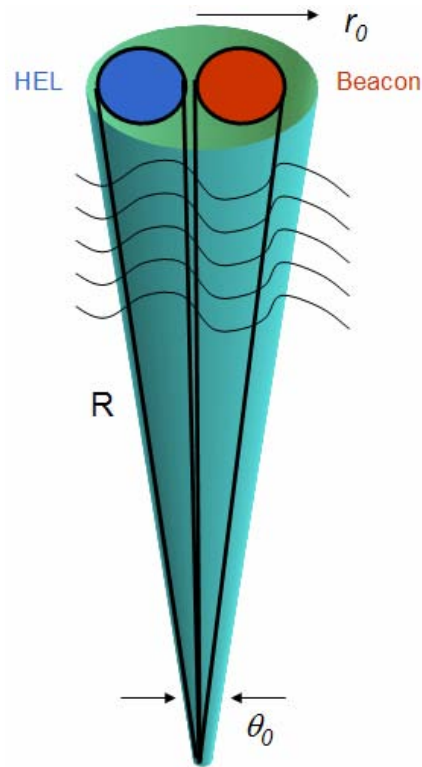


Figure 6: Depiction of the beacon and high energy laser beams' propagating wave fronts, coherence length, and isoplanatic angle. [Adapted from Fiorino, 2005a]

For performance purposes, if the beacon and kill beams do not fall within this angle, performance of the system degrades (Beland, 1993). Small isoplanatic angles indicate strong turbulence, and large values correspond to weaker turbulence.

Temporal anisoplanatism is characterized by the Greenwood frequency,  $f_G$ . The Greenwood frequency describes the temporal separation between the beacon and the outgoing laser beam, and is defined by the equation

$$f_G = \left[ 0.102 \left( \frac{2\pi}{\lambda} \right)^2 \int_{Path} C_n^2(z) W_E^{5/3}(z) dz \right]^{3/5} \quad (8)$$

where  $W_E$  is the wind speed ( $\text{m}\cdot\text{s}^{-1}$ ). It is a measure of how fast the optical system must respond to correct for the turbulent atmosphere. To understand the magnitude of each of the previously defined parameters, Table 1 provides a comparison of the calculated values for various slant ranges with constant optical turbulence along the path. (Bartell et al. 2005)

Table 1: This shows how the magnitudes for the Fried coherence length, isoplanatic angle, and Greenwood frequency are affected by various turbulence strengths and propagation distances. [Adapted from Bartell et al. 2005]

$C_n^2$ ( $\text{m}^{-2/3}$ )	Range R (km)	Fried $r_0$ (m)	Isoplanatic $\theta_0$ (rad)	Greenwood $f_G$ (Hz)
Weak	1000	$4.6 \times 10^{-2}$	$2.6 \times 10^{-8}$	275
$10^{-17}$	100	0.19	$1.1 \times 10^{-6}$	69
	10	0.74	$4.2 \times 10^{-5}$	17
Strong	1000	$1.9 \times 10^{-4}$	$1.1 \times 10^{-10}$	$6.9 \times 10^4$
$10^{-13}$	100	$7.4 \times 10^{-4}$	$4.2 \times 10^{-9}$	$1.7 \times 10^4$
	10	$2.9 \times 10^{-3}$	$1.7 \times 10^{-7}$	$4.4 \times 10^3$

Another effect due to optical turbulence is scintillation, the variation due to the phase distortions of the propagating beam through the atmosphere. These variations are defined by the Rytov number

$$\sigma_x^2 = 2.25 \left( \frac{2\pi}{\lambda} \right)^{\frac{7}{6}} \left( \int C_n^2(z) \left( \frac{z}{R} \right)^{\frac{5}{6}} (R-z)^{\frac{5}{6}} dz \right)^{\frac{-3}{5}} \quad (9)$$

where  $C_n^2(z)$  is the index of refraction structure constant as a function of altitude ( $\text{m}^{-2/3}$ ),  $R$  is the range (m), and  $z$  is altitude (m). However, these adaptive optical systems cannot correct for this variation. Data from star scintillations have also been used to develop optical turbulence models.

## 2.6 Optical Turbulence Models

There are three varieties of optical turbulence models that are utilized by the Department of Defense. These types are standard, statistical and numerical models. Each has its own unique set of input parameters and equations used to calculate  $C_n^2$ . Some models are very basic with minimal inputs and simple equations, while others are more involved and use complex mathematical calculations or utilize large databases of meteorological data to derive  $C_n^2$  profiles. (Fiorino, 2005b)

Standard models are relatively simple ones that calculate optical turbulence using an analytical equation or set of equations. These models consist of one equation or a system of equations that are derived by fits to thermosonde or stellar scintillometer data. There are only a few input parameters for these calculations, which include values such as altitude, pressure level, or sometimes wind speed. Instead of capturing all of the vertical fluctuations of  $C_n^2$  within a given profile, standard models provide a smooth and generalized trendline. Examples of this type of model include Hufnagel-Valley 5/7, CLEARI, and SOR. (Fiorino, 2005b)

Alternatively, statistical models are purely mathematical representations of optical turbulence profiles. Within the bounds of observations and climatology, they produce physically realistic turbulence spectra using random number generation, monte-carlo, or other mathematical techniques. Realistically, optical turbulence profiles are not smooth functions with altitude, such as the standard models produce, but highly variable. Statistical models attempt to capture the fluctuations. (Fiorino, 2005b)

Numerical models are similar to, but more complicated than the standard model because they use additional meteorological inputs, such as temperature, time-of-day, and humidity, to produce optical turbulence profiles. They are called numerical models because they obtain their necessary inputs from the output of physically-based numerical weather prediction models or from physically collected data. Examples of this type are DEEST and NSLOT. (Fiorino, 2005b)

### ***2.6.1 Hufnagel-Valley 5/7***

In 1974 Hufnagel developed a model on the basis of stellar scintillations and Bufton thermosonde measurements. He attempted to correlate the scintillation spectrum with meteorological wind parameters such as peak wind speed, speed at the tropopause, speed at significant inversions and speed at low Richardson's number. Like all models, it had several limitations. It was only valid at mid-latitude locations from 3km to 24km above the surface. Due to the complexity of the involved computations and uncertainty in the input parameters, only a mean value of  $C_n^2$  could be calculated. Later in 1988, P. B. Ulrich, following the suggestions of G. C. Valley, extended the model from 3 km down to the surface. The most popular version of this model is called the Hufnagel-Valley 5/7 (HV 5/7) model because the input parameters yield  $C_n^2$  profiles such that the

coherence length is 5 cm and the isoplanatic angle is 7  $\mu$ rad for an earth to space path (Good et al. 1988). This model calculates  $C_n^2$  using the following equation:

$$C_n^2(h) = 5.94 \times 10^{-53} \left( \frac{W}{27} \right)^2 h^{10} e^{\frac{-h}{1000}} + 2.7 \times 10^{-16} e^{\frac{-h}{1500}} + A e^{\frac{-h}{100}} \quad (10)$$

where A is the surface  $C_n^2$  value ( $m^{-2/3}$ ), h is the altitude in kilometers, and W is the root mean square wind speed (m/s) and the only input value. (Fiorino et al. 2006)

### 2.6.2 CLEAR I

This model, like the Hufnagel model, was developed from an extensive research campaign at White Sands Missile Range (WSMR) New Mexico during the late summer of 1984. The motivation behind this investigation was to provide the Army with a database for ground-based laser performance. This study was comprised of data collected from thermosonde and stellar scintillation measurements. A profile for the nighttime thermosonde data was created from an arithmetic average of all 18 night launches. This same procedure was done for the scintillometer data, which was collected over 30 consecutive nights, and the averages of both profiles compared well with one another. Therefore, the researchers felt they had produced a valid optical turbulence profile. (White et al. 1985)

The CLEAR I model characterizes optical turbulence in four different altitude layers, which results in the characterization of optical turbulence profiles by a system of four equations:

$$\log_{10} C_n^2 = \begin{cases} 0 & h < 1.23 \text{ km} \\ -10.7025 - 4.3507h + 0.8141h^2 & 1.23 < h < 2.13 \text{ km} \\ -16.2897 + 0.0335h - 0.0134h^2 & 2.13 < h < 10.34 \text{ km} \\ -17.0577 - 0.0449h - 0.0005h^2 + 0.6181e^{-5\left(\frac{h-15.5617}{3.466}\right)^2} & 10.34 < h < 30 \text{ km} \end{cases} \quad (11)$$

where  $h$  the altitude in kilometers above mean sea level (MSL) (Beland, 1993). Since this model claims to only be valid 1.23 km above MSL, the altitude of White Sands Missile Range, HELEEOS uses Hufnagel-Valley 5/7 to extend CLEARI to lower altitudes. (Fiorino, 2005a)

### ***2.6.3 Statistical Model ATMtools***

The initial stages for this model were developed for the Dynamic Compensation Experiment (DyCE) conducted at White Sands Missile Range. Wave optics code for this study was developed by researchers at the Air Force Research Laboratory (AFRL/DEBA) and MZA Associates Corporation in Albuquerque, NM. One of the many goals of DyCE was to use wave optics code to simulate and evaluate laser performance under variations in optical turbulence profiles along the propagation path. The atmosphere was divided up into to slabs, called phase screens, where each phase screen was of equal thickness and defined by some arbitrary  $C_n^2$  value. Using linear algebra techniques, the researchers derived matrix equations to express the Rytov parameter, Fried coherence length, and isoplanatic angle in terms of null space basis vectors and its coefficient,  $C_0$ , the arbitrary  $C_n^2$  value. For a fixed set of  $\sigma_x^2$ ,  $r_0$ , and  $\theta_0$ , they could produce a sequence of randomized optical turbulence profiles by adding random linear combinations of null space basis vectors. The coefficients of the null space basis vector,  $C_0$ , were generated as zero-mean Gaussian random numbers with  $\sigma$  equal to three. More specifically the distribution of  $C_0$  values is Gaussian, with an average value of zero. Sample results from this procedure are shown in Figure 7.

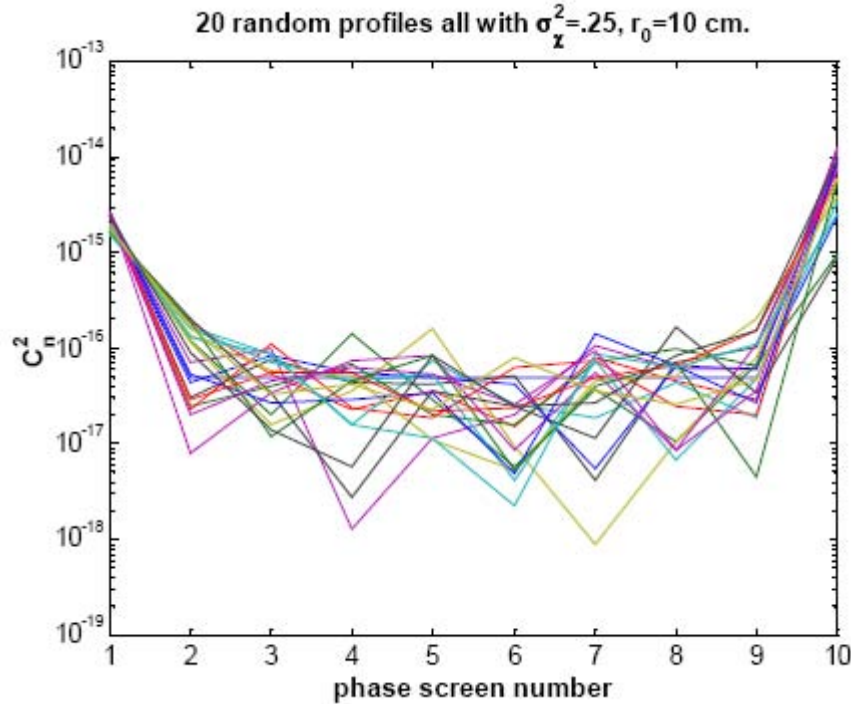


Figure 7: Twenty random turbulence profiles corresponding to the same Fried coherence length and Rytov value. [Adapted from Whiteley, 2000]

To safeguard against the production of unrealistic profiles, if a profile yielded a screen strength that was negative, then it was discarded and a new set would be generated.

(Whiteley, 2000)

Later, Dr. Eric Magee further expanded the model and developed an atmospheric structure function, which contains information about optical turbulence, wind, and molecular absorption and scattering. The model he developed is part of a toolbox called ATMtools, which is composed of an expansive collection of Matlab functions. One significant improvement to the previous model was the expansion of optical turbulence characterization along the propagation path. The previous model relied on two versions of the CLEARI profile to serve as an upper and lower bound for  $C_n^2$  along the path. However, this new model not only randomizes the standard profiles described above, but

it can also randomize the climatological profile produced by HELEEOS or any other user specified  $C_n^2$  vector. Once they have been computed, ATMtools can produce enhanced randomized versions of each profile. (Magee, 2005, Alliant Techsystems, 2005)

#### ***2.6.4 Directed Energy Environmental Simulation Tool***

The DEEST consists of a collection of various models that are used to simulate optical atmospheric effects. From user input values, DEEST is able to implement specific models from its database and produce the results on an interactive display. The models that are used to produce optical turbulence profiles for a specific atmospheric layer are shown in Table 2. Earlier versions of DEEST used only fifth generation mesoscale model (MM5) data for the continental United States (CONUS) region. Now, DEEST can use World Meteorological Organization Gridded Binary (GRIB) format, which contains worldwide meteorological data. Also, DEEST can implement one dimensional thermosonde data and apply them to an onion skin model. To model optical turbulence, DEEST divides the atmosphere up into layers, where each one uses a characteristic optical turbulence model. Surface layer optical turbulence, the first 50 m, is characterized by two different models, one for over the land and the other over water. The boundary layer is also described by two models, one for a stable and the other for an unstable boundary layer. Optical turbulence in the free atmosphere is characterized by the Dewan model, and CLEARI is used to characterize optical turbulence above the MM5 data. Table 2 clarifies which model is used for a specific atmospheric layer and a given scenario. (Jumper et al. 2005)

Table 2: DEEST  $C_n^2$  models and their regions of applicability  
 [Adapted from Jumper et al. 2005]

Region	Cn2 Model
Above MM5 Model Top (20-30 km)	Clear I
Above boundary layer and below MM5 model top (1-20km)	Dewan
Within boundary layer and above surface layer (0.1-1km)	Kaimal (Unstable) or Dewan (Stable)
Surface Layer (0-0.1km)	Over land: Tunick Over water: Frederickson and Davidson

#### 2.6.4.1 DEEST Boundary Layer Models.

The Tunick model, which strictly models the surface layer, is based on the  $C_n^2$  formulations of Tatarski, and it was validated by scintillometer data. Tunick found that his model's results were in close agreement with the measurements. However, there were some deviations which are thought to be caused by weakly stable conditions at night and when computed temperature gradients were very small. As for DEEST, it strictly uses the Tunick model for land scenarios because Tunick does not model optical turbulence well over bodies of water. The vertical profile produced by this model is given by the equations

$$C_n^2(z) = C_n^2(z^*) \cdot \left(\frac{z}{z^*}\right)^{(-4/3)} \quad \text{and} \quad C_n^2(z) = C_n^2(z^*) \cdot \left(\frac{z}{z^*}\right)^{(-2/3)} \quad (12)$$

Where  $z$  is the height above the ground (m),  $z^*$  is  $\Delta z/(\Delta \ln z)$  (m), and the  $-4/3$  indicates unstable and the  $-2/3$  indicates stable or near neutral atmospheric conditions. (Tunick 2003)

To predict optical turbulence over water layers, DEEST uses the Frederickson and Davidson model, a precursor to the NSLOT numerical model. This model was derived

from both Monin-Obukhov similarity theory and confirmed by experimental data collected over San Diego Bay by researchers from the Naval Post-Graduate School (NPS). As motivation, Frederickson and Davidson wanted to express  $C_n^2$  in terms of other meteorological parameters than simply windspeed and altitude. This model uses the more complicated equation to produce a  $C_n^2$  profile for the surface layer:

$$C_n^2 = A^2 C_T^2 + 2ABC_{Tq} + B^2 C_q^2 \quad (13)$$

where  $C_T^2$  is the temperature structure constant ( $K \cdot m^{-2/3}$ ),  $C_{Tq}$  is the temperature-specific humidity cross-structure parameter ( $K \cdot m^{-2/3}$ ),  $C_q^2$  is the specific humidity structure parameter ( $m^{-2/3}$ ), A is  $\frac{\partial n}{\partial T}$ , and B is  $\frac{\partial n}{\partial q}$ . (Frederickson et al. 2000)

When the boundary layer (BL) is considered to be unstable, the Kaimal model is used and supplied with a  $C_n^2$  value from the Tunick model. It produces a vertical profile from the equations

$$\frac{C_n^2(z)}{C_n^2(z_0)} = \begin{cases} \left(\frac{z}{z_0}\right)^{-4/3}, & z < 0.5z_{PBL} \\ \left(\frac{z_{PBL}}{2z_0}\right)^{-4/3}, & 0.5z_{PBL} < z < 0.7z_{PBL} \\ 2.9 \left(\frac{z}{z_{PBL}}\right)^3 \left(\frac{z_{PBL}}{2z_0}\right)^{-4/3}, & 0.7z_{PBL} < z < z_{PBL} \end{cases} \quad (14)$$

where  $z$  is the altitude (m),  $z_{PBL}$  is the height of the boundary layer (m), and  $z_0$  is the height of the surface layer (m). For a stable boundary layer, DEEST uses the Dewan model to estimate the value of optical turbulence, and it will be described in more detail within the next section. (Kaimal et al. 1976)

#### ***2.6.4.2 DEEST Upper Air Models.***

The DEEST uses the Dewan model to produce an optical turbulence profile for the upper atmosphere. This model is also based on the  $C_n^2$  calculations of Tatarski, and was developed for the stable free atmosphere. To compute a  $C_n^2$  vertical profile, the Dewan model uses the equation

$$C_n^2 = aM^2L^{4/3} \quad (15)$$

where  $a$  is the constant 2.8,  $M$  is the vertical gradient of refractive index ( $\partial n/\partial z$ ), and  $L$  is the characteristic scale length for optical turbulence. The scale length is a function of temperature, wind shear, and tropospheric height, and it uses separate equations to calculate the different values for the troposphere and the stratosphere. Above the top of the MM5 data, DEEST uses the CLEARI profile to produce the optical turbulence values. (Adair, 2005)

#### ***2.6.5 Navy Surface Layer Optical Turbulence***

The NSLOT model was developed by Frederickson and Davidson at NPS. It uses a bulk model developed from Monin-Obukhov Similarity theory (MOS), which utilizes measured environmental parameters to characterize atmospheric optical turbulence and gradient properties near the ocean surface. According to MOS theory, atmospheric conditions are assumed to be horizontally stationary and homogeneous, and turbulent fluxes of momentum, sensible heat, and latent heat are assumed to be vertically constant within the surface layer. This model is a successor to the model utilized in DEEST, and uses MOS theory to further develop Equation 13 into a bulk model described by mean meteorological parameters. (Frederickson et al., 2000)

The (Frederickson et al., 2000) bulk model developed from MOS theory was validated by a series of experimental measurements collected over San Diego Bay. Infrared scintillation measurements were obtained over a 7 km path concurrently with meteorological measurements collected from a buoy at the path's midpoint. Bulk estimates of  $C_n^2$  were computed from the data collected from the buoy and were compared to the scintillation-derived optical turbulence values. Under stable conditions the bulk  $C_n^2$  estimates became increasingly higher than the scintillation derived values as the air-sea temperature difference became larger and more positive (the air being much warmer than the water). Bulk  $C_n^2$  values decrease when the absolute air-sea temperature difference goes to small positive values approaching zero. A summary of the results is shown in Figure 8.

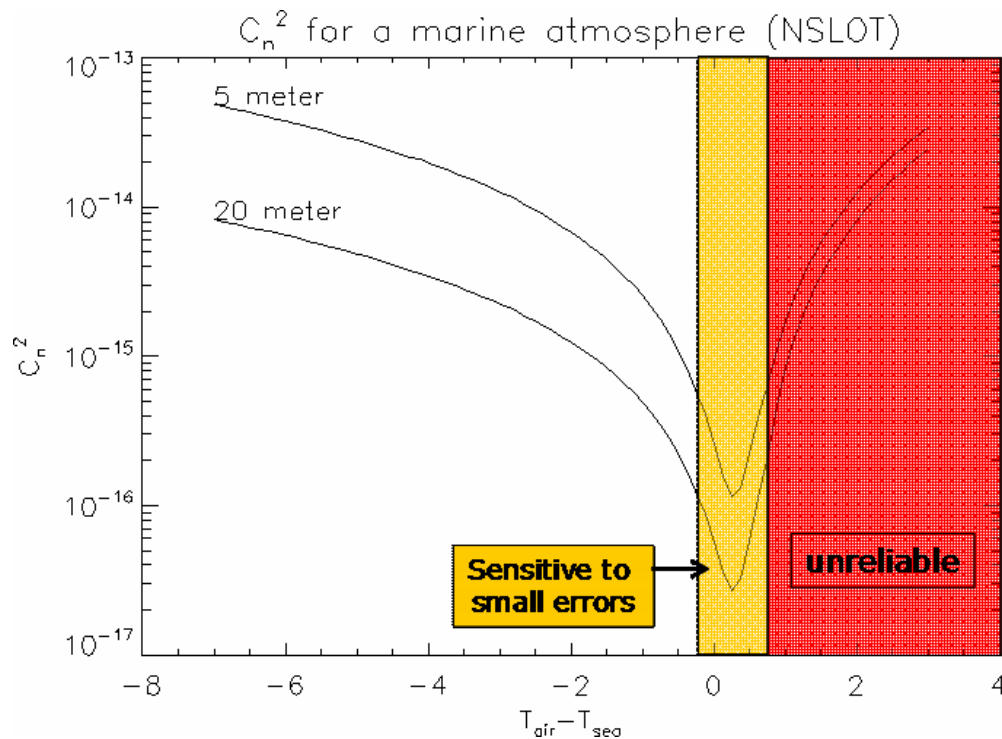


Figure 8: Plot showing the ranges of air-sea temperature difference in which NSLOT is valid, sensitive to small errors, or dominated by large errors.

[Adapted from Hammel et al. 2005]

## **2.7 High Energy Laser End-to-End Operational Simulation**

The HELEEOS is a parametric one-on-one engagement level model, which was developed by The Air Force Institute of Technology's (AFIT) Center for Directed Energy and sponsored by the High Energy Laser Joint Technology Office (JTO). This model incorporates scaling laws tied to respected wave optics code and all significant beam degradation effects from thermal blooming due to molecular and aerosol absorption and scatter to optical turbulence. HELEEOS evaluates the uncertainty in low-altitude HEL engagement due to all major clear-air atmospheric effects as well as clouds, rain and fog. Worldwide seasonal, diurnal, and geographical spatial-temporal variability in parameters, such as temperature, pressure, water vapor content and optical turbulence profiles, is organized into probability density function (PDF) databases. To do this, HELEEOS uses a variety of resources which include Extreme and Percentile Environmental Reference Tables (ExPERT), the Master Database for Optical Turbulence Research in Support of the Airborne Laser, and the Global Aerosol Data Set (GADS). Updated ExPERT mapping software allows the user to select a specific site, regional surface, and upper air data to characterize the atmospheric degradations on the beam by surface level relative humidity percentile. Also, the PDF nature of HELEEOS's atmospheric effects package provides realistic analyses of uncertainties in the probability of kill. The user can access, display and export atmospheric data independent of a HEL engagement simulation.

The ExPERT database is a joint effort by the Air Force Research Laboratory's Air Vehicles and Space Vehicles Directorates, and the Air Force Combat Climatology Center. ExPERT is an interactive microcomputer program, which displays pre-calculated climatological values for various regions, including Land, Ocean, and the Free

Atmosphere, as well as for 299 sites worldwide. For the individual surface land sites, this program allows the user to view monthly and hourly percentile data, duration data, and yearly minimum and maximum values for the following atmospheric variables: altimeter setting; dewpoint temperature; absolute humidity; relative humidity; specific humidity; temperature; wind speed; and wind speed with gusts. Percentiles for diurnal and sky cover data are displayed as well. Also available are the percent frequency of occurrence for several significant weather phenomena: thunderstorms; fog; blowing snow or sand; freezing rain; hail; snow; and rain. Notably, ExPERT also enables the user to display the probabilities of when a particular combination of temperature and relative humidity will occur for a specific land site (Squires et al., 1995).

For the upper air (or free atmosphere) and ocean regions, where the climatological record is not built upon hourly observations, percentiles are not directly calculated by binning the observations by numbers of occurrence. Since the upper air and ocean data are compiled from twice-daily balloon launches (upper air), irregular aircraft and satellite measurements, and irregular ship observations (ocean), the historical records are in the form of mean and standard deviation data only. ExPERT percentiles for the upper air and ocean regions are projected from the mean and standard deviations assuming either a normal or gamma distribution. The free atmosphere data in ExPERT are provided at every 1000 ft (305 m) from the surface to 10,000 ft (3048 m), every 2000 ft from 10-20 kft, every 5000 ft from 20-50 kft, and every 10 kft from 50-80 kft (Fiorino and Parks, 1995).

In the Global Aerosol Data Set (GADS) incorporated into HELEEOS (Koepke et al., 1997), the atmospheric aerosol particles are described by 10 main aerosol

components, which represent the atmosphere and are characterized through their size distribution and their refractive index depending on the wavelength. These aerosol particles are based on components resulting from aerosol emission, formation, and removal processes within the atmosphere, so that they exist as mixture of different substances, both externally and internally. Typical components include water-soluble, water-insoluble, soot, sea-salt and mineral, and the sea-salt particles are defined in two classes and the mineral particles in four. GADS allows the display of the global aerosol distribution of each defined aerosol component, including the vertical profile, on a  $5^\circ \times 5^\circ$  latitude-longitude grid for summer and winter. This permits the determination of the radiative properties and mass concentration of the resulting externally mixed aerosols at each grid point on the globe. (Fiorino et al., 2006)

The correlated optical turbulence profile in HELEEOS comes from the data collected in the Master Database for Optical Turbulence Research in Support of Airborne Laser (Bussey et al. 2000). This database was obtained from thermosonde vertical profile measurements at different locations worldwide. For HELEEOS the climatological values of  $C_n^2$  were analyzed to obtain distributions within the boundary layer and at higher altitudes. The earth was treated as an “onion skin” model, where the atmosphere was broken up into altitude layers within the planetary boundary layer and the upper air region. In the boundary layer HELEEOS uses an empirical relation between  $C_n^2$  and relative humidity, and for higher altitudes it relates optical turbulence to temperature for a respective altitude bin. Table 3 is visual aid to clarify how the data were categorized into the bins for each of the different atmospheric layers. (Fiorino et al. 2006)

Table 3: In the boundary layer the data were sorted by altitude, relative humidity range, and the corresponding optical turbulence values (top), and the upper air data were sorted in similar fashion, but by temperature. [Adapted from Gravley, 2004]

<b>0-5% RH</b>	<b>5-10% RH</b>	<b>10-15% RH</b>	~~	<b>95-100% RH</b>
Altitude	Altitude	Altitude	~~	Altitude
Relative Humidity	Relative Humidity	Relative Humidity	~~	Relative Humidity
Cn2	Cn2	Cn2	~~	Cn2
<b>-70--60</b>	<b>-60--50</b>	<b>-50--40</b>	~~	<b>90-100</b>
Altitude	Altitude	Altitude	~~	Altitude
Temperature	Temperature	Temperature	~~	Temperature
Cn2	Cn2	Cn2	~~	Cn2

Regardless of whether optical turbulence was being empirically related to temperature or relative humidity at a given altitude layer, each distribution of optical turbulence was well-fitted by a lognormal function. The program, Tablecurve2D, was used to fit equations to the distributions. An example of a lognormal fit and its five unique coefficients is shown in Figure 9. (Fiorino et al. 2006)

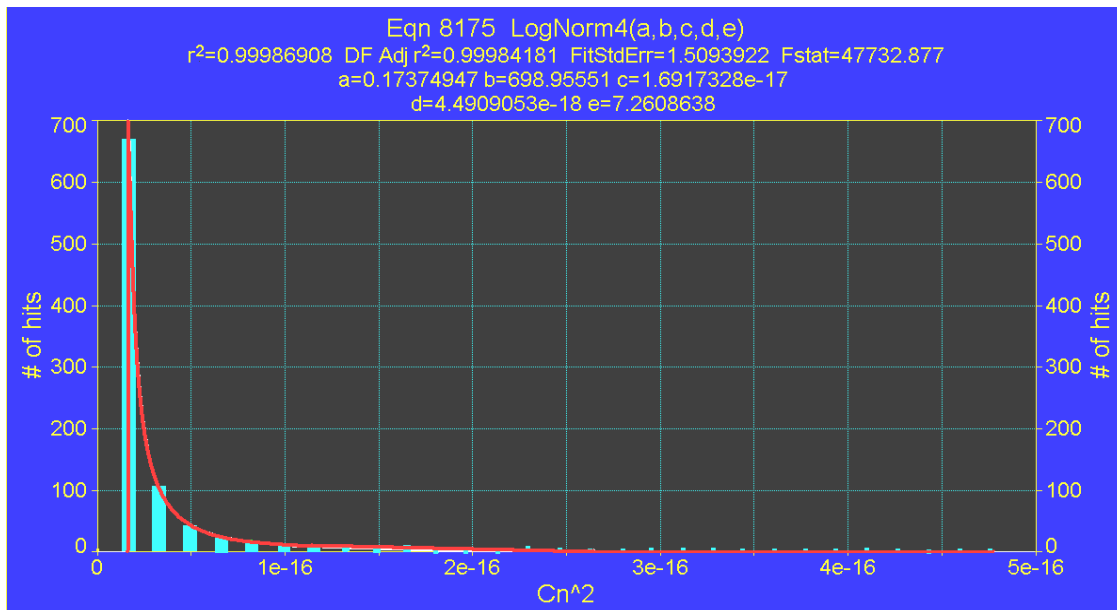


Figure 9: The lognormal distribution for the East Asia summer site from 8,000-9,000 ft at 50-60 °F, which contained 905 different  $C_n^2$  values. [Adapted from Gravley, 2004]

In turn, each lognormal distribution function is stored for its respective boundary layer and above boundary layer altitude bins in the form of its five unique coefficients of the following equation:

$$x = \frac{\exp\left(\frac{\pm 1}{\ln(2)} \left[ \ln(2) \cdot \ln\left(\frac{(y-a)}{b}\right) \right]^{\frac{1}{2}} \cdot \ln(e)\right) \cdot d \cdot (e-1) + c \cdot e^2 - c}{(e^2 - 1)} \quad (16)$$

where x is the  $C_n^2$  value ( $m^{-2/3}$ ) and y is the number of counts.

To produce an optical turbulence profile, HELEEOS begins by utilizing the ExPERT database, and with the data provided, HELEEOS calculates temperature and relative humidity profiles. Then, it references the lognormal distribution database and produces a mode  $C_n^2$  value for the corresponding atmospheric bin. For the boundary layer, it produces an optical turbulence value from the altitude and relative humidity bin that corresponds to the weather data from the ExPERT site. To produce values for the upper air region, HELEEOS matches a  $C_n^2$  value to the corresponding altitude and temperature bin. (Fiorino et al. 2006)

### III. Data and Methodology

#### 3.1 Chapter Overview

The purpose of this chapter is to discuss, in detail, the data and the methodology used in this study. The data section is a discussion of the different sources of optical turbulence profiles. These range from simple systems of equations to more complicated computer programs. The standard, correlated  $C_n^2$  climatological, and NSLOT profiles are calculated using HELEEOS because the equations are already integrated into the program. The statistical model data are generated using the ATMtoolbox and Matlab, and the DEEST profiles are sample profiles from Sara Adair. Even though the profiles are calculated using different models, the output data are similar in structure.

In order to accomplish the objectives of this research, the following tasks are to be completed:

1. Modification of the existing HELEEOS correlated  $C_n^2$  climatology by expanding the  $C_n^2$  distribution data for two distinct altitude sections within the boundary layer and extension of the free atmosphere data down to 1,000 ft. This supports a variable boundary layer height.
2. Verification that the correlated  $C_n^2$  climatological profiles legitimately represent the thermosonde data used to produce them.
3. Use of HELEEOS to produce the standard models, Hufnagel-Valley 5/7 and CLEARI, and compare them to the correlated  $C_n^2$  climatological profiles generated for scenarios corresponding to the thermosonde launches. This shows whether or not the simple standard models represent realistic optical turbulence values over variations in climatology.

4. Generation of randomized optical turbulence profiles using the statistical model for conditions similar to those of the climatological data. Then calculate and compare these distributions.
5. Plot randomized Hufnagel-Valley 5/7 and HELEEOS correlated  $C_n^2$  climatological profiles with the thermosonde data to observe and quantify trends in each.
6. Obtain MM5 data that correspond to the times and dates of the thermosonde launches for the ABL campaign. Use these data to produce numerically derived optical turbulence profiles.
7. Plot the DEEST profiles with the correlated climatological profiles to determine the validity of the DEEST profile using HELEEOS.
8. Plot the NSLOT profiles against the HELEEOS correlated climatological profiles to determine the validity of both profiles and optical turbulence characterization.

### **3.2 Data**

The data used in this research came from several different sources ranging from basic equations found in textbooks to more complicated databases and computer programs. Since they are versatile, the equations governing the standard models are easily programmable into any of the more complicated models. The standard profiles are part of both the HELEEOS and the statistical model, and they are straightforwardly reproduced by selecting one from a menu. The output data are in the form of two vectors, one of  $C_n^2$  values and the other for the corresponding altitude values.

The statistical model uses Matlab functions from ATMtools called `AtmStruct`, which calculates an atmospheric structure, and `RandCn2Prof`, which computes a

randomized optical turbulence profile from the atmospheric structure. `AtmStruct` generates a structure from atmospheric model data for a propagation path, specified by the platform and target heights (m), downrange distance (m), the number of equal thickness phase screens, model type, and model name. The Matlab structure contains the information displayed in Table 4.

Table 4: A list of atmospheric parameters and sample values from the `AtmStruct` calculation, `atm=AtmStruct(61,366,0,150,'Cn2',HV57')`

<b>Parameter</b>	<b>Name</b>	<b>Value</b>
<b>hp</b>	platform height (m)	61
<b>ht</b>	target height (m)	366
<b>rd</b>	downrange distance (m)	0
<b>L</b>	slant range (m)	305
<b>z</b>	phase screen distance vector (m)	[200x1 double]
<b>dz</b>	phase screen thickness vector (m)	[200x1 double]
<b>h</b>	phase screen altitude vector (m)	[200x1 double]
<b>Cn2</b>	optical turbulence vector ( $m^{(-2/3)}$ )	[200x1 double]
<b>Cn2Eval</b>	Cn2 model used	HV57(h);'

Once the atmospheric structure has been generated, the randomized  $C_n^2$  profiles can be calculated using the Matlab function `RandCn2Prof`. This function also requires several different input parameters; the atmospheric structure generated with `AtmStruct`, the number of generated random randomized profiles, a standard deviation for the random vectors, a threshold for the normalized  $C_n^2$  values, and a user designated fixed  $r_0$ ,  $\theta_0$ ,  $\sigma_x^2$ , and beam quality,  $M_0$ . The output optical turbulence structure contains all of the different randomized profiles, and their corresponding Rytov variances, coherence lengths, isoplanatic angles, and average  $C_n^2$  values. After both functions have computed their respective data sets, the optical turbulence profiles can then be plotted using any graphical program.

HELEEOS provides the user with a menu, where one can simply select parameters or enter values for a desired scenario. An example of the main menu and atmospheric parameters menu is illustrated in Figure 10.

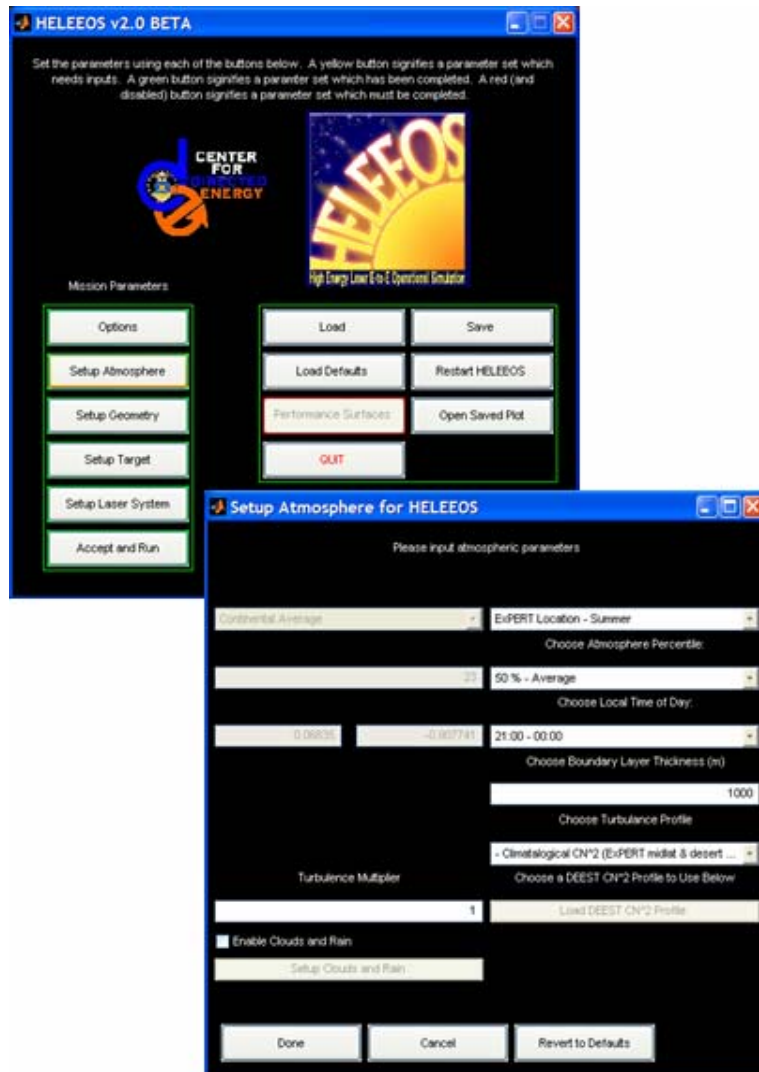


Figure 10: HELEEOS display menus where the main menu is shown on top, and the atmosphere menu is on the bottom. [Adapted from HELEEOS]

To produce correlated optical turbulence climatologies, HELEEOS uses a large meteorological database called ExPERT, which is composed of weather data tables for hundreds of sites worldwide. When the user has specified a relative humidity percentile,

ExPERT provides HELEEOS with surface RH and temperature values for the selected site, and HELEEOS calculates relative humidity and temperature vertical profiles based on these surface values. Within the boundary layer (variable up to 1525 m), optical turbulence is determined by the ExPERT site's relative humidity based on the specified percentile conditions. For  $C_n^2$  values above the boundary layer, the user-defined percentile is used to obtain a temperature, which is then empirically related to a  $C_n^2$  value. The output profiles HELEEOS produces are altitude vectors. More specifically, for this study these altitude vectors range from 114 m to 6,000 m in 50 evenly spaced divisions.

The DEEST uses two different types of standard Air Force Weather Agency files, MM5 and GRIB files. To calculate atmospheric effects for a desired laser propagation path over the continental United States (CONUS), the DEEST model only requires the use of MM5 data. For scenarios over the remaining parts of the world, the user must obtain GRIB files for the region (Jumper et al. 2005). DEEST has a display menu, depicted in Figure 11, where the user can select weather data for a region, zoom in on a more specific location, and then select or enter in the desired parameters. Once the user has selected a specific file and designated the desired parameters, DEEST outputs a  $C_n^2$  vector profile for the given scenario. This vector can then be plotted in any program that has graphing capabilities.

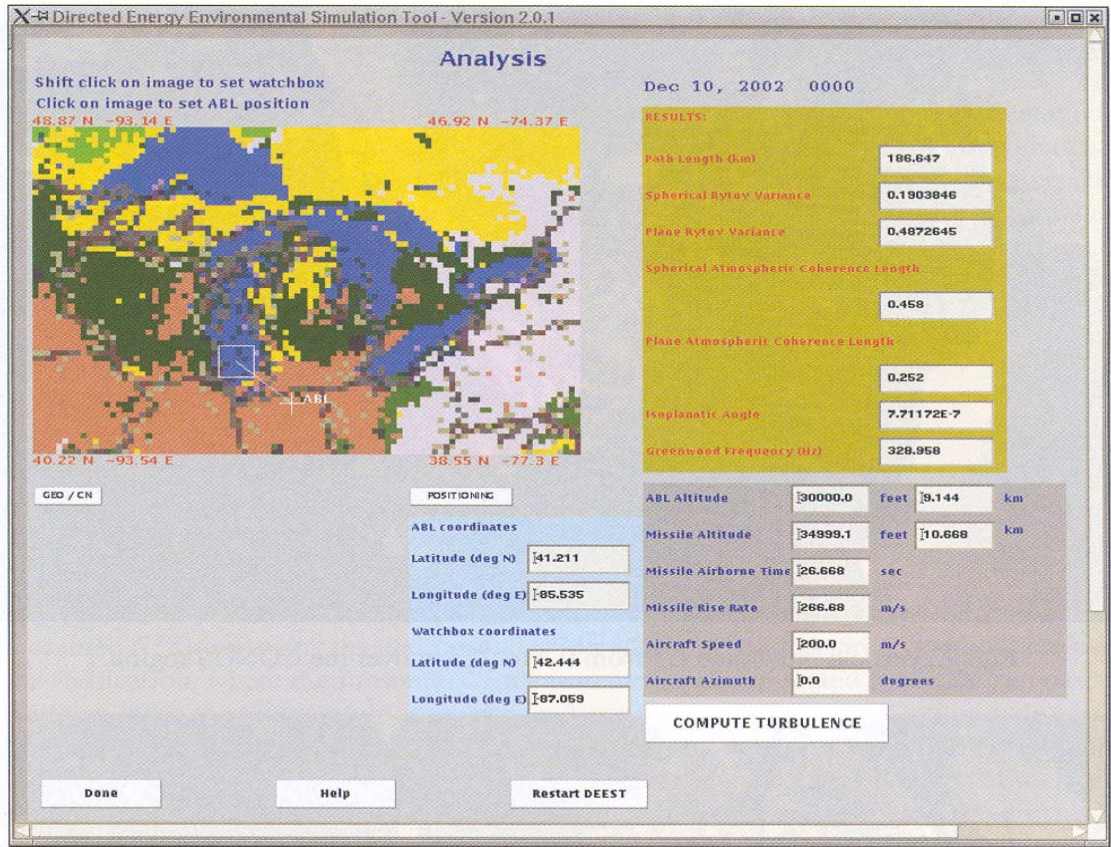


Figure 11: DEEST Analysis menu, which displays to the user, all of the input parameters to construct a desired scenario. [Adapted from DEEST]

### 3.3 Methodology

The following section describes the background work that had to be completed before the analysis work could begin. It discusses how the data mentioned above are used to produce optical turbulence profiles, so that the desired comparisons could be made, and it also describes the statistical methods used to quantify these differences. As noted in chapter 2, the HELEEOS climatological  $C_n^2$  database had to be expanded for each location and season. This included adding two slabs that divide the boundary layer, one from the surface to 200 ft and the other which extends from 200 ft to 1200 ft, and an extension of the free atmosphere profiles down to 1000 ft. Having only one altitude slab

for the entire boundary layer did not provide enough resolution to produce valid optical turbulence profiles. Appendix tables Table 8, Table 9, Table 10, and Table 8 display the log-normal coefficients for the various altitude layers and their resolution. Also, HELEEOS is programmed to model changes in the boundary layer height, so the data for the upper air region also needed to be extended down to lower altitudes to account for this change and still keep the relationships between  $C_n^2$  and RH and temperature consistent.

After these modifications were made, the data were analyzed for each new bin, and the coefficients for each log-normal distribution were entered into the optical turbulence database for HELEEOS. This improvement to the HELEEOS climatological data ensured valid  $C_n^2$  values for varying boundary layer heights. The purpose of using climatologically derived and meteorologically correlated optical turbulence values is to produce more accurate and versatile profiles than a standard equation could provide.

To make the comparison between the standard and the correlated climatological profiles, HELEEOS is used to produce the optical turbulence profile for both of the different model types. The only inputs required to calculate the standard profiles are the profile's selection from a menu and the desired geometry setup, so an altitude vector with the specific bounds can be generated. A comparable correlated  $C_n^2$  climatological profile is produced using the same geometry to provide an identical altitude vector, but the atmospheric parameters also had to be defined for a specific scenario. These values were chosen to mimic the conditions under which the thermosonde data were collected. For all scenarios, an ExPERT location with an equivalent geographic location to each launch site

was used to provide the proper atmospheric and climatological data. A list of the different scenarios for this study is shown in Table 5.

Table 5: Table of the HELEEOS scenarios used in this study.

<b>Expert Location</b>	East Asia	Desert
<b>Season</b>	Summer	Summer
	Winter	Winter
<b>Atmosphere %-tile</b>	50%	50%
<b>Local Time-of-Day</b>	21:00-00:00	21:00-00:00
<b>Turbulence Profile</b>	Climatological	Climatological
	HV 5/7	HV 5/7
	CLEARI	CLEARI
<b>Platform Altitude</b>	6,000 m	6,000 m
<b>Target Altitude</b>	0 m	0 m

An assumption was made that the thermosonde data were collected under average weather conditions, which meant that ExPERT provided HELEEOS with 50<sup>th</sup> percentile atmospheric values for the selected site. Another variable to consider is the boundary layer height for a given time of day. Since HELEEOS allows a varying boundary layer, boundary layer heights for different times of the day can be factored into the analysis. Each of the thermosonde campaigns were conducted during the late evening and night time frames. Therefore, the time of 21:00-00:00 is selected for that input parameter.

In the next chapter statistical model randomizations of  $C_n^2$  profiles are used to provide a wider variety of comparisons for analysis. The first goal is to compare a randomized distribution to a climatological distribution. An example of the original Hufnagel-Valley 5/7 profile and a randomized version of this are illustrated in Figure 12. To do this each randomized profile is broken up into altitude layers similar to those of the thermosonde data, and a distribution is calculated for each one. Five randomized Hufnagel-Valley 5/7 profiles are generated for 100 equally spaced phase screens using the top and bottom of the second boundary layer slab (61-366 m), as defined for the

HELEEOS correlated climatology, as lower and upper altitude limits for the optical turbulence profile. Chosen at random, profiles #2 and #4 are used in the analysis. Once the distributions are fitted in Tablecurve2D with the lognormal equation, both are compared to another boundary layer climatological distribution. For example, they are plotted together with the desert summer 30-35% relative humidity bin because the number of phase screens is approximately equal to the same number of  $C_n^2$  values in this climatological bin. This same procedure was used to make two more comparisons between bins in the upper air region.

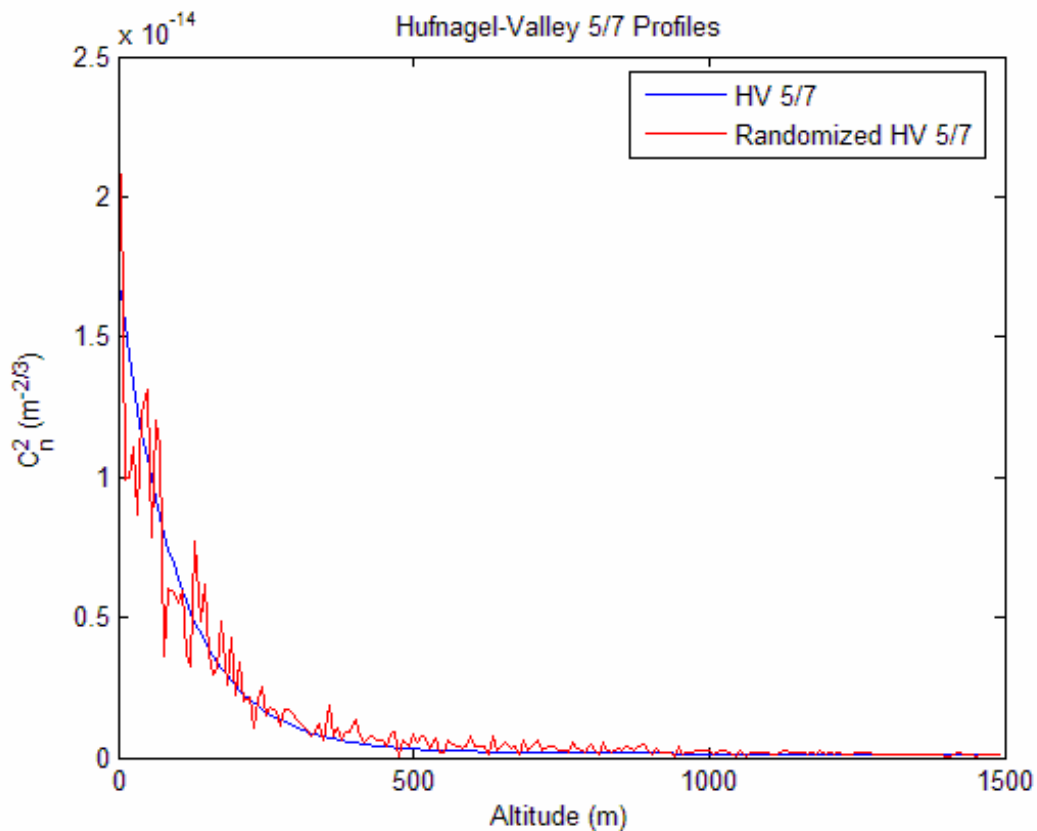


Figure 12: Hufnagel-Valley 5/7 profiles, standard (blue) and randomized (red) with 200 phase screens.

Next, a comparison is made between the randomized profiles and the thermosonde data. This is done by plotting five randomized correlated  $C_n^2$  climatological profiles calculated for each site and season with five thermosonde profiles for the corresponding launch site. For this comparison, the objective is to observe the statistical randomizations against the climatological ones, and determine whether or not the statistical model's randomization technique realistically mimics the climatology.

The final comparisons are between the HELEEOS profile and ones and the numerically generated optical turbulence profiles of the DEEST and the NSLOT models. Each optical turbulence profile for DEEST and NSLOT is generated for similar conditions to the thermosonde data. A comparable scenario to that of each launch, including general geographic location, season and time of day, is used for input variables to generate each of the numerically derived optical turbulence profiles, which ensures the validity of each comparison.

## IV. Results and Analysis

### 4.1 Chapter Overview

This chapter discusses the results produced by the various optical turbulence models and the techniques used to analyze the data. The first section verifies that the correlated  $C_n^2$  climatology developed specifically for HELEEOS represents the thermosonde data from which it was derived. With this established, the standard model profiles, along with the climatological profiles, are compared to the thermosonde data for the various seasons and locations to determine the versatility of the standard profiles. Discussed in section 4.4 are the results of the comparisons between the statistical analysis of the statistically randomized optical turbulence profile and the thermosonde profiles. The numerically derived DEEST and NSLOT profiles are compared to the correlated  $C_n^2$  climatological profiles in section 4.5, and the last section discusses the effects the various optical turbulence profiles have on HEL system performance prediction.

### 4.2 Validation of the HELEEOS Climatological Profile

The following sets of figures compare the optical turbulence profile collected by each thermosonde launch to the corresponding correlated  $C_n^2$  climatology produced by HELEEOS. For this specific comparison, the conditions during which the thermosonde data were collected are simulated in HELEEOS to produce the correlated optical turbulence climatological profile for each launch site. An ExPERT location with a similar geographic location to the launch site is chosen for each of the four scenarios, mid-latitude and desert summer and winter. It is assumed that the data were collected during average seasonal temperatures and relative humidities. HELEEOS also has the

capability to simulate diurnal changes within the boundary layer. In particular one can specify the time of day, which results in varying boundary layer heights. Therefore, the relative time frame for the balloon launches is another input variable to the scenario.

The first comparison, shown in Figure 13, is for a Mid-latitude North location in East Asia during the summer season. The top plot illustrates the trends of the raw thermosonde optical turbulence profiles, where each individual balloon launch is represented by a different color. Statistics are used to empirically correlate  $C_n^2$  to the climatological parameters, relative humidity and temperature. Then an optical turbulence profile can be generated for the specified conditions, which is represented by the blue line in the bottom figure. Since these particular launches occurred during the late evening, 21:00-00:00 is used as the time of day, which yields a boundary layer height of 1000 m. The bottom plot shows the HELEEOS profile, the solid blue line, the thermosonde mean  $C_n^2$  value, represented by the solid black line, and the standard deviation of  $C_n^2$  over all of the different launches, which is represented by the gray shaded region.

The HELEEOS climatological profile captures the general trend of the thermosonde launches, but it does not capture the smaller variations. Initially, the HELEEOS profile is approximately 65% greater than the standard deviation, but quickly drops within it a few meters higher. At 1.1 km the climatological profile captures the peak in  $C_n^2$  that occurs just above the boundary layer. However, the HELEEOS profile does predict a broader peak with a lower magnitude than the mean  $C_n^2$  profile. At 2 km and 3 km there are several smaller spikes in the thermosonde optical turbulence values, which are captured under broader curves of the correlated  $C_n^2$  climatological profile.

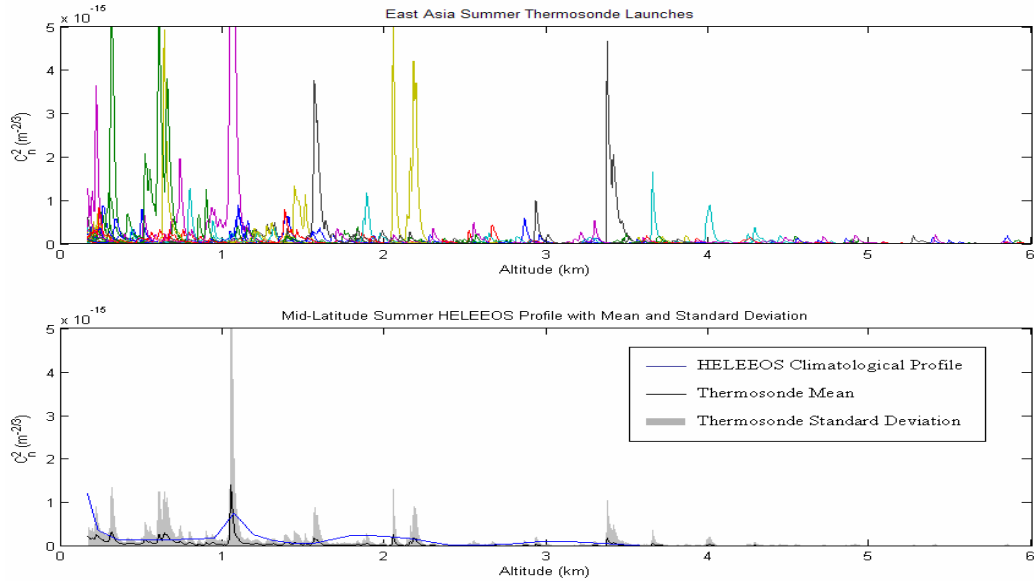


Figure 13: Comparison of the East Asia summer thermosonde data, which was collected at night, to the HELEEOS correlated  $C_n^2$  climatology. The top plot is each raw thermosonde profile, and the bottom contains the HELEEOS correlated climatology in comparison with the mean and standard deviation of  $C_n^2$  over all of the thermosonde data.

All of these minor discrepancies are accounted for by the procedure used to calculate the correlated  $C_n^2$  climatology. As mentioned previously, the atmosphere was divided into altitude layers or slabs. These layers had to be thicker, consequently sacrificing resolution, because there was an insufficient amount of thermosonde data to be analyzed. The greater initial peak is a consequence of binning the lower altitudes, with higher  $C_n^2$  values, together with the lower optical turbulence values at higher altitudes. Therefore, the initial peak is capturing the greater optical turbulence values from the surface and using them at higher altitudes. There are two smaller and broader peaks that occur at 2 and 3 km, which could have been produced for one of two reasons. First, the peaks encompass several spikes in  $C_n^2$ , where these smaller spikes probably create a higher mode value in the distribution because they were binned with lower magnitude values. Thus, they produced a higher  $C_n^2$  value for the particular altitude layer.

However, HELEEOS calculates correlated  $C_n^2$  climatologies based on the ExPERT tables of temperatures and relative humidities and their corresponding optical turbulence value. An assumption was made that the thermosonde data were collected under average conditions. If the actual weather conditions were not average, that could also account for the larger values of  $C_n^2$  than those collected by the thermosonde. As for the rest of the profile, it falls within one standard deviation of the mean  $C_n^2$ , which makes the HELEEOS climatological profile a legitimate representation of the data.

On the other hand, there is a little more disagreement between the desert summer profile produced by HELEEOS and the corresponding thermosonde data, which is illustrated in Figure 14. The discrepancy within the boundary layer is most likely a consequence of how HELEEOS models the boundary layer and the data tables it uses to find the mode  $C_n^2$  value for the given atmospheric parameters.

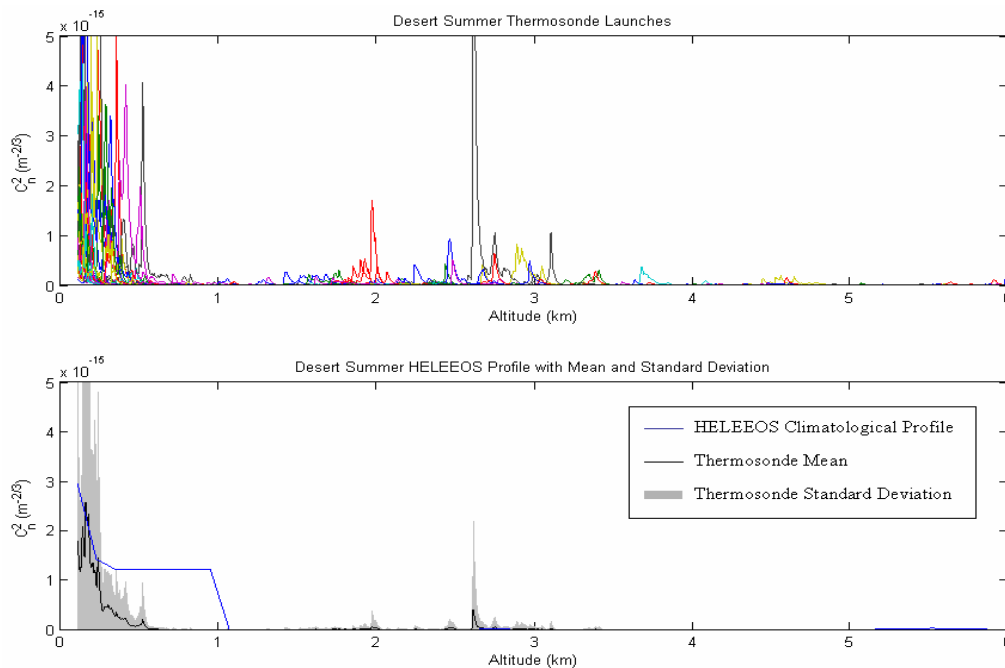


Figure 14: Comparison of the desert summer thermosonde data with the correlated  $C_n^2$  climatology. The top plot is each raw thermosonde profile, and the bottom contains the correlated climatological profile with the thermosonde data mean and standard deviation.

To properly interpret this comparison, it is important to note that the boundary layer height for this scenario was 1000 m for the time period of 21:00 to 00:00. HELEEOS predicts that optical turbulence is a constant value from about 0.4 km to 0.9 km, but the real data do not show this trend. For the first few hundred meters, the climatological profile does not deviate much from the mean  $C_n^2$  profile, which means that the database for the first boundary layer slab accurately predicts optical turbulence values. However, for the second slab, there were simply not enough data at larger relative humidities for these higher altitudes, so the same mode value of  $C_n^2$  for the 60-65% relative humidity (RH) bin was also used for the 95-100% RH bin and every one in between. Table 8 in the appendix illustrates the lack of data within the boundary layer. In the free atmosphere, the mode value of  $C_n^2$  is found according to the temperature, and it is approximately two orders of magnitude lower at 1.1 km for the average temperature value than at 0.9 km for the average RH value. Despite this discrepancy, the remainder of the profile falls within one standard deviation of the mean. It is important to note for the previous two figures, that HELEEOS is not reproducing the campaign launch conditions, but rather is given similar input parameters to estimate an optical turbulence profile for the given average conditions.

As for the plots for the other scenarios, mid-latitude winter and both desert winter locations, they compare similarly to that of the mid-latitude summer site. For completeness and to avoid redundancy, these can be found in the appendix. Even though there were not enough physical data to reproduce completely realistic profiles for each campaign location, the HELEEOS correlated climatological profiles for each corresponding ExPERT location generally fall within one standard deviation of the mean

thermosonde  $C_n^2$  value. Overall, it has the flexible capability to estimate optical turbulence profiles for different temperatures and relative humidities, which makes it a valuable and versatile tool.

### **4.3 Standard vs. Climatological models**

Standard models are the most widely used among the Department of Defense to characterize optical turbulence profiles. Since they are the simplest of the three types examined in this study, they are very easy to use. Again, these models only contain one equation or a system of equations that require a minimal number of input variables, such as altitude or windspeed, to calculate  $C_n^2$  vertical profiles. Another factor which contributes to their widespread use is that these equations can be found in several common atmospheric optical turbulence reference books. The equations for each of the different profiles were derived by fitting a curve to physically collected data, but because they have few atmospheric inputs, their simplicity becomes a limitation.

Even though this limitation exists, these profiles are still commonly used. The curves only capture the most basic trends in the  $C_n^2$  data and do not have much flexibility for atmospheric variations. The degree to which these profiles have been simplified is easily seen in Figure 15. Initially, the Hufnagel-Valley 5/7 profile is approximately an order of magnitude greater than the standard deviation. It does not really capture any of the physical data within the first half of the boundary layer, 0.5 km. Though HV 5/7 sometimes falls within the mean and standard deviation in the upper part of the boundary layer and above, there are occasions where the profile remains greater than it. The literature states that this model is really only valid for mid-latitude locations because it assumes a low tropopause and was actually developed using mid-latitude thermosonde

data, but as seen in Figure 15, it does not accurately model the boundary layer, and produces  $C_n^2$  values greater than the standard deviation in the lower upper air region.

(Beland 1993)

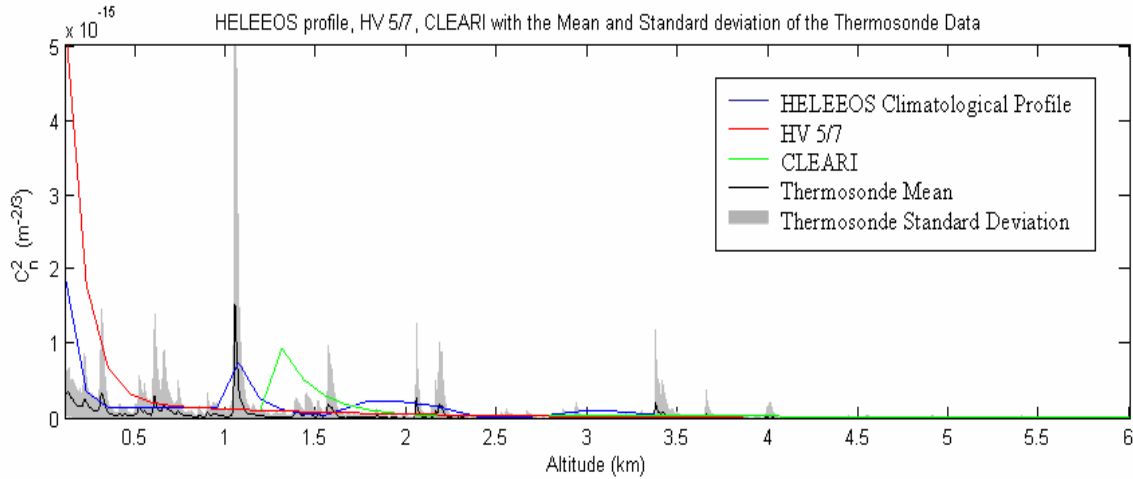


Figure 15: Mid-Latitude summer HELEEOS climatological profile, Hufnagel-Valley 5/7, and CLEARI superimposed over East Asia Summer thermosonde mean  $C_n^2$  and Standard Deviation.

As for the CLEARI model, it falsely predicts a spike at 1.3 km. This is because the model is only valid at 1.23 km, the distance of White Sands Missile Range above mean sea level, and when HV 5/7 is added on as an extension to model  $C_n^2$  at lower altitudes, the model produces this feature. However, the initial part of the profile was determined under higher altitude boundary layer conditions. This implies that CLEARI could more accurately predict optical turbulence values if it was not referencing altitudes above mean sea level, but instead above the surface. Also, CLEARI was developed under higher-altitude desert summer conditions with all of the data collected at night, so it should more accurately model optical turbulence values for that particular scenario.

For the next part of the investigation, the objective was to observe how the standard models actually compared with changes in atmospheric conditions. Shown in Figure 16 are the comparisons between the climatological profiles produced by HELEEOS and these standard models.

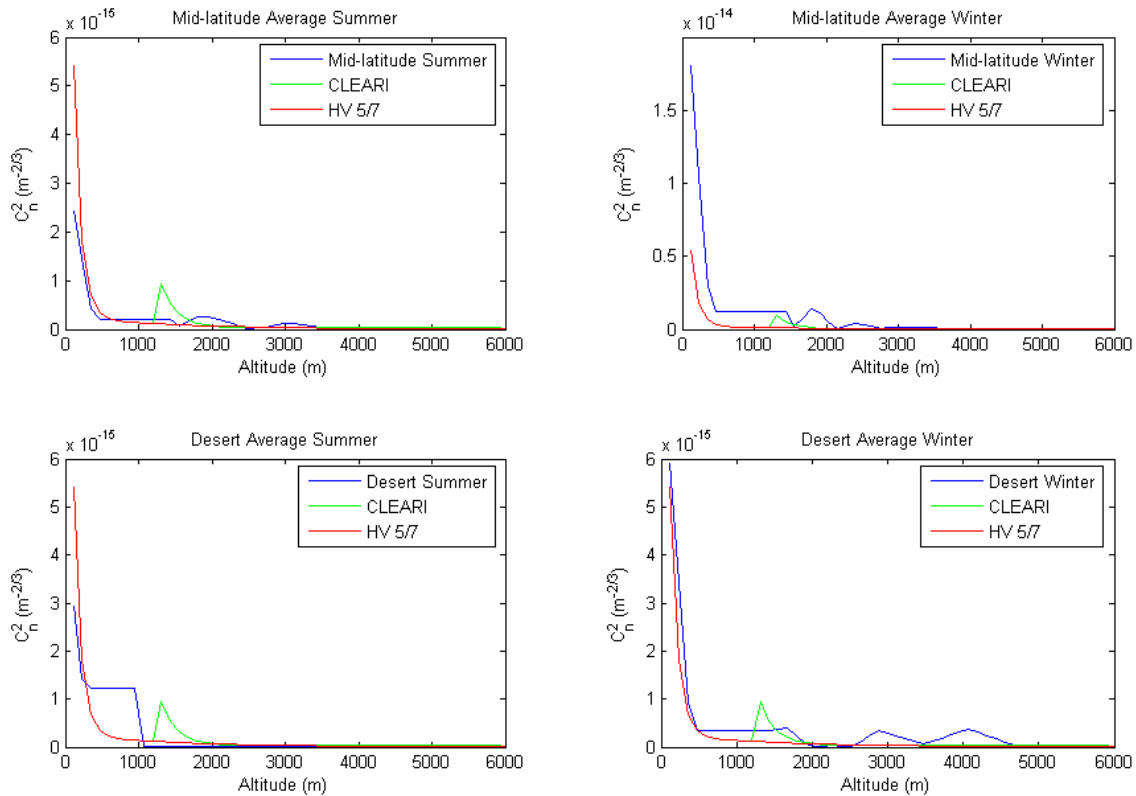


Figure 16: Comparisons of the HELEEOS climatological profiles for the 50<sup>th</sup> percentile RH with the standard models of Hufnagel-Valley 5/7 and CLEARI; East Asia Summer (top left), East Asia Winter (top right), Desert Summer (bottom left), Desert Winter (bottom right). The boundary layer height for the profiles is 1524 m. Note that the Mid-Latitude winter  $C_n^2$  vertical scale is larger than the others.

The initial mid-latitude summer profile is about half the value of Hufnagel-Valley 5/7, but at approximately 300 m, they are very similar in magnitude and shape. On the other hand, the mid-latitude winter profile is initially three and a half times greater than Hufnagel-Valley 5/7, and remains greater than it throughout the boundary layer. As for the desert summer profile, the Hufnagel-Valley 5/7 profile is 50% greater than the

climatological profile, but at approximately 400 m, the climatological  $C_n^2$  profile stays about an order of magnitude greater than the other for the remainder of the boundary layer. The desert winter profile and Hufnagel-Valley 5/7 profiles compare very well throughout the boundary layer, so Hufnagel-Valley 5/7 profile is a good estimate of a desert winter 50<sup>th</sup> percentile relative humidity  $C_n^2$  profile.

The differences in optical turbulence due to the change in season can be explained by radiative transfer properties. Radiation from the earth's surface and atmosphere generally tends to radiate away from the earth towards space. Since the earth's surface and atmosphere are warmer and contain more moisture during the summer, the radiation does not propagate as easily through to the top of the atmosphere. This process results in more evenly distributed energy, which then leads to smaller temperature gradients and smaller optical turbulence values. During the winter months, the ground and air are colder and hold less moisture. Therefore, larger amounts of radiation can escape into space. Due to the lack of moisture that evenly distributes the energy throughout the atmosphere, there are larger temperature gradients, which, in turn, produce larger  $C_n^2$  values.

HELEEOS also has the capability to predict optical turbulence profiles for more extreme weather conditions. Figure 17 illustrates the different profiles for 10<sup>th</sup>, 50<sup>th</sup>, and 95<sup>th</sup> percentile relative humidity conditions. A similar analysis to the seasonal changes in optical turbulence can be applied to changes in relative humidity. In general, 10<sup>th</sup> percentile relative humidity  $C_n^2$  values should be the largest, and the 95<sup>th</sup> percentile values should be the smallest. Again, this is because the higher moisture content reduces temperature gradients and lowers  $C_n^2$ . This explains how the greatest optical turbulence

profile corresponds to the 10<sup>th</sup> percentile relative humidity, the middle is the 50<sup>th</sup> percentile, and the smallest magnitude is the 95<sup>th</sup> percentile relative humidity profile.

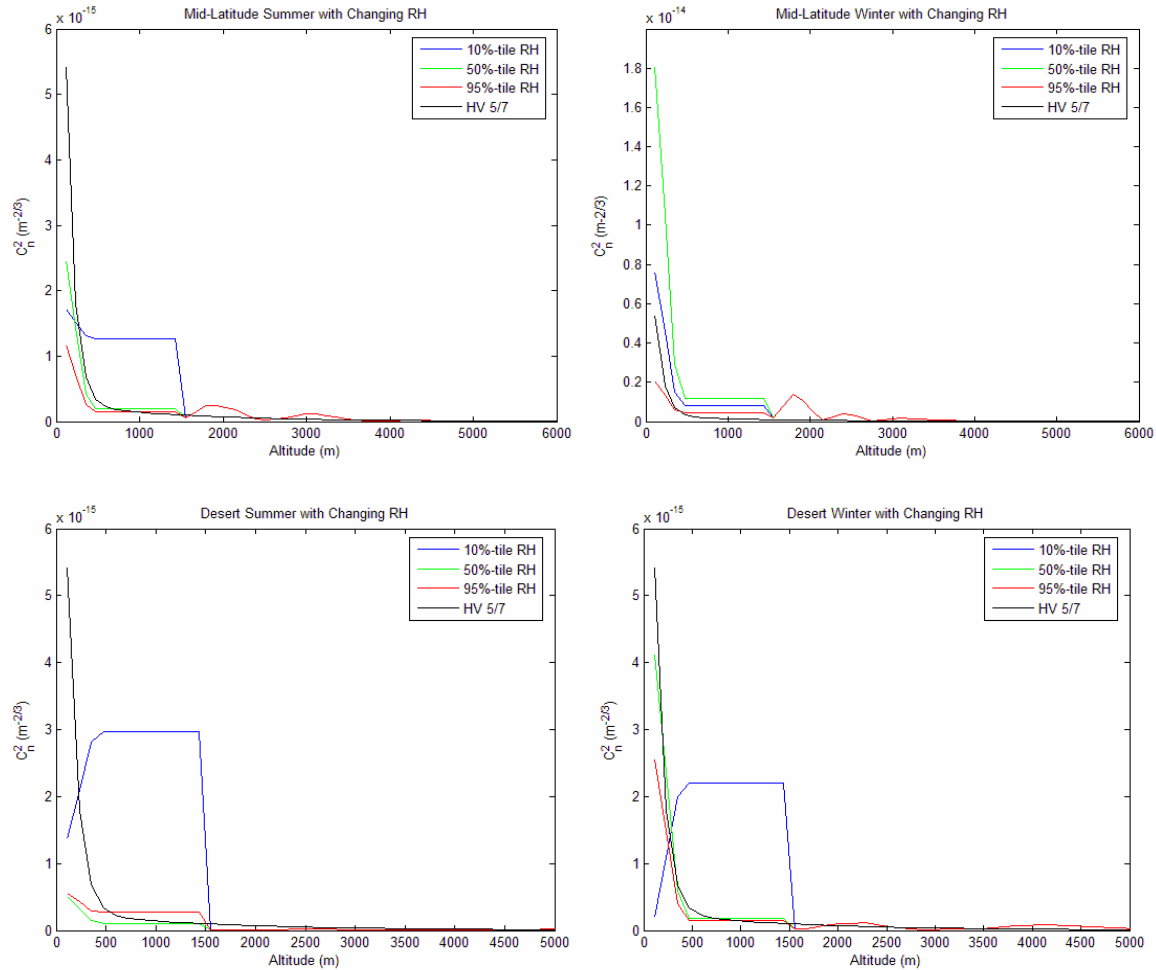


Figure 17: Mid-Latitude and desert summer and winter optical turbulence profiles for 10<sup>th</sup> percentile, 50<sup>th</sup> percentile, and 95<sup>th</sup> percentile relative humidity plotted against Hufnagel-Valley 5/7.

The deviations from the radiative transfer theory predications for the magnitudes of  $C_n^2$  for each profile are effects of the lack of thermsonde data. Since all of the bins that compose the climatological profile did not contain log-normal distribution coefficients, the data from the nearest bin were used to fill in the empty ones. Thus, it is entirely possible that a high value of  $C_n^2$  could occupy a 95<sup>th</sup> percentile relative humidity bin or a

lower  $C_n^2$  value in a 10<sup>th</sup> percentile bin. For both of the summer and winter desert sites, the 10<sup>th</sup> percentile RH  $C_n^2$  profiles increase within the boundary layer, which is counter to the normal decay of optical turbulence values. One explanation for this could be an effect from a temperature inversion within the desert boundary layer. Another, and the most likely, is this is an effect of the binning process. Since there were not enough data to fill all of the relative humidity bins, the empty ones are filled with the nearest bin data. The only method to resolve this inversion is to similarly analyze more optical turbulence data under these lower relative humidity conditions.

#### **4.4 Statistical vs. Climatological Models**

Statistical models have one significant advantage over the ones previously mentioned because they can simulate the random variations and peaks in climatological optical turbulence values. The particular model used in this study, ATMtools, takes an existing standard model or some other  $C_n^2$  vector and randomizes it. Researchers use this technique in hope of producing a profile with more realistic features. Accurately reproducing typical thermosonde profiles using statistical models would be a powerful tool for optical turbulence prediction.

##### ***4.4.1 Analysis of statistically derived $C_n^2$ distributions***

The first task to accomplish for this model is to confirm the type of Gaussian distributions that are produced for a given altitude layer. Since the analysis done to develop the HELEEOS climatological profile found that the physical  $C_n^2$  distributions were log-normal, a type of skewed Gaussian, then the statistical model should also produce log-normal distributions to emulate the physical data. The function in ATMtools

that calculates optical turbulence profiles uses zero-mean Gaussian randomized numbers to enhance the input  $C_n^2$  vector by randomizing its entries. To confirm this technique, distributions are produced for the altitude layers, 100-400m, 400-700m, and 700-1000m. An interesting observation is the distributions for the first layer are all lognormal, as seen in Figure 18.

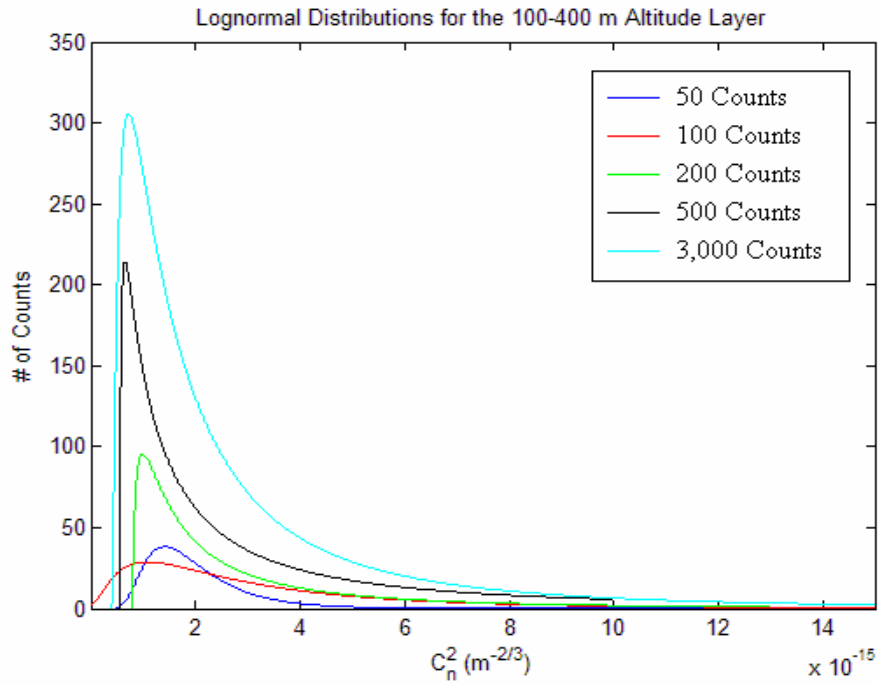


Figure 18: Enhanced Hufnagel-Valley 5/7 profile distributions for 100-400 m.

This is a consequence of the shape of the HV 5/7 distribution, and the exponential decay within the boundary layer is the cause. Since the optical turbulence values are decreasing much more quickly than the altitude values are increasing, there are greater variances in the  $C_n^2$  values, which produce a skewed distribution. Even when the number of counts is increased to 3,000, the distribution is never a normal Gaussian function. For the rest of the profile, the altitude values are increasing more quickly than the  $C_n^2$  values are decreasing, and the distributions become normal Gaussians.

#### 4.4.2 Comparison of the statistical and climatological distributions

The next goal is to observe the kind of optical turbulence distributions the statistical model produced against the climatological ones. To make the best possible comparison, similar conditions to that of the thermosonde distributions are closely mimicked for the input parameters to the statistical model. Using an identical altitude layer to one of those defined for the HELEEOS correlated  $C_n^2$  climatological model, the statistical model enhances the Hufnagel-Valley 5/7 and CLEARI profiles, and the distributions are calculated. Statistics are then used to analyze two of the different randomized profiles.

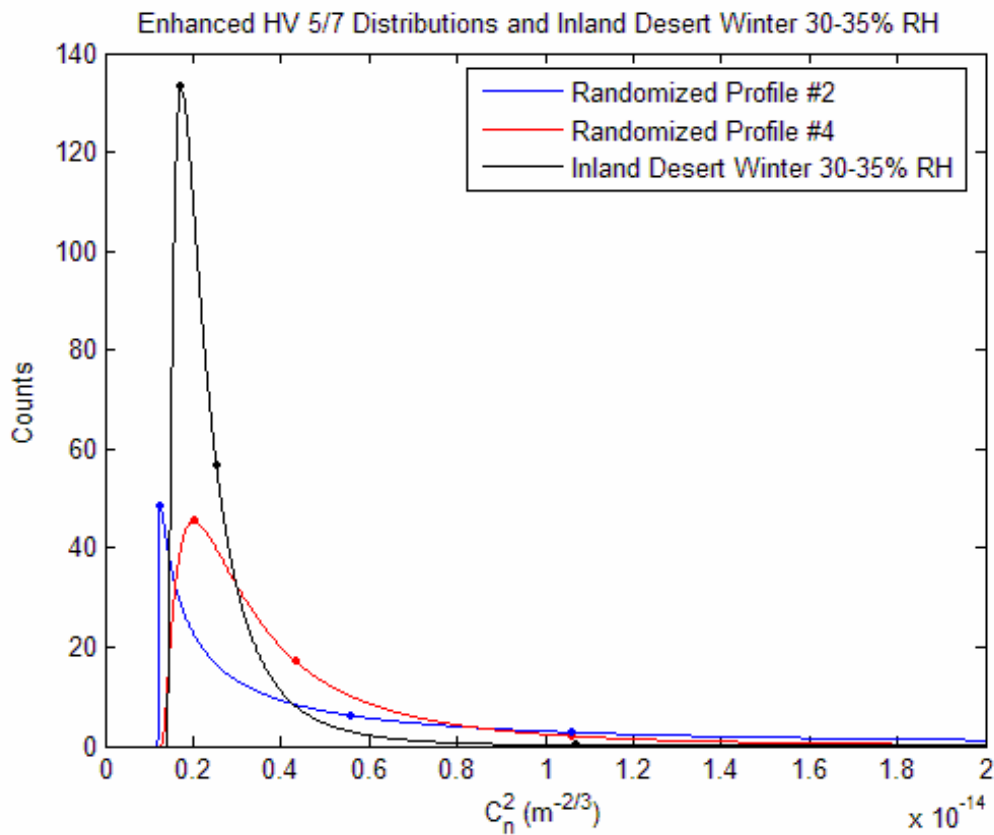


Figure 19: Two enhanced Hufnagel-Valley 5/7  $C_n^2$  distributions and the 30-35% relative humidity distribution for one of the desert winter locations in the boundary layer.

Since the distributions are calculated from the same vector size, the area under each curve is approximately the same. Each distribution has its own set of statistics, which are displayed in Table 6.

Table 6: The statistics for each log normal distribution.

	<b>Randomize Profile #2</b>	<b>Randomized Profile #4</b>	<b>Desert Winter 30-35% RH</b>
<b>Area under the Curve</b>	1.05E-13	1.42E-13	1.59E-13
<b>Mode Value</b>	1.26E-15	2.04E-15	1.75E-15
<b>Median Value</b>	1.06E-14	1.06E-14	1.07E-14
<b>Mean Value</b>	5.60E-15	4.36E-15	2.56E-15

The areas under each curve are approximately equal to one another, which is what one would expect with similar distribution sizes. Also, the median values are equal because of the distribution boundaries. For these distributions, the right end point is  $2 \times 10^{-14}$  and the left is approximately  $1 \times 10^{-16}$ , and therefore, the median value is half the distance between the end points. The mode values are close to one another, and the difference between each can be seen in the peaks of each plot. However, the magnitude of the desert mode is approximately three times greater than the magnitudes of the randomized distributions. As for the mean, these values are the farthest apart, and the difference can also be seen in Figure 19.

The next distribution comparison is between the enhanced CLEARI and HV 5/7 and two mid-latitude climatological profiles. The commonalities between them are the altitude layer, 9-10 kft, and the number of counts. As one can see from Figure 20, the climatological distributions are approximately six times greater in magnitude than the Gaussian distributions. Another feature is the shape of the log-normal curve in contrast

to the Gaussian distribution. A lognormal curve is a skewed Gaussian, and the degree of this feature is clearly illustrated in Figure 20.

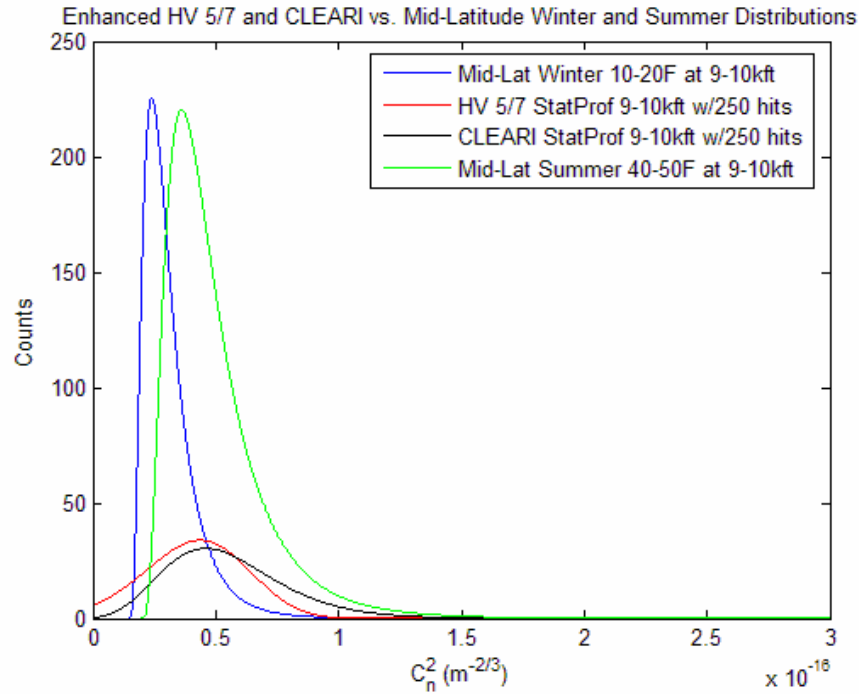


Figure 20: Enhanced Hufnagel-Valley 5/7 and CLEARI profiles with East Asia winter at 10-20 °F and East Asia summer at 40-50 °F from 9-10kft (the free atmosphere) for random distribution #4.

Comparing the distributions of  $C_n^2$  values helps to determine whether or not the statistical model is realistically randomizing them. The distributions of the statistical model in the boundary layer are the most similar to the climatological distributions, but the distributions for the statistical model in the free atmosphere are not skewed Gaussians, and they do not mimic climatology. The smaller numbers of counts for the mode value of the CLEARI and HV 5/7 profiles are most likely a consequence of the profile's shape. Also, the magnitude of the variations in  $C_n^2$  is much less than the physical variation. Since the statistically enhanced distributions are slightly different than the climatological ones, it is important to observe the statistical profile trend against

the physical one. Therefore, five mid-latitude summer HELEEOS climatological profiles with several of the corresponding thermosonde launches were plotted together, and this relationship can be seen in Figure 21.

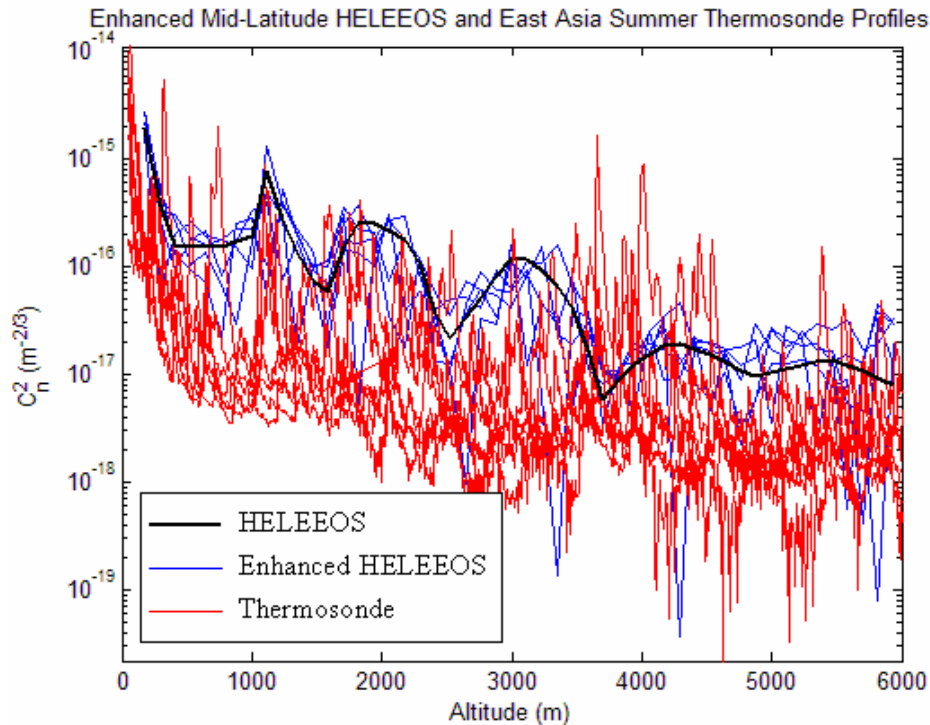


Figure 21: Enhanced Mid-latitude Summer climatological profile with the corresponding East Asia thermosonde profiles.

The blue lines represent the statistically randomized correlated  $C_n^2$  climatological profile, and one can see that the distribution about the original profile, the black line, is a normal Gaussian. However, there are a few values that stray from the normal distribution, and two of them are approximately an order of magnitude smaller than the lowest thermosonde  $C_n^2$  values. The lognormal distribution of the thermosonde data is also clearly seen in the figure. It has a lower, more populated base line (in the range of  $10^{-18}$  and  $10^{-17}$ ), with significant fluctuations in  $C_n^2$ , which are larger in magnitude than the base.

## 4.5 Numerically Derived vs. Climatological Models

Since the version of DEEST available for this study was not functioning properly, sample profiles obtained from Sara Adair, one of DEEST's developers, and another given in a briefing at a Directed Energy Professional Society (DEPS) conference are used for the analysis instead. The first comparison is depicted in Figure 22, and it shows the differences between the climatological and DEEST  $C_n^2$  profile. This particular set comes from MM5 data for specified East Asia and desert locations, which are comparable in scenario to the thermosonde launches, though not for the specific dates of the launches.

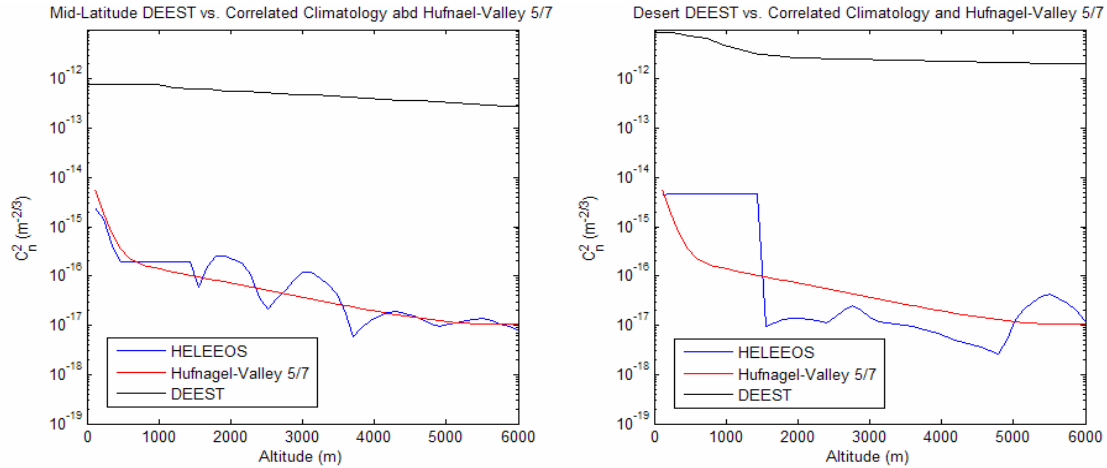


Figure 22: A comparison of the DEEST optical turbulence profiles for East Asia and Desert summer MM5 data, the HELEEOS correlated optical turbulence climatological profile for the corresponding ExPERT sites, and the Hufnagel-Valley 5/7 profile.

As one can see, the DEEST profile is much larger than the HELEEOS climatological and Hufnagel-Valley 5/7 profiles by two to three orders of magnitude. As previously shown in Figure 15, the HELEEOS profile represents the thermosonde data rather well, even though it is slightly larger than the standard deviation at times. Therefore, the DEEST profile must also be several orders of magnitude greater than the physical data. In this case it does not represent the optical turbulence data for these locations.

The second example of a DEEST profile is illustrated in Figure 23. The physical data were collected around 22:00, approximately the same time frame as the ABL campaign thermosonde launches.

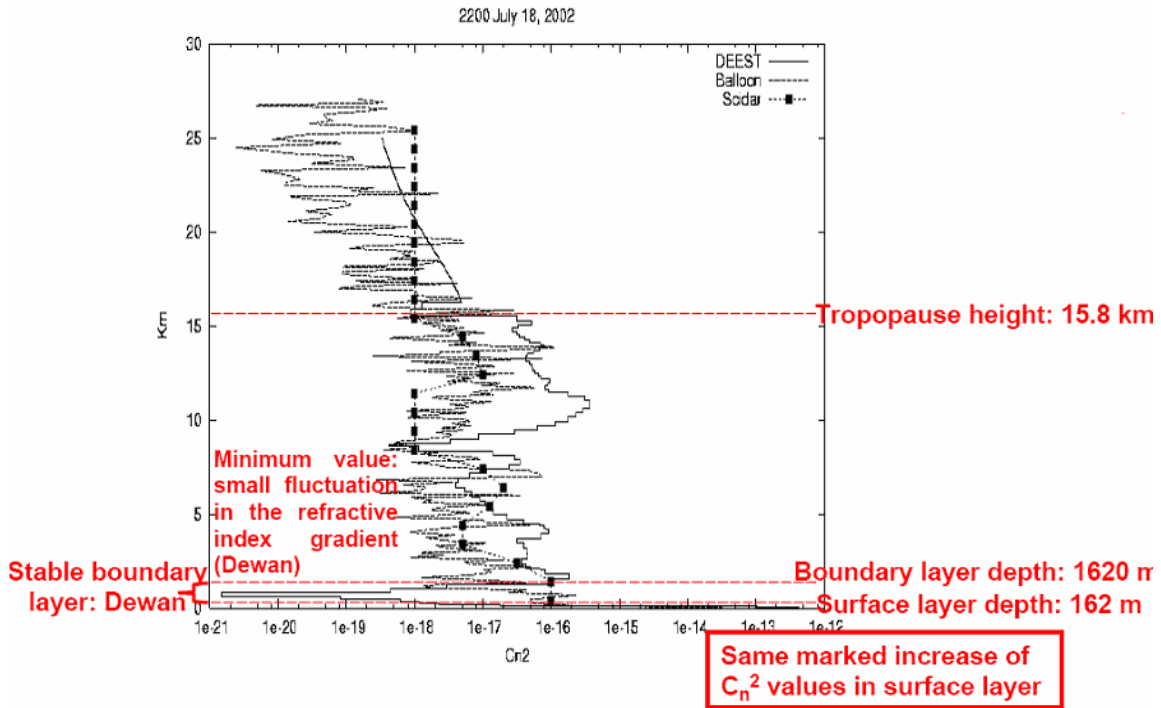


Figure 23: DEEST profile for 22:00 July 18, 2002 compared to corresponding balloon and scidar profiles. [Adapted from Adair, 2005]

As one can see, this DEEST generated profile captures the data slightly better than the profiles in the previous figure because there is a range from approximately 5 km to 10 km where the DEEST profile has values within the same order of magnitude as the thermosonde values. As for the remaining altitudes, the profile is one to two orders of magnitude greater. In the boundary layer, DEEST predicts that there is an extreme drop in  $C_n^2$ , which is on the order of  $10^{-21}$  in magnitude. According to the thermosonde data in Figure 23 and the other profiles analyzed previously, this feature is completely

unrealistic. In the lower troposphere the profile is slightly greater in magnitude than the physical data, and from approximately 5 km to 8 km, the profile falls within the balloon  $C_n^2$  profile. However, in the upper troposphere the DEEST prediction of optical turbulence values ranges anywhere from one to two orders of magnitude greater than the physical data.

Overall, the DEEST profiles generally do not represent realistic optical turbulence values for the profiles used in this study. The first example showed  $C_n^2$  values several orders of magnitude larger than measured values for the East Asia and desert summer scenarios. The second example shows a random, unrealistic drop on the order of  $10^{-21}$  in value within the boundary layer, and estimates values of optical turbulence that are one to two orders of magnitude greater than the thermosonde data in the upper troposphere.

Another example of numerically derived  $C_n^2$  values is a model called NSLOT. It was derived by Frederickson and Davidson using Monin-Obukhov Similarity theory, and it was verified by a study in collaboration with NPS. The NSLOT model was developed from the same study previously discussed in the DEEST boundary layer models section and is currently in the process of being implemented into HELEEOS to provide maritime surface layer  $C_n^2$  profiles. Therefore, a comparison between the HELEEOS correlated  $C_n^2$  climatological and NSLOT profiles can be made. The first comparison is for corresponding desert summer land and sea locations and is illustrated in Figure 24.

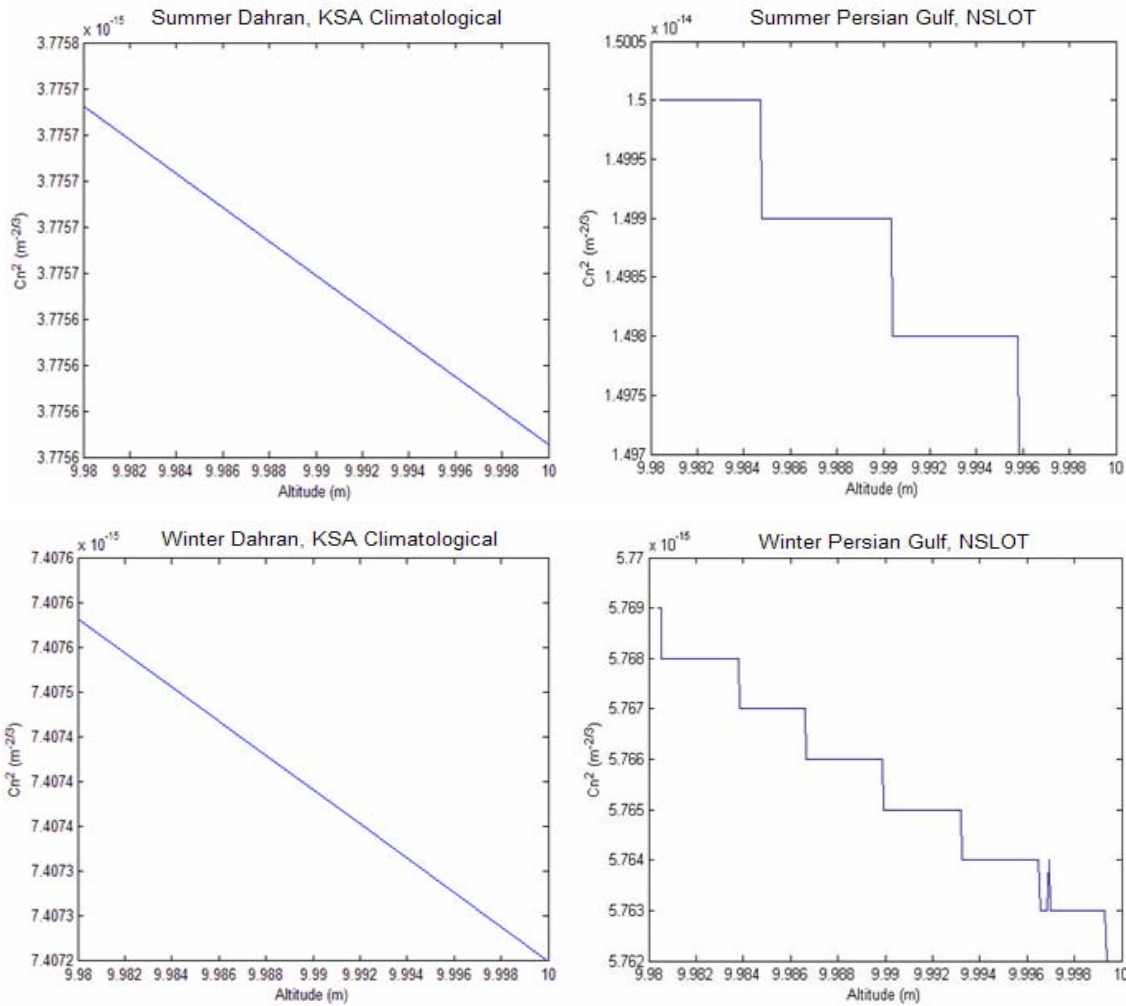


Figure 24: Climatological profiles (right) for coastal desert summer and winter locations and NSLOT profiles (left) for oceanic locations near the ExPERT site. The geometry for this scenario is a 1 km slant range with the target and platform 10 m above the surface.

For this comparison the correlated climatological profile is produced for the ExPERT site, Daharan, Kingdom of Saudi Arabia, and the NSLOT data come from off the coast in the Persian Gulf. Besides having different shapes, the optical turbulence profiles between the climatological and NSLOT profiles, in general, are not drastically different, especially for the winter case. However, they are different because NSLOT was developed over water, and the climatological data were collected over land. The summer NSLOT profile is approximately seven times greater than the climatological. As discussed in 2.6.5, the

air-sea temperature difference plays a role in the output  $C_n^2$  profile. This summer scenario has an air-sea temperature difference of -0.3, which falls within the region close to zero where the values are sensitive to small errors (Hammel et al., 2005). For the winter case, the correlated climatological profile is only two times greater than NSLOT. This scenario has an air-sea temperature difference of -0.9. Therefore, the produced  $C_n^2$  values realistically model the physical values. In any case, the numerically-produced optical turbulence profiles for NSLOT compare well to the correlated climatology in HELEEOS for this desert scenario because the profile values are within an order of magnitude, due to of the unstable meteorological conditions.

The second correlated  $C_n^2$  climatological and NSLOT comparison is data calculated from the ExPERT site, Pyongtaek, Korea, and from numerical atmospheric data off the coast of Korea in the Yellow Sea. It is a comparison of both mid-latitude summer and winter profiles, and is shown in Figure 25. Again, the NSLOT summer profile is approximately seven times greater than the climatological profile. The summer scenario has an air-sea temperature difference of 0.9, which implies that the estimated  $C_n^2$  values are larger than scintillometer-derived climatological optical turbulence values. Under these stable conditions there is a large amount of uncertainty in the  $C_n^2$  values, making them unreliable (Hammel et al., 2005). On the other hand, the winter data are very similar. The slopes of the profiles are slightly different, but the values are within the same magnitude range of approximately  $2 \times 10^{-15} \text{ m}^{-2/3}$ . However, the air-sea temperature difference is zero, so there are small uncertainties in the optical turbulence values for this profile. Therefore, they could be more different than what the comparison shows. These profiles for this North Mid-Latitude location agree within an order of magnitude.

Therefore, these findings support and validate the correlation technique, relating  $C_n^2$  values to meteorological parameters, used in HELEEOS.

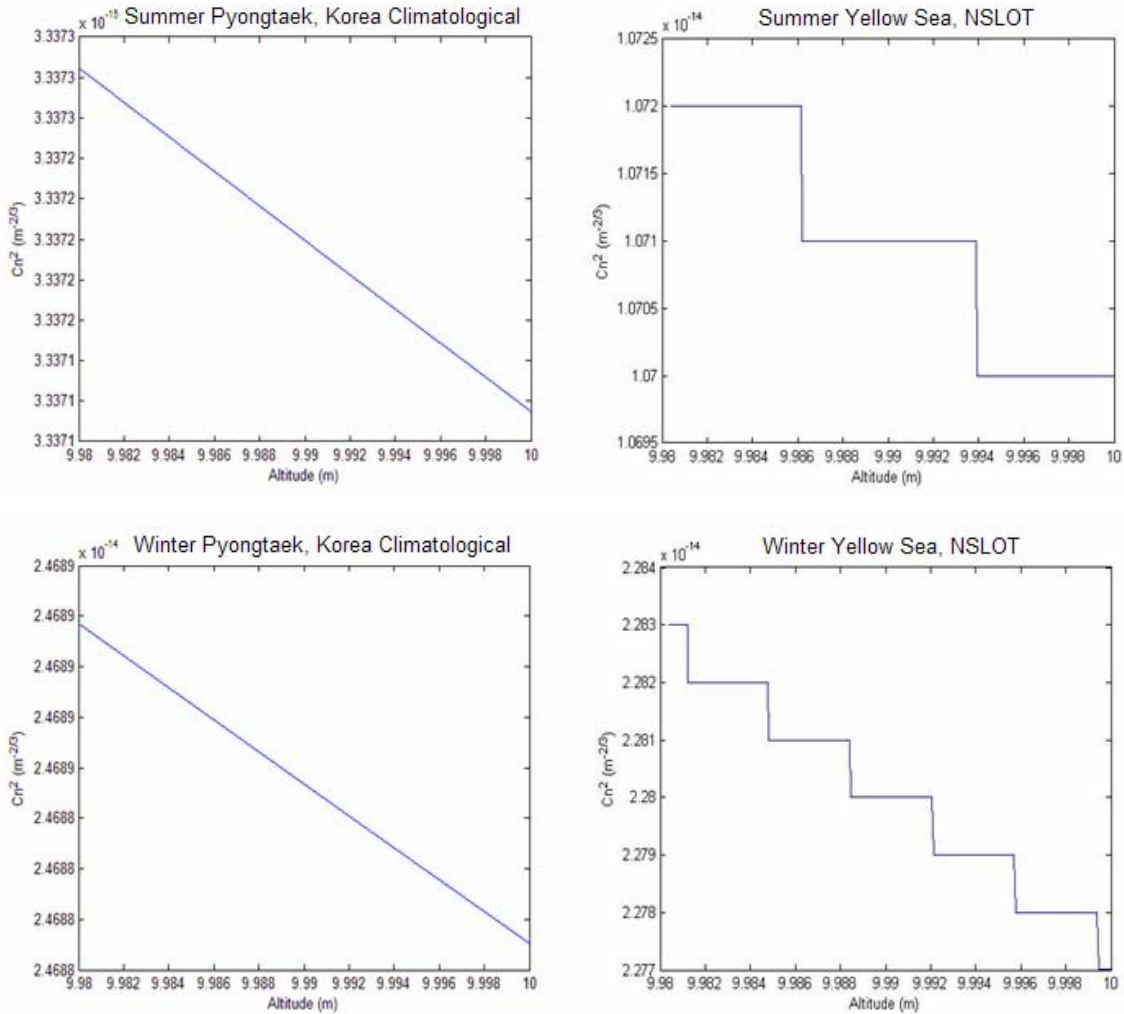


Figure 25: Climatological profiles (right) for coastal mid-latitude summer and winter locations and NSLOT profiles (left) for oceanic locations near the ExPERT site. The geometry for this scenario is a 1 km slant range with the target and platform 10 m above the surface.

#### 4.6 Air Force Applications

Previously in this chapter, it was shown in Figure 16 that the Hufnagel-Valley 5/7 and the correlated  $C_n^2$  climatological models do not always predict the same values of optical turbulence. Since they estimate different values of  $C_n^2$  along a high energy laser

beam propagation path, this could have a significant effect on the prediction of the system's performance. For the mid-latitude summer location, the Hufnagel-Valley 5/7 profile is generally comprised of greater values of  $C_n^2$  than the correlated optical turbulence climatology, except for at the top of the boundary layer, where they are approximately the same magnitude. Throughout the boundary layer and above, the mid-latitude winter correlated climatological profile is always greater. In the desert location, the Hufnagel-Valley 5/7 profile is initially larger than the correlated climatological one, and then the climatological remains greater throughout the remainder of the boundary layer. As for the DEEST numerically-generated optical turbulence profiles, they estimate  $C_n^2$  values that are several orders of magnitude larger than Hufnagel-Valley 5/7 and the HELEEOS correlated climatology. This result should have a greater impact on HEL system performance predictions. Profile estimates produced using NSLOT should have a more comparable system performance prediction to those of the HELEEOS correlated  $C_n^2$  climatology. The parameter, required dwell time on target, is used to quantify the variations in HEL system performance due to the differences in optical turbulence profiles. Higher values of optical turbulence indicate greater beam distortion, which suggests that the required dwell time on a target should be longer to achieve the desired effect and vice versa for smaller values of  $C_n^2$ . When calculating the dwell time on a target, the optical turbulence closer to the platform is weighted more than  $C_n^2$  at the target.

Table 7 provides a tabular summary of the required dwell times for the different optical turbulence profiles used to predict a HEL engagement scenario. It is important to

note that none of these scenarios are applying adaptive optics, the laser power is only 50 kW, and the aperture size is only 0.5 m.

Table 7: A tabular summary of required dwell times for an East Asia summer location using each of the standard and numerical profiles and the correlated  $C_n^2$  climatology for 3 various scenarios: Low- altitude with a 10 km slant range; High-altitude with a 90 km slant range; Surface layer with a 5 km slant range. All scenarios use a 50 kW laser with a wavelength of  $1.06\mu\text{m}$  with an aperture size of 0.5 m.

	<b>Low-Alt. 10km Slant Range</b> Platform Alt. 1525 m Target Alt. 0 m	<b>High-Alt. 90km Slant Range</b> Platform Alt. 6720 m Target Alt. 6725 m	<b>Surface Layer</b> Platform Alt. 20 m and Target Alt. 5m with 5 km Slant Range
<b>HV 5/7</b>	14.3857	330.5797	25.6207
<b>CLEARI</b>	16.0457	336.8904	25.6207
<b>HELEEOS 10%</b>	22.5791	493.9823	2.7728
<b>50%</b>	14.4122	492.2955	4.9588
<b>95%</b>	58.874	490.6146	0.40806
<b>DEEST (over land)</b>	3.71E+04	5.19E+06	2.9155E+03
<b>(over water)</b>	3.10E+05	1.35E+08	2.7271E+04
<b>NSLOT</b>			1.5074

The first scenario is a low-altitude engagement, where the platform height is the top of the boundary layer, the target is on the surface, and the slant range is 10 km. There are only a few seconds difference between Hufnagel-Valley 5/7 and the CLEARI profiles because the calculations take into the account the spike in  $C_n^2$  caused by the extension of CLEARI to the surface with Hufnagel-Valley 5/7. The differences in dwell time between the 10<sup>th</sup> and 50<sup>th</sup> percentile RH are what one would expect from turbulence. The dwell time for the 10<sup>th</sup> percentile is longer than the 50<sup>th</sup> percentile RH because of higher  $C_n^2$  values. The long dwell time for the 95<sup>th</sup> percentile RH is an effect of molecular and aerosol scattering. The DEEST profile predicts dwell times that are two to three orders of magnitude greater than the required dwell times using the other optical turbulence profiles.

For the second scenario the platform altitude is at a height of 7,620 m and the target was at 7,625 m with a slant range of 90 km between the two. Again, adaptive optics are not used in this scenario, so the required dwell times are longer than they would be in a real engagement scenario. There is a six second difference in required dwell time between Hufnagel-Valley 5/7 and CLEARI. The correlated  $C_n^2$  climatologies for the various relative humidities do not have much of an effect on required dwell time because relative humidity is approximately zero in the free atmosphere. Therefore, the 160 s difference in required dwell time between the standard profiles and the correlated  $C_n^2$  climatology profiles is simply an effect of the differences in profile magnitude at this altitude. As for the required dwell time using the DEEST generated profile, it produces dwell times that are 3 to 5 orders of magnitude larger than both the standard models and the HELEEOS correlated  $C_n^2$  climatology.

The final scenario consists of the platform altitude at 20 m and the target altitude at 5 m above the surface with a slant range of 5 km. Hufnagel-Valley and CLEARI optical turbulence profiles predict the same required dwell times because they are the same profile for this surface layer scenario. The Hufnagel-Valley predicts a required dwell time of 25 seconds, which is 20 to 24 seconds longer than any of the times predicted by the HELEEOS correlated  $C_n^2$  climatologies and NSLOT profile. Previously in section 4.6, it was shown that the NSLOT profiles and the HELEEOS correlated  $C_n^2$  climatologies were very similar, and Table 7 confirms those results because their respective required dwell times on target are also very close in value. All of the required dwell times for these profiles are within 1 to 3.5 s of one another, which confirms the results of the previous section.

Table 7 shows that various optical turbulence profiles produce different system performance predictions. Earlier in section 4.3, the differences are not large between the values of optical turbulence between the standard profiles and the HELEEOS correlated  $C_n^2$  climatology, but they produced differences in required dwell time on the range of approximately 8 to 160 seconds. The NSLOT and the HELEEOS correlated  $C_n^2$  climatology comparisons show that the small differences in optical turbulence profiles produce small differences in system performance. As for the DEEST  $C_n^2$  profiles, the difference of two to three orders in magnitude between it and the standard and HELEEOS correlated climatology produced required dwell times three to four orders of magnitude greater. For completeness, a similar table for a desert summer location can be found in the appendix.

Given that there is such a variation in system performance between these profiles for one location, there must also be a worldwide variation between them. The following sets of figures examine the worldwide changes in HEL system performance prediction between the standard profile Hufnagel-Valley 5/7 and the HELEEOS correlated  $C_n^2$  climatology. Since HELEEOS uses an optical turbulence profile, where the values of  $C_n^2$  are correlated to relative humidity (and temperature), it has the ability to estimate optical turbulence profiles for other parts of the world based on a given location's climatology, and the Hufnagel-Valley 5/7 profile produces the same  $C_n^2$  values regardless of the location to which it is applied. Therefore, there should be a worldwide difference in required dwell times between the two optical turbulence profiles. These changes in system performance, due to the differences in optical turbulence profiles, are illustrated in Figure 26. The engagement scenario for Figure 26 has the platform at the top of the

boundary layer (1525 m) and the target on the ground. Therefore, the optical turbulence values for altitudes near the top of the boundary layer and the differences in  $C_n^2$  values between the two profiles at this location play significant roles in the outcome of the dwell time plot for each profile.

The color bars for the first two maps indicate the required dwell time in seconds, where the green indicates a shorter dwell time of approximately 0.25 s and the red a longer one of about 8 s. For the last map the color bar indicates the difference in required dwell time on target between the correlated  $C_n^2$  climatological model and Hufnagel-Valley 5/7. Yellow indicates that the two models predict roughly the same dwell time, and therefore the color has a value of 0. The greener dots indicate the climatological dwell times were shorter than Hufnagel-Valley 5/7, and vice versa for the red points.

Although the dwell time plots for the Hufnagel-Valley 5/7 and correlated  $C_n^2$  climatological profiles look almost the same, there are differences between the two. These differences are also what one would expect according to the analysis above. At the top of the boundary layer, the summer mid-latitude profile and Hufnagel-Valley 5/7 are very similar in value, and therefore, the difference in dwell time is approximately zero. As for the desert region, the summer climatological profile is slightly larger than Hufnagel-Valley 5/7. Thus, the scenario using the climatological profile resulted in a longer dwell time.

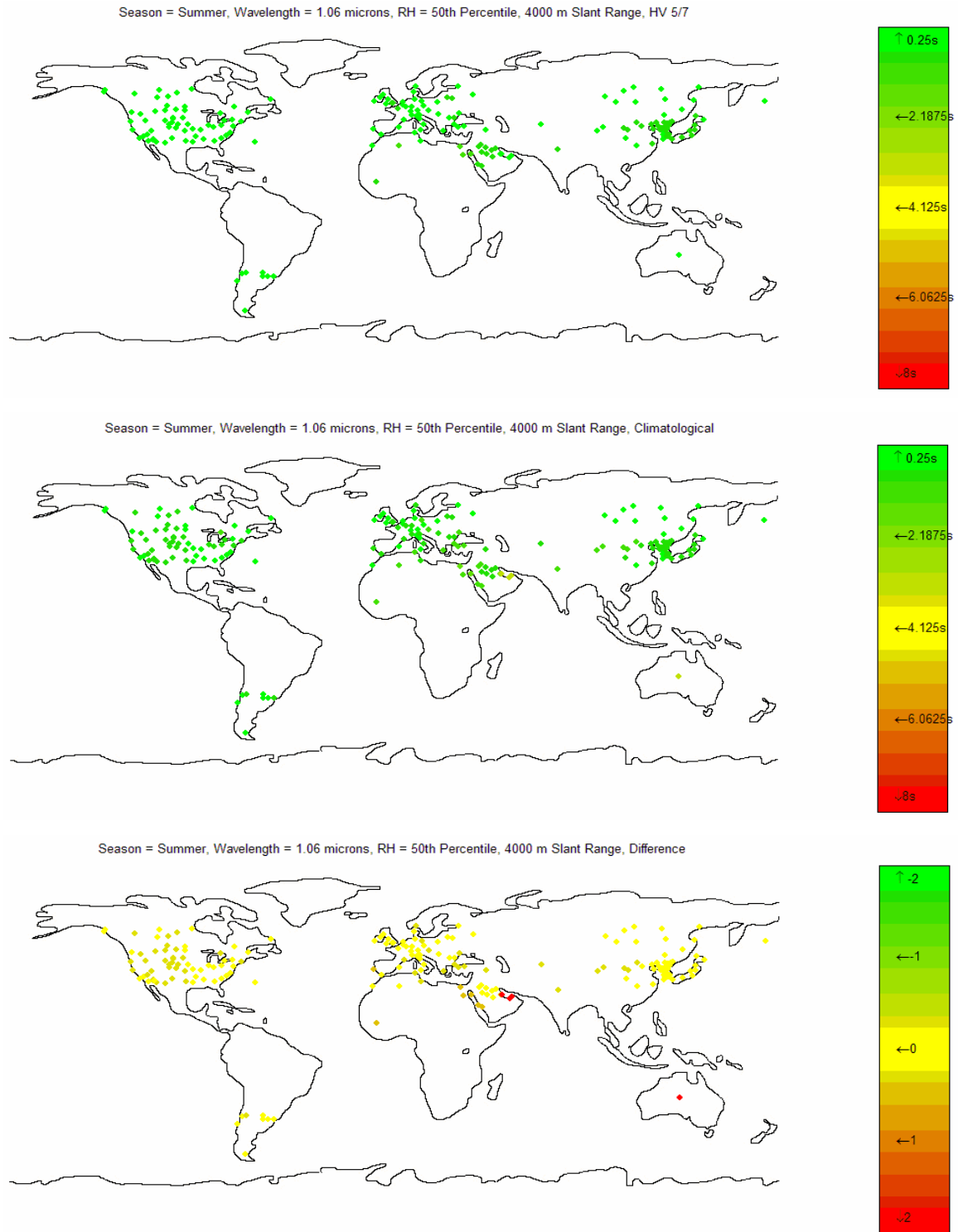


Figure 26: Worldwide map of required dwell times for all ExPERT Mid-latitude and Desert sites for the summer season, 1.06 $\mu$ m laser wavelength, 50<sup>th</sup> relative humidity percentile, and 4000 m slant range. Hufnagel-Valley (top), Climatological (middle), and the Difference (bottom)

The next figure illustrates the impact slant range has on required dwell time. The effects due to the differences in  $C_n^2$  profiles are amplified over a longer slant range, and it is shown in Figure 27 for slant ranges of 4000 m and 10,000 m. For the 4,000 m slant range, the difference between the two profiles for mid-latitude regions is approximately zero, but for the 10,000 m slant range there is a considerable change in predicted HEL system performance. This effect varies between ExPERT sites worldwide. In most cases, the climatological profile predicts a worst case scenario, but there are locations where the Hufnagel-Valley 5/7 profile predicts the longer dwell time. These plots show that it is important for future studies to properly characterize optical turbulence for given locations because the various profiles predict differences in the performance of a high energy laser system.

As seen previously in Figure 17, variations in relative humidity percentile within the boundary layer have an effect on the magnitude of optical turbulence values, and therefore, will also have an effect on HEL system performance. Figure 28 illustrates the differences in required dwell time on a target between Hufnagel-Valley 5/7 and the HELEEOS correlated  $C_n^2$  climatological profile. Again, this scenario is strictly within the boundary layer, and it uses a laser wavelength of 1.06  $\mu\text{m}$  over a 10,000 m slant range. The first map shows the difference between the 10<sup>th</sup> percentile relative humidity HELEEOS correlated  $C_n^2$  climatology and Hufnagel-Valley 5/7. Since the values of  $C_n^2$  are so much higher within the boundary layer, this profile predicts a longer required dwell time than Hufnagel-Valley 5/7. For the 50<sup>th</sup> percentile relative humidity case, the HELEEOS correlated optical turbulence climatology, in general, also predicts a longer required dwell time on target.

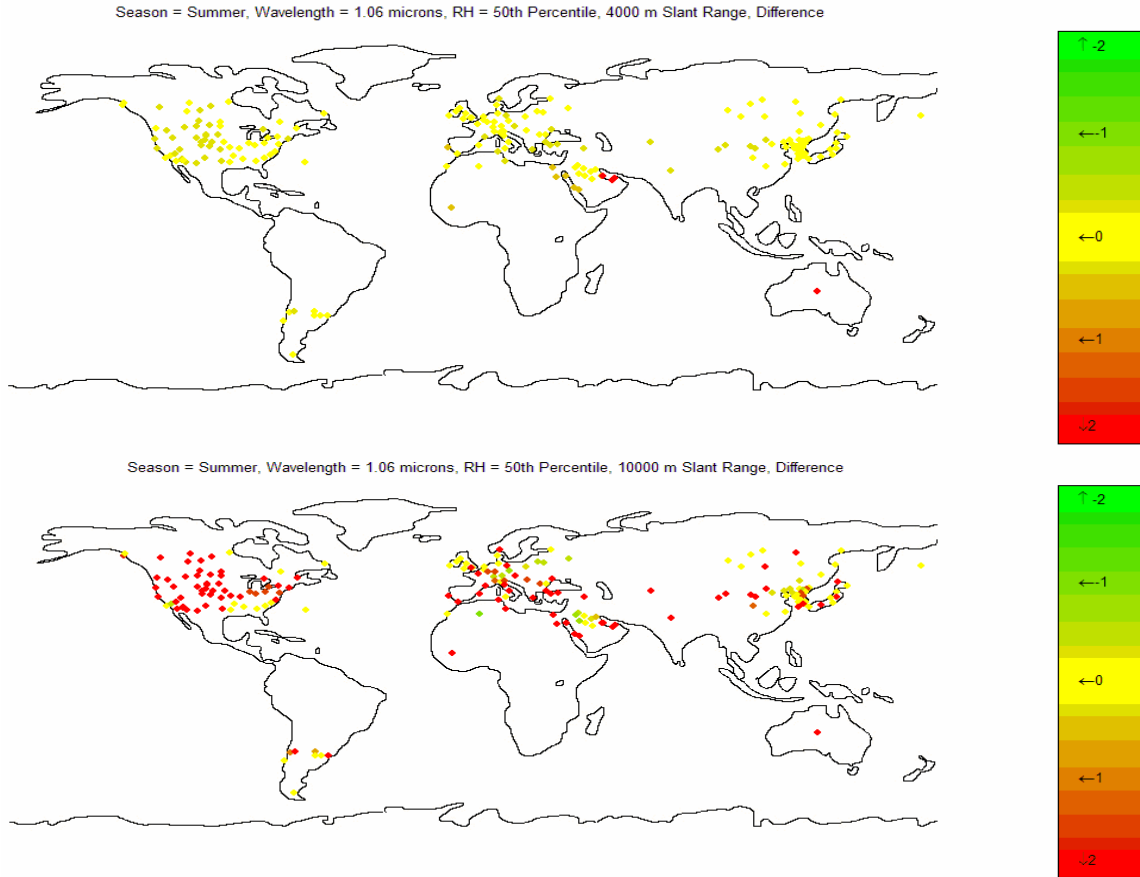


Figure 27: Dwell time difference plots between the climatological and Hufnagel-Valley profiles for a slant range of 4000 m (top) and 10,000 m (bottom).

The last case is the difference between the 95<sup>th</sup> percentile relative humidity correlated climatology and Hufnagel-Valley 5/7 profiles. There are several desert locations where the correlated climatology predicts longer dwell times and a few mid-latitude locations where Hufnagel-Valley 5/7 predicts the longer time. On the whole for this scenario, the two profiles predict similar required dwell times worldwide. This feature of predicting system performance for various meteorological conditions is unique to the HELEEOS correlated climatology. It is important to understand the effects on HEL system performance given an optical turbulence profile in order to correctly predict a scenario's outcome.

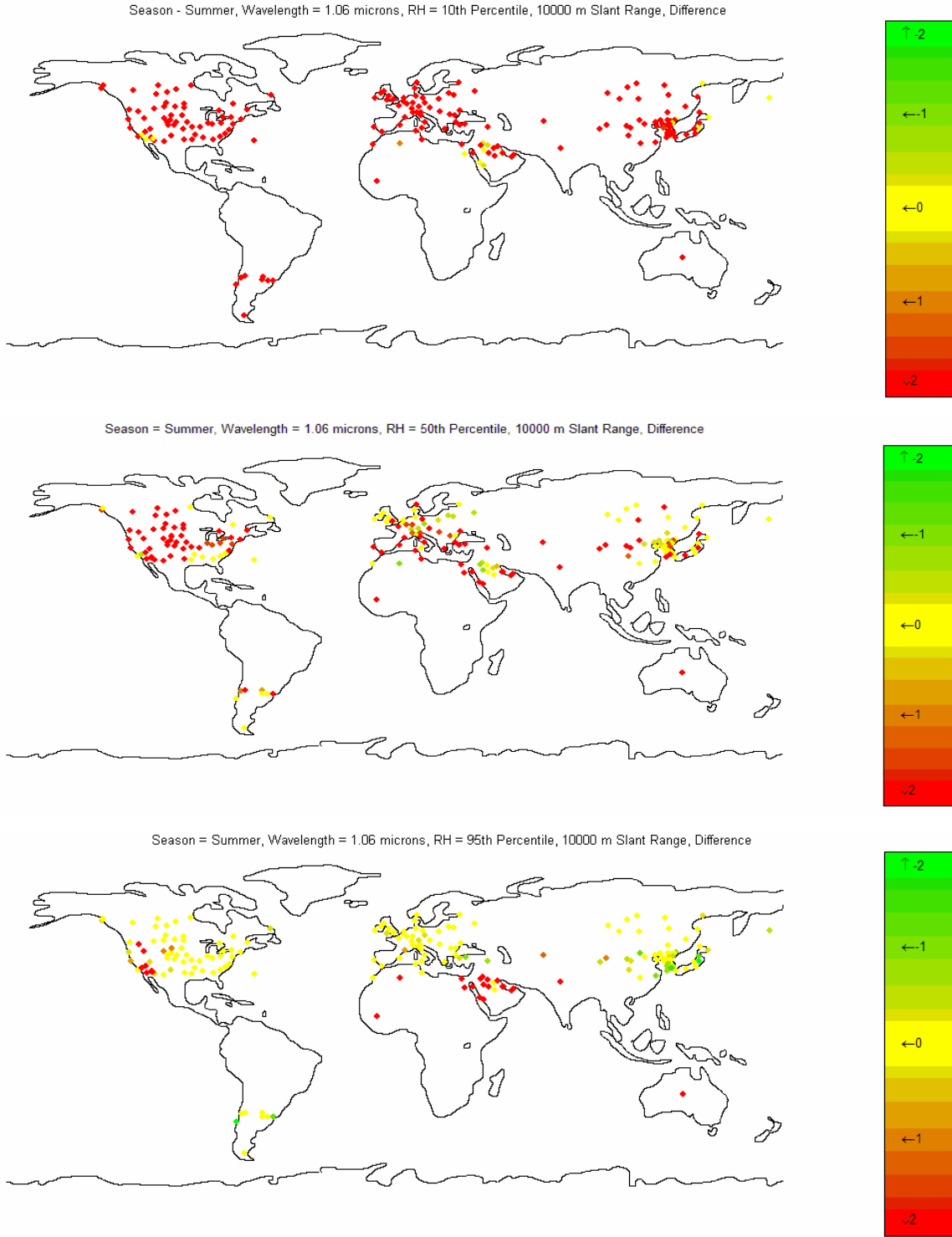


Figure 28: Worldwide required dwell time differences between Hufnagel-Valley 5/7 and the HELEEOS correlated climatological  $C_n^2$  profiles for the summer season with variations in RH, 10<sup>th</sup> percentile (top), 50<sup>th</sup> percentile (middle) and 95<sup>th</sup> percentile (bottom), a wavelength of 1.06  $\mu\text{m}$ , and a slant range of 10 km.

## V. Conclusions and Recommendations

### 5.1 Conclusions

This research confirms that there are differences between the standard and correlated climatological  $C_n^2$  profiles, which produce changes in system performance not only locally, but on a worldwide scale. The magnitude of the variation in performance also depends upon the scenario. For tactical low altitude scenarios, the required dwell time differences range from a few hundredths of a second to 42 s between the standard models and the correlated climatology and three or four orders of magnitude with DEEST. At high altitudes, 7620 m, the dwell time differences range from 160 s between the standard models and the correlated  $C_n^2$  climatology and three to five orders of magnitude between the DEEST and the others. For the surface layer scenario, the differences in system performance were the smallest, ranging from a few seconds amongst the standard, NSLOT, and correlated climatology, and two to three orders of magnitude between them and the DEEST profile. It is important to properly characterize optical turbulence vertical profiles because these differences in profiles are significant with regard to HEL system performance.

As the comparison between the statistically enhanced climatological model and the thermosonde data showed, the randomization technique used in the statistical model's programming did not mimic the irregularities in the physical data, except for within the boundary layer. Although the statistical model's randomization technique does not completely mimic physical trends in optical turbulence, the enhanced profiles appear to be more realistic than a smooth generalized profile. Therefore, using a randomized

profile in an engagement scenario might yield a more realistic system performance prediction than a smooth profile.

Unlike the statistical comparison, the purpose of the numerical comparisons was to observe similar magnitudes and shapes in the  $C_n^2$  profiles. The specific comparisons to the DEEST model show that the correlated climatological and standard profiles, and the source thermosonde data, are several orders of magnitude less than the DEEST profiles obtained for this study. Figure 23 shows a slightly better DEEST representation of the thermosonde data, but it still confirms that, in general, DEEST produces optical turbulence vertical profiles that are two to three orders of magnitude greater than physically measured optical turbulence profiles. Regarding HEL engagement scenarios, DEEST optical turbulence estimations produce required dwell times that are three to four orders of magnitude greater than the times produced using the other models. Therefore, DEEST profiles may provide unrealistic predictions in HEL system performance.

Conversely, the NSLOT comparisons show that even though the model comparison scenarios used different but adjacent surfaces, the profile values are still within the same order of magnitude and the required dwell times on target are within a 1 s to 3.5 s of one another. These results are taken to confirm that the  $C_n^2$  modeling techniques of NSLOT and HELEEOS are valid characterizations for the inputted climatological conditions.

Although there are many different types of comparisons made throughout this paper, there are two important confirmations from this research. First, this study demonstrates that the modified optical turbulence climatology used by HELEEOS can effectively correlate optical turbulence values to other meteorological parameters, especially relative humidity within the boundary layer. Thus, HELEEOS can produce

$C_n^2$  profiles in a realistic manner. Since the data were sorted by climatological parameters, they are also applicable to other areas of the globe with similar climatology. The HELEEOS  $C_n^2$  profiles also have the flexibility to predict optical turbulence values for extreme percentile cases. This is important because  $C_n^2$  values do not remain the same despite similarities in weather conditions. The other significant conclusion is that one can use HELEEOS to run all the different optical turbulence models and produce all of the comparisons herein. Having all of the various standard models programmed into one larger encompassing program makes the data generation much faster and considerably easier. HELEEOS not only has these models implemented into its programming, but it also uses other algorithms to simulate laser weapon system performance. Therefore, even the effects due to the differences in optical turbulence models can be calculated using HELEEOS and the operational implications of those differences can be quantified. The understanding and knowledge of the magnitude of these changes is important because these differences in system performance could have significant operational implications.

## **5.2 Recommendations**

As a result of this study's analysis, there are several suggestions to upgrade HELEEOS' modeling capabilities. To assist the user, it might be beneficial to continue the study on the dwell time effects between the standard and climatological profiles. Then, the differences can be quantified, and the user would be able to anticipate the results of the system performance prediction for the desired scenario. Another suggestion would be to implement the statistical model into HELEEOS, and do a study concerning the varying system effects caused by the differences in randomized profiles vs. smooth

trends. This would help to determine and quantify the benefits of using a more realistic optical turbulence profile. A final implementation into HELEEOS would be the capability to read in standard AFWA meteorological data files (MM5 and GRIB), and use the correlated  $C_n^2$  climatology method to produce realistic optical turbulence vertical profiles based on the most recent weather predictions. This would enable HELEEOS to incorporate real-time weather data and forecasts for operational tactical-level engagements.

An additional study would be to genuinely extend the climatological profile down to the surface. Currently, the surface  $C_n^2$  data are limited in number, so HELEEOS should implement a true surface layer model to characterize optical turbulence at these low altitudes. This would supplement the modeling of the boundary layer, and HELEEOS would have the capabilities to realistically produce better optical turbulence values at lower altitudes. One could do this by using valid numerical models such as NSLOT or produce a  $C_n^2$  database based on surface layer optical turbulence effects on a propagating laser beam. Another quantifiable comparison can be made between the HELEEOS climatological profile's optical turbulence modeling capabilities and other studies, where surface layer optical turbulence data were physically collected. These comparisons with measured climatological  $C_n^2$  values would provide a validation of simulated surface values produced by HELEEOS. An additional task, that would expand HELEEOS' modified optical turbulence climatologies, would be to analyze thermosonde data collected over tropical regions. Then, HELEEOS could truly characterize  $C_n^2$  worldwide. The last task should be to model optical turbulence horizontally. Currently, for a given altitude,  $C_n^2$  is a constant along a horizontal path. However, this is not a

completely valid assumption, and for the most accurate system performance prediction, such heterogeneity should be modeled as well.

## Appendix

The following three figures contain the profiles of each remaining ABL campaign site not analyzed in Chapter 4. These figures help support the analysis in section 4.2.

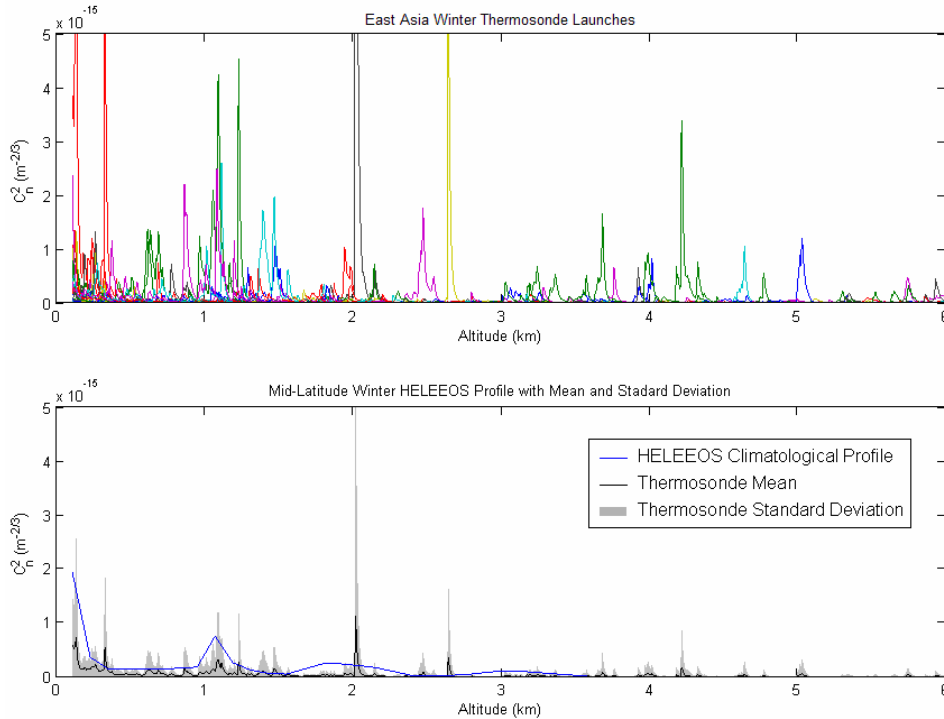


Figure 29: Comparison of the East Asia winter thermosonde data to the corresponding HELEEOS correlated optical turbulence climatology. The top plot is each raw thermosonde profile, and the bottom contains the comparison between the HELEEOS correlated  $C_n^2$  climatology and the thermosonde data mean and standard deviation. The boundary layer height for this scenario is 500 m.

The bottom plot shows the mean and standard deviation from all of the campaign launches for this East Asia location and the corresponding HELEEOS correlated optical turbulence climatology for a similar EXPERT winter location and night time boundary layer height. As one can see, the HELEEOS correlated climatology generally falls within one standard deviation of the mean from the thermosonde data. Therefore, this method of

optical turbulence characterization accurately represents physical data for this location, season, and time of day.

The next figure illustrates the comparison between the HELEEOS correlated  $C_n^2$  climatology for a coastal desert winter and the corresponding ABL campaign thermosonde profiles. Overall, the HELEEOS climatology falls within the mean and standard deviation of the thermosonde data. The only exception is the peak in  $C_n^2$  just above the boundary layer. It would fall within the standard deviation if the peak was shifted down a few meters, and this feature is most likely a result from the low resolution binning process.

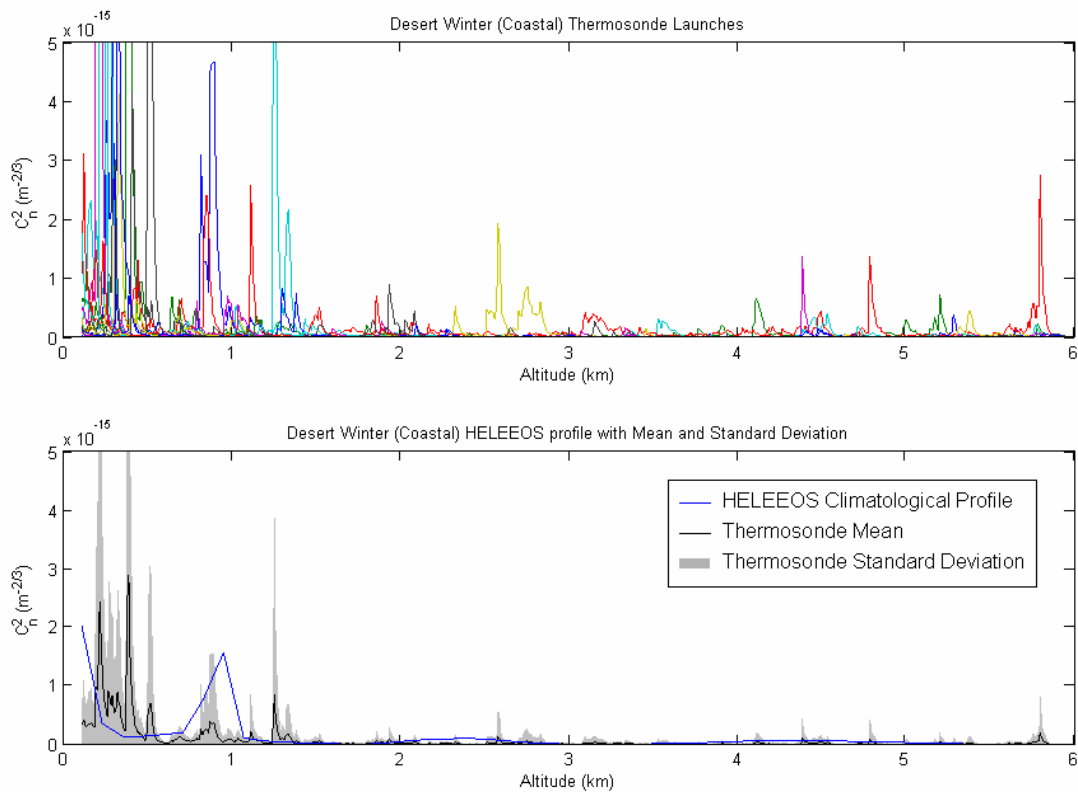


Figure 30: Comparison of the desert coastal winter thermosonde data to the corresponding HELEEOS correlated optical turbulence climatology. The top plot is each raw thermosonde profile, and the bottom contains the comparison between the HELEEOS correlated  $C_n^2$  climatology and the thermosonde data mean and standard deviation. The boundary layer height for this profile is 500 m.

This final figure shows the ABL campaign profiles for an inland desert winter site and its corresponding HELEEOS correlated  $C_n^2$  climatology. Within the first 500 meters of the boundary layer, the HELEEOS profile is approximately three times as large in magnitude of the standard deviation. However, the first 120 m of the boundary layer are not shown, but were analyzed with the rest of the boundary layer data to create this profile. The initial surface  $C_n^2$  mode values are large enough to produce this magnitude difference. The remain part of the HELEEOS profile falls within the standard deviation of the thermosonde data, and particularly captures the two large peaks in  $C_n^2$  at 3 and 4 km. Again, it is important to note for all of these figures, that HELEEOS is not reproducing the campaign launch conditions, but rather is given similar input parameters to estimate an optical turbulence profile for the given conditions.

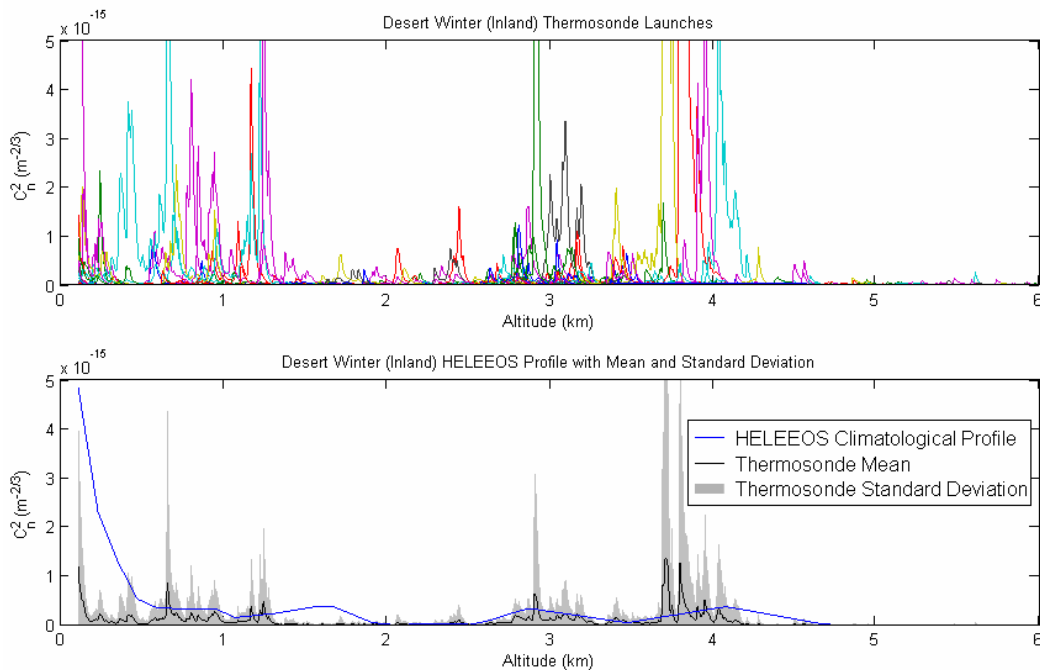


Figure 31: Comparison of the desert inland winter thermosonde data to the corresponding HELEEOS correlated optical turbulence climatology. The top plot is each raw thermosonde profile, and the bottom contains the comparison between the HELEEOS correlated  $C_n^2$  climatology and the thermosonde data mean and standard deviation. The boundary layer height for this scenario is 500 m.

The following six plots show the comparison between climatological distributions in the free atmosphere and ones from statistically randomized profiles for the same altitude slab as the climatological distributions. This material supports the results and analysis discussed in section 4.4.2.

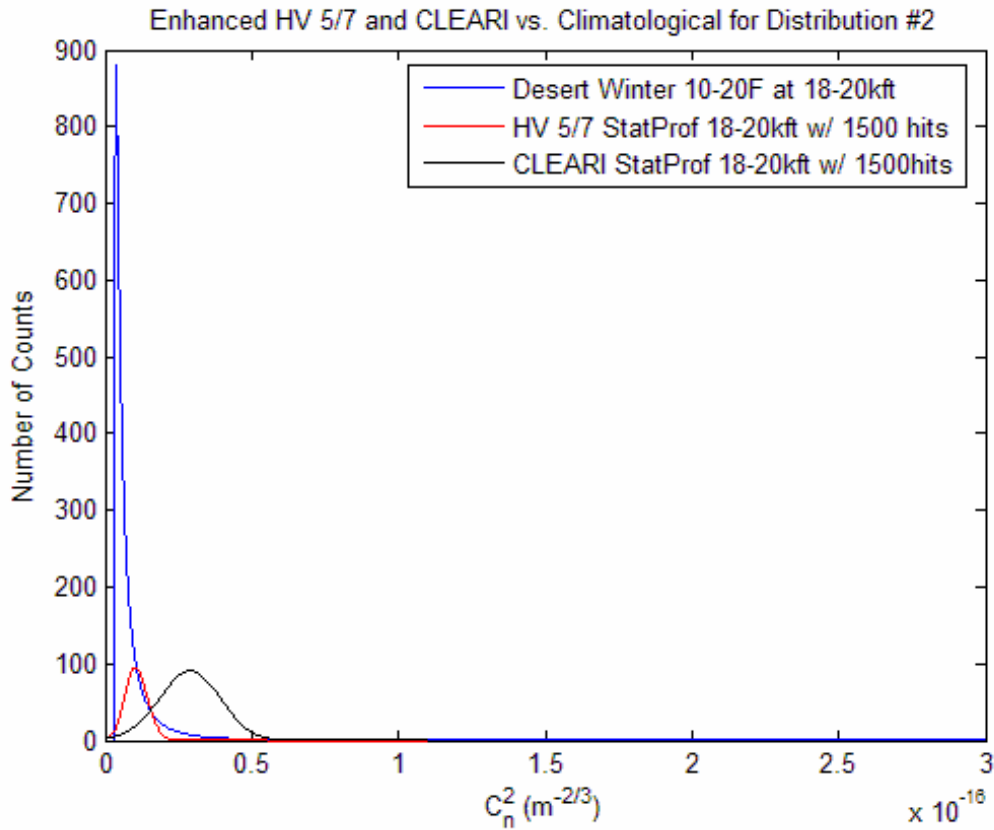


Figure 32: Enhanced Hufnagel-Valley 5/7 and CLEARI profiles with desert winter at 10-20 °F and from 18-20kft for random distribution #2.

This figure illustrates the differences between the statistical distributions between the climatological distribution and the statistical randomized distributions. As one can see, the climatological distribution is lognormal, and the mode value has a large number of counts. However, the statistically randomized distributions are Gaussian, their mode values are slightly different, and the magnitude of the number of counts is almost an order of magnitude less than the climatological distribution. This confirms that at higher

altitudes, the statistically randomized profiles do not mimic the climatological randomization of  $C_n^2$  at higher altitudes.

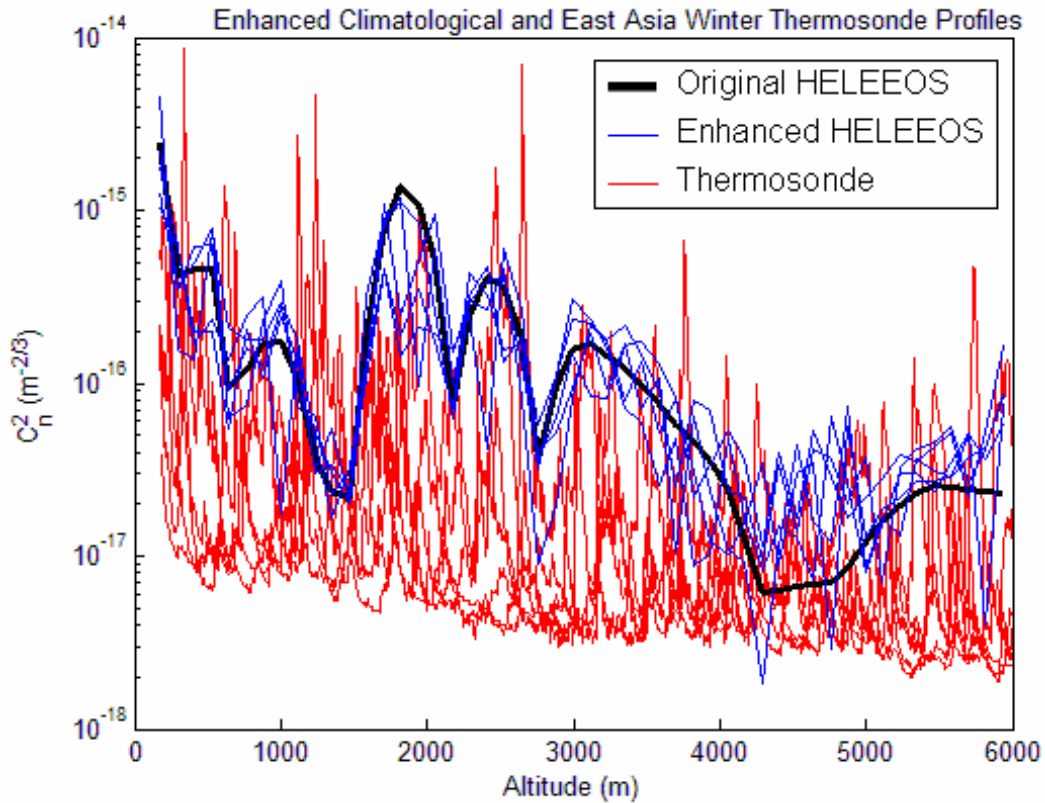


Figure 33: Enhanced Mid-latitude winter correlated  $C_n^2$  climatology with the corresponding East Asia thermosonde profiles.

This plot depicts the statistical model’s randomization technique against the climatological randomization. The blue profiles are the East Asia randomized HELEEOS correlated  $C_n^2$  climatology, and they exhibit a Gaussian distribution about the original HELEEOS correlated  $C_n^2$  climatology. The red profiles are the ABL campaign thermosonde profiles for the corresponding location, and they exhibit a log normal distribution about a line at approximately  $10^{-17} \text{ m}^{-2/3}$ .

The next comparison shows the ABL campaign for the desert summer location, the HELEEOS correlated  $C_n^2$  climatology, and five randomized correlated climatologies.

One can see the Gaussian distribution about the original HELEEOS correlate  $C_n^2$  climatology, and the lognormal distribution in the thermosonde data.

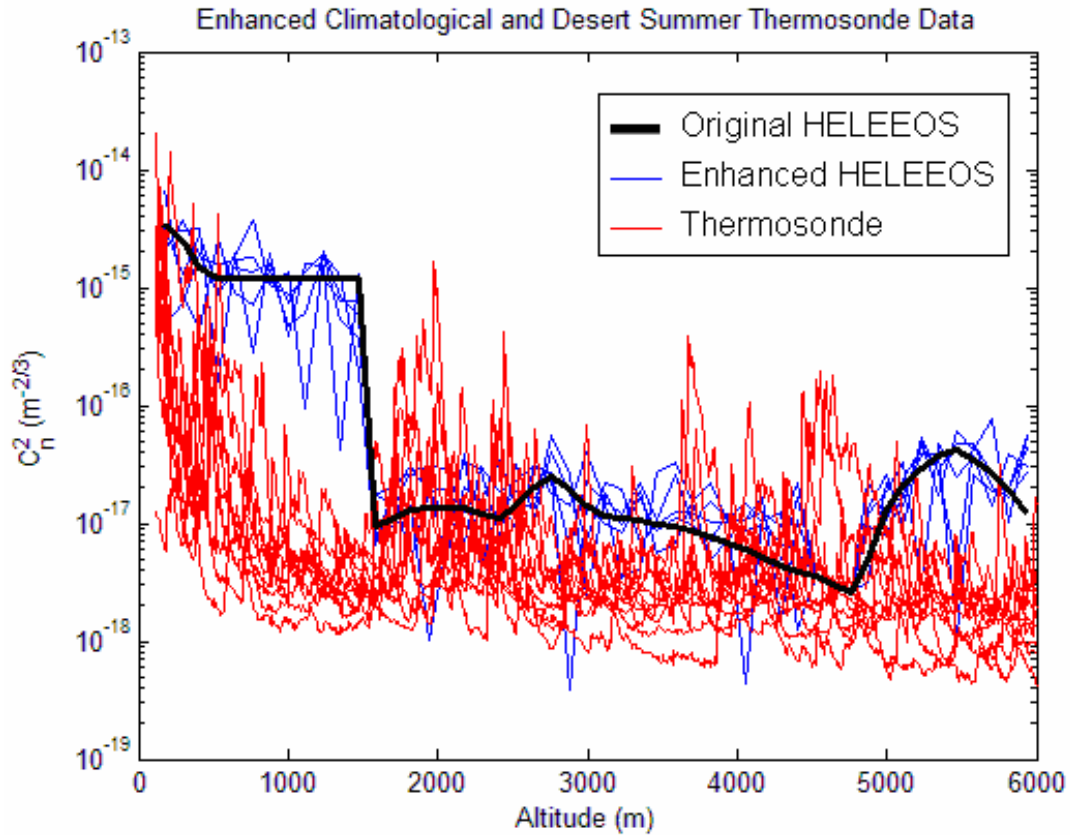


Figure 34: Enhanced Desert summer correlated  $C_n^2$  climatology and the corresponding ABL campaign thermosonde profiles.

Figure 35 illustrates the differences between the inland desert winter ABL campaign thermosonde optical turbulence profiles, the corresponding HELEEOS correlated  $C_n^2$  climatology, and five enhanced correlated  $C_n^2$  climatologies. One can see the Gaussian distribution of the statistical model's randomization technique against the lognormal distribution of the thermosonde data.

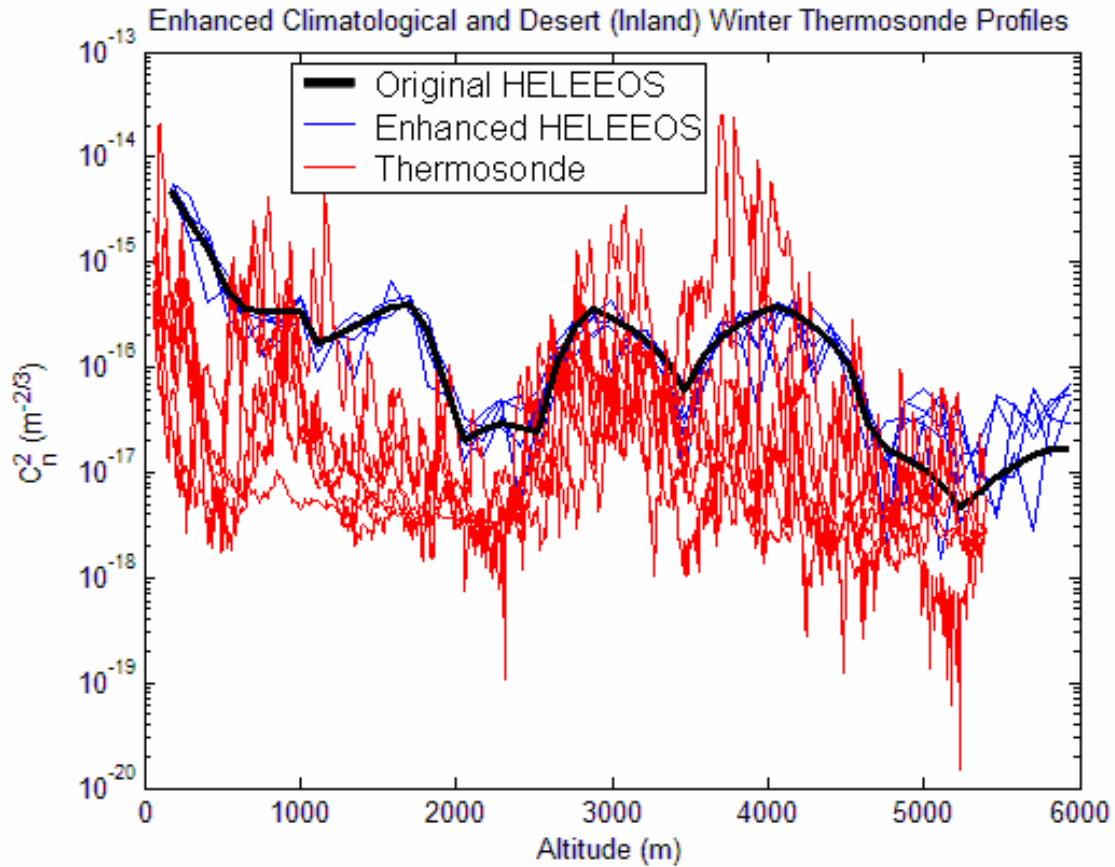


Figure 35: Enhanced desert inland winter correlated  $C_n^2$  climatology with the corresponding ABL campaign thermosonde profiles.

Figure 36 shows the final comparison between the statistically randomized HELEEOS correlated optical turbulence climatological profiles and the corresponding coastal desert winter thermosonde profiles collected for the ABL campaign. Again, this figure illustrates the differences between the Gaussian distribution of the enhanced correlated  $C_n^2$  climatology produced by the statistical model, ATMtools, and the lognormal distribution of the thermosonde data.

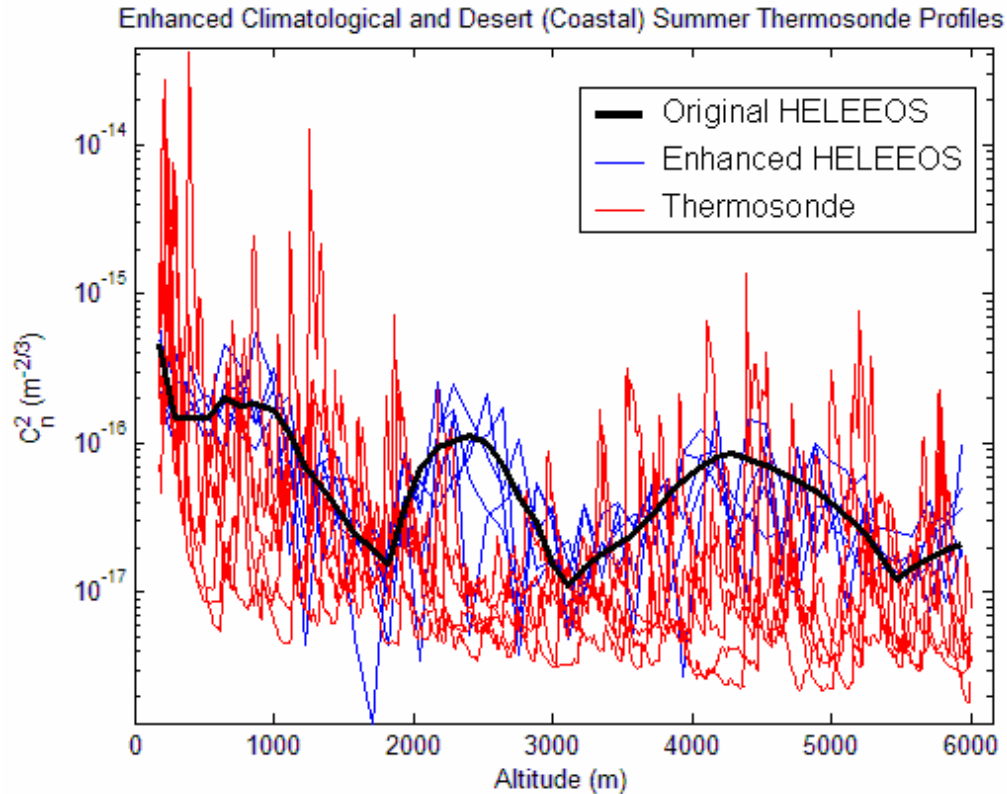


Figure 36: Enhanced desert coastal winter correlated  $C_n^2$  climatology with the corresponding ABL campaign thermosonde profiles.

The final comparison illustrates the differences between the East Asia winter thermosonde optical turbulence vertical profiles, five enhanced Hufnagel-Valley 5/7 profiles, and the original HELEEOS correlated  $C_n^2$  climatology and Hufnagel-Valley 5/7 profile. This figure shows the difference between the thermosonde optical turbulence profiles and another randomized profile, Hufnagel-Valley 5/7. The Gaussian distribution of the statistically randomized profile and how different it is from the climatological randomization is easily seen in this figure. Again, the purpose of these six plots is to support the results of section 4.4.2. Although the  $C_n^2$  values are randomized, the statistically generated profiles do not mimic the climatological values and distributions of  $C_n^2$ .

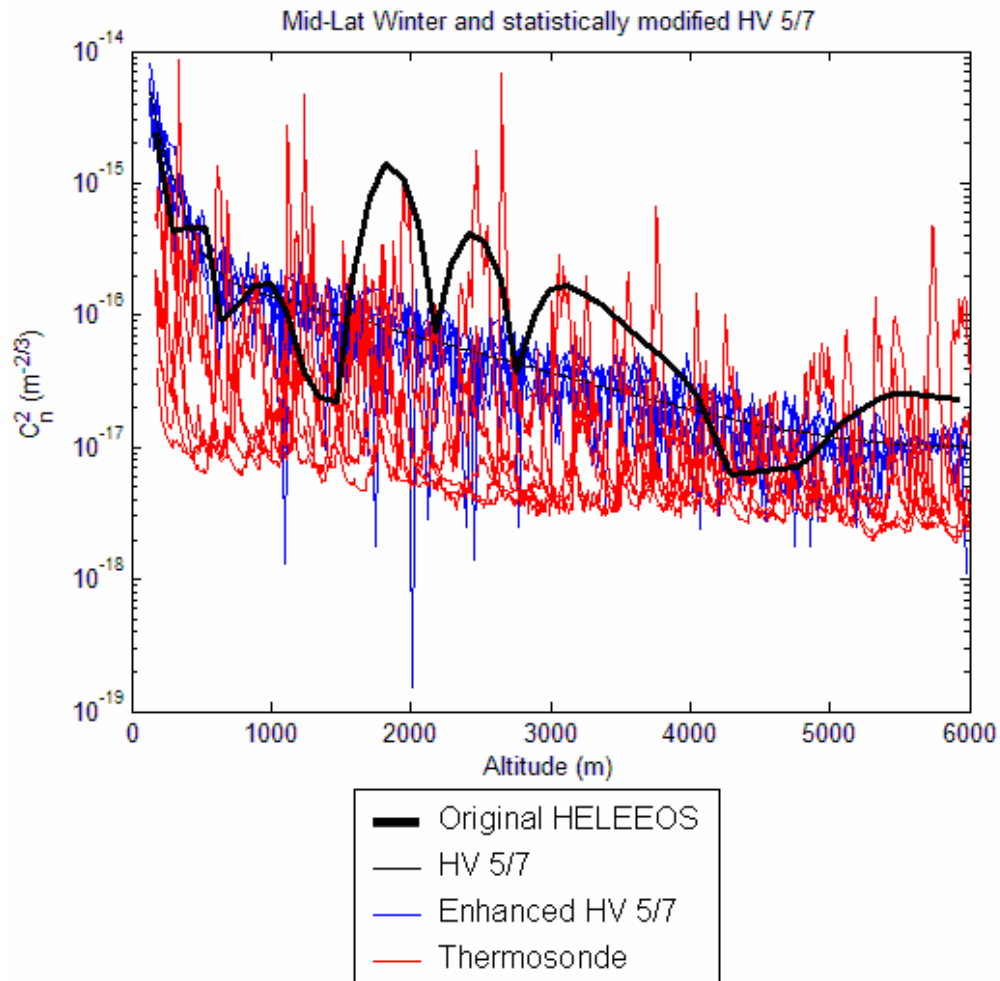


Figure 37: Enhanced Hufnagel-Valley 5/7 and East Asia winter ABL campaign thermosonde profiles with the HELEEOS correlated  $C_n^2$  climatology.

The final sets of figures are the worldwide plots illustrating the differences between the required dwell times between the Hufnagel-Valley 5/7 profile and the HELEEOS correlated  $C_n^2$  climatology. These plots support the results discussed in section 4.6, where it addresses the changes in HEL system performance using differing optical turbulence profiles.

Figure 38 and Figure 39 illustrate the worldwide variation in system performance prediction between Hufnagel-Valley 5/7 and the summer correlated  $C_n^2$  climatology.

Both scenarios have a slant range of only 4000 m, and therefore, the differences between the two profiles are not as apparent. Except for a few desert locations, the two profiles predict approximately the same required dwell times.

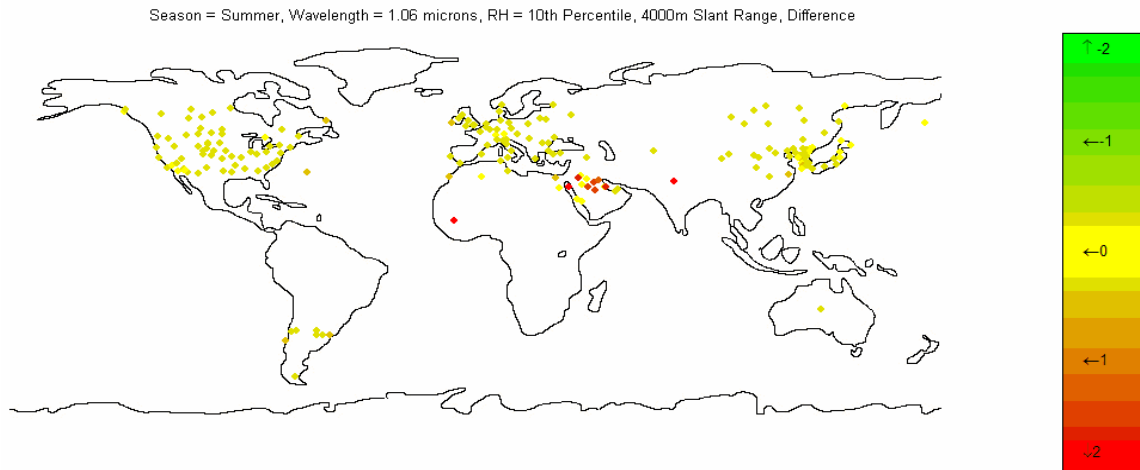


Figure 38: The difference in dwell time between Hufnagel-Valley 5/7 and the climatological profiles for the 10<sup>th</sup> percentile relative humidity and a 4000 m slant range.

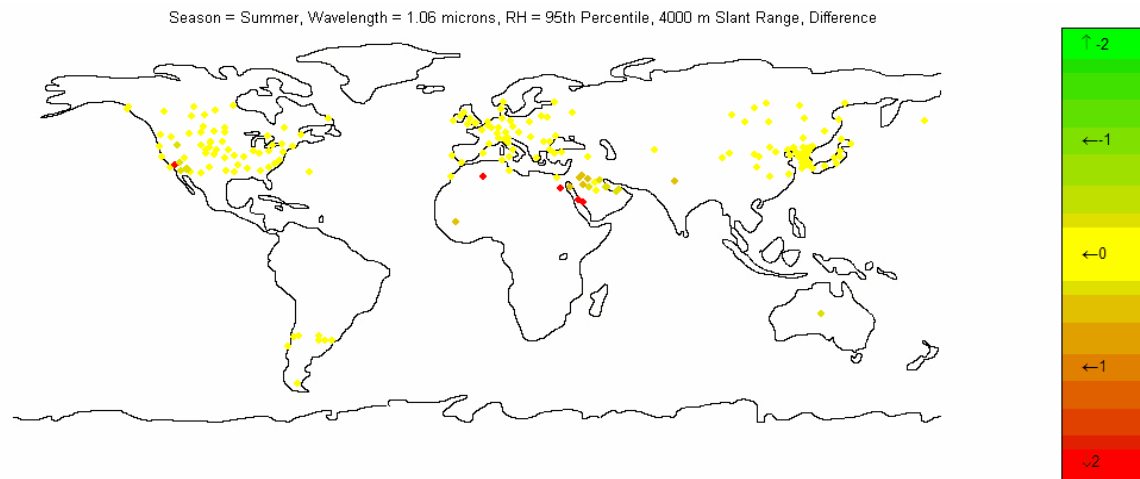


Figure 39: The difference in dwell time between Hufnagel-Valley 5/7 and the climatological profiles for the 95<sup>th</sup> percentile relative humidity and a 4000 m slant range.

The next figure, Figure 40, shows the difference in required dwell times between Hufnagel-Valley 5/7 and the winter 10<sup>th</sup> percentile RH correlated  $C_n^2$  climatology.

Despite the obvious differences in required dwell times in Northern Europe, the general worldwide difference between the two profiles is not as apparent because of the 4000 m slant range.

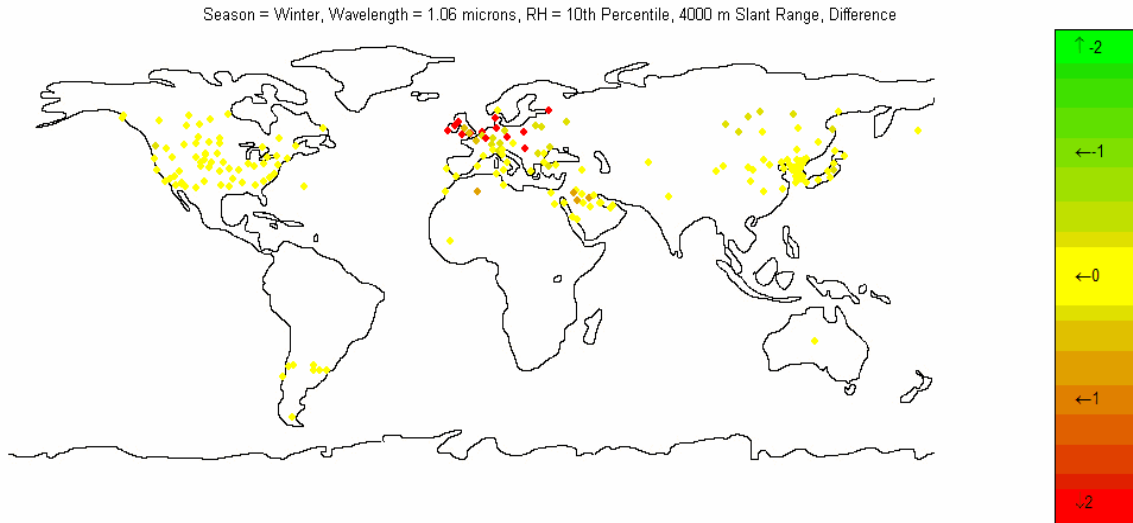


Figure 40: The difference in dwell time between Hufnagel-Valley 5/7 and the climatological profiles for the 10<sup>th</sup> percentile relative humidity and a 4000 m slant range.

Figure 41 illustrates the differences in required dwell times between Hufnagel-Valley 5/7 and the winter 50<sup>th</sup> percentile RH correlated  $C_n^2$  climatologies for slant ranges of 4000 and 10,000 m. The impact slant range has on the difference in required dwell time on target caused by the two profiles is clear in this figure.

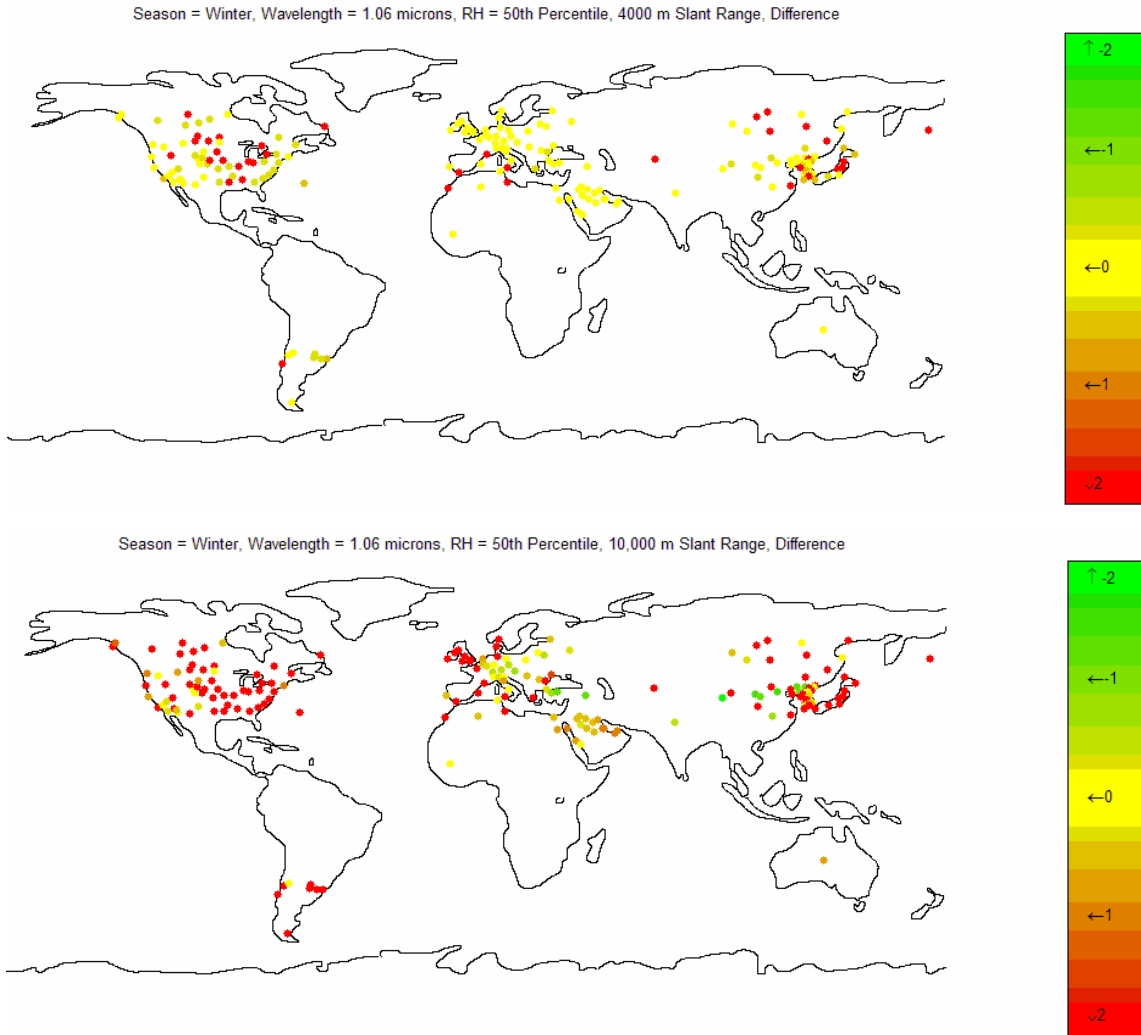


Figure 41: The difference in dwell time between Hufnagel-Valley 5/7 and the correlated  $C_n^2$  climatologies for the 50<sup>th</sup> percentile RH and a slant range of 4000 m (top) and 10,000 m (bottom)

The final figure in this set, Figure 42, shows the variation in required dwell times between Hufnagel-Valley 5/7 and the winter 95<sup>th</sup> percentile RH HELEEOS correlated  $C_n^2$  climatology for slant ranges of 4000 and 10,000 m. In the 4000 m slant range case, the required dwell times for both profiles are almost the same worldwide. However, the differences between the two profiles are amplified, and are clearly illustrated in the bottom plot of the figure.

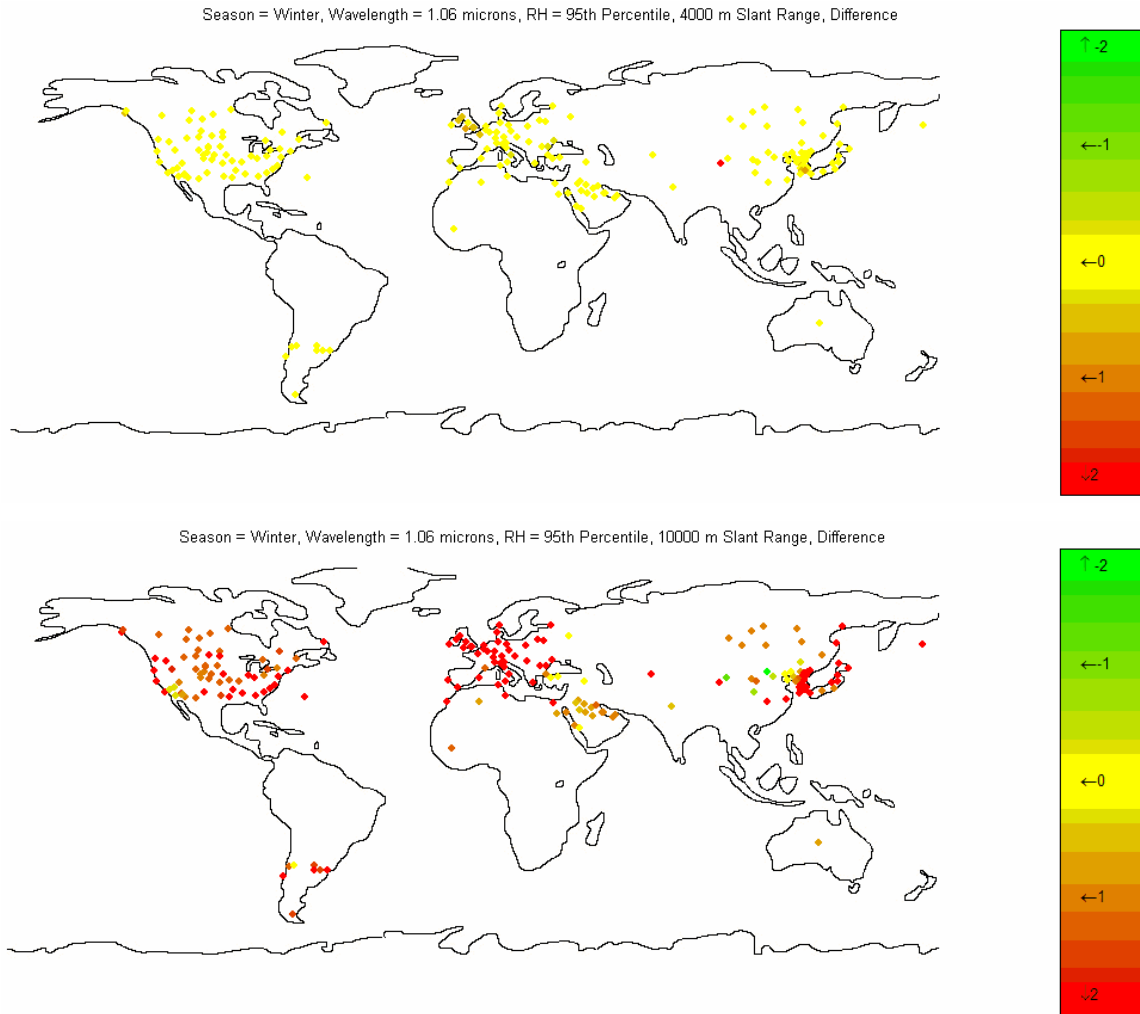


Figure 42: The difference in dwell time between Hufnagel-Valley 5/7 and the correlated  $C_n^2$  climatologies for the 95<sup>th</sup> percentile relative humidity for a slant range of 4000 m (top) and 10,000 m (bottom)

The following four tables are the non-expanded coefficient tables that HELEEOS accesses to produce optical turbulence profiles for its correlated  $C_n^2$  climatologies. These tables illustrate the lack of data that causes the affects seen in sections 4.2 and 4.3.

Table 8: Boundary layer coefficients for the East Asia Summer campaign.

	0-5%	60-65%	65-70%	70-75%	75-80%	80-85%	85-90%	90-95%	95-100%
<b>a</b>	<b>0-200 ft</b>	~~				1.453	0.9919	0.8457	0.5512
<b>b</b>		~~			32.09	13.32		19.66	62.89
<b>c</b>		~~			1.50E-15	2.54E-15		1.01E-15	1.59E-15
<b>d</b>		~~			1.09E-15	1.89E-15		4.55E-16	2.11E-16
<b>e</b>		~~			1.633	1.133		14.55	13.53
<b>a</b>	<b>200-1200 kft.</b>	~~	0.25	0.559	-0.1389	0.5619	0.3599	1.121	1.220
<b>b</b>		~~	20.11	103.4	77.36	61.8	116.1	47.4	116.8
<b>c</b>		~~	9.01E-16	4.72E-16	1.55E-16	1.87E-16	2.85E-16	1.50E-16	1.04E-16
<b>d</b>		~~	5.81E-16	5.63E-16	1.72E-16	4.19E-17	3.56E-16	7.72E-17	1.52E-16
<b>e</b>		~~	0.5979	1.492	3.121	7.175	1.561	6.079	1.994

Table 9: Upper air coefficients from 1-5 kft for the East Asia Summer campaign

		-70 - -60°F	30 - 40°F	40 - 50°F	50 - 60°F	60 - 70°F	70 - 80°F	80 - 90°F	90 - 100°F
<b>a</b>	<b>1-2 kft</b>	~~				0.6629	0.3225		
<b>b</b>		~~				14.498	1249.8		
<b>c</b>		~~				1.37E-16	1.73E-16		
<b>d</b>		~~				1.03E-17	1.16E-17		
<b>e</b>		~~				3.86	9.099		
<b>a</b>	<b>2-3 kft</b>	~~				0.7318	0.6		
<b>b</b>		~~				385.2	536.3		
<b>c</b>		~~				1.95E-16	2.79E-16		
<b>d</b>		~~				9.28E-17	2.03E-16		
<b>e</b>		~~				1.847	1.114		
<b>a</b>	<b>3-4 kft</b>	~~				0.2222	0.5		
<b>b</b>		~~				914.4	78.51		
<b>c</b>		~~				1.08E-15	9.82E-17		
<b>d</b>		~~				7.24E-16	6.94E-17		
<b>e</b>		~~				1.048	0.9962		
<b>a</b>	<b>4-5 kft</b>	~~			0.25	-1.487			
<b>b</b>		~~			44.03	988.1			
<b>c</b>		~~			1.33E-16	4.63E-17			
<b>d</b>		~~			9.99E-17	2.70E-18			
<b>e</b>		~~			0.973	17.97			

Table 10: Upper Air coefficients from 5-10kft for the East Asia Summer campaign

		-70 - -60°F	30 - 40°F	40 - 50°F	50 - 60°F	60 - 70°F	70 - 80°F	80 - 90°F	90 - 100°F
a	5-6 kft				-0.1397	0.6597			
b					220.3	859.6			
c					3.22E-17	1.08E-16			
d					5.48E-18	1.03E-16			
e					7.596	1.504			
a	6-7 kft				0.2342	0.9022			
b					570	345.5			
c					2.67E-16	2.05E-17			
d					3.13E-17	5.52E-18			
e					5.007	6.055			
a	7-8 kft				0.5556				
b					918.6				
c					1.39E-16				
d					1.14E-16				
e					1.008				
a	8-9 kft			-9.35	0.1737				
b				45.39	699				
c				5.35E-18	1.69E-17				
d				2.27E-17	4.35E-15				
e				7.145	7.261				
a	9-10 kft			0.9876	0.1492				
b				220.1	709.2				
c				3.62E-17	3.97E-17				
d				2.77E-17	3.27E-18				
e				2.072	6.573				

Table 11 : Upper air coefficients from 10-30 kft, and the temperatures are in °F for the East Asia Summer campaign.

		-70 - -60°	~~	-30 - -20°	-20 - -10°	-10 - 0°	0 - 10°	10 - 20°	20 - 30°	30 - 40°	40 - 50°	50 - 60°
<b>a</b>	<b>10-12 kft</b>		~~								0.2305	-1.116
<b>b</b>			~~								1649.4	465.0
<b>c</b>			~~								1.30E-16	6.74E-18
<b>d</b>			~~								9.71E-18	1.24E-18
<b>e</b>			~~								6.287	9.106
<b>a</b>	<b>12-14 kft</b>		~~							-2.411	0.0038	
<b>b</b>			~~							321.9	1497.2	
<b>c</b>			~~							4.36E-18	2.79E-17	
<b>d</b>			~~							3.81E-19	3.47E-18	
<b>e</b>			~~							29.84	7.268	
<b>a</b>	<b>14-16 kft</b>		~~						1.185	1.766	1.065	
<b>b</b>			~~						75.97	1402.0	310.3	
<b>c</b>			~~						1.39E-17	4.11E-18	1.12E-17	
<b>d</b>			~~						1.74E-17	2.04E-18	7.49E-19	
<b>e</b>			~~						1.764	4.184	12.684	
<b>a</b>	<b>16-18 kft</b>		~~						0.0424	0.9504		
<b>b</b>			~~						537.8	718.3		
<b>c</b>			~~						9.31E-18	2.55E-18		
<b>d</b>			~~						9.18E-19	2.30E-18		
<b>e</b>			~~						12.02	2.618		
<b>a</b>	<b>18-20 kft</b>		~~					0.7186	2.402	4.067		
<b>b</b>			~~					218.0	726.8	49.19		
<b>c</b>			~~					1.29E-17	2.21E-18	2.95E-18		
<b>d</b>			~~					4.11E-18	3.61E-18	2.17E-18		
<b>e</b>			~~					3.494	1.918	0.8773		
<b>a</b>	<b>20-25 kft</b>		~~			0.9148	0.1872	-0.4097	0.2245			
<b>b</b>			~~			197.1	1239.1	2302.4	801.4			
<b>c</b>			~~			2.02E-17	6.80E-18	1.44E-17	1.47E-17			
<b>d</b>			~~			1.27E-18	1.22E-18	8.52E-19	1.14E-18			
<b>e</b>			~~			14.44	6.966	10.56	6.60E+00			
<b>a</b>	<b>25-30 kft</b>		~~	1.276	1.604	0.5455	-2.169	1.1995				
<b>b</b>			~~	31.94	875.7	2237.5	1639.3	46.91				
<b>c</b>			~~	2.87E-18	4.33E-17	1.54E-16	3.56E-18	6.47E-18				
<b>d</b>			~~	2.57E-18	4.16E-17	1.10E-16	2.98E-19	4.15E-18				
<b>e</b>			~~	1.178	1.444	1.006	15.22	1.183				

This final table illustrates the differences in required dwell time between the various optical turbulence profiles for a desert summer location. This table is supplementary material to Table 7. For the first scenario, the standard models predict

dweltimes 4 s longer than the correlated  $C_n^2$  climatology for 50<sup>th</sup> percentile (average) RH, and the DEEST profile predicts required dweltimes that are 3 to 4 orders of magnitude greater than the others. For the second scenario, the standard models predict longer dweltimes of approximately 100 s, than the correlated  $C_n^2$  climatologies, and DEEST's required dwell time prediction is five orders of magnitude greater than the others. The surface layer scenario predicts dwell time on the order of a few seconds for NSLOT and the correlated  $C_n^2$  climatologies. The standard models predict dweltimes that are 20 seconds longer than the two previous model types, and the required dwell time using DEEST is two to three orders of magnitude greater than the others.

Table 12: A tabular summary of required dweltimes for a desert summer location using each of the standard and numerical profiles and the correlated  $C_n^2$  climatology for 3 various scenarios: Low- altitude with a 10 km slant range; High-altitude with a 90 km slant range; Surface layer with a 1 km slant range. All scenarios use a 50 kW solid state laser with an aperture size of .5 m.

	<b>Low-Alt. 10km Slant Range</b>	<b>High-Alt. 90km Slant Range</b>	<b>Surface Layer Platform Alt. 20 m and Target Alt. 5m with 5 km Slant Range</b>
<b>HV 5/7</b>	16.6828	579.6422	25.0958
<b>CLEARI</b>	17.4248	587.9571	25.0958
<b>HELEEOS 10%</b>	8.4877	471.5085	4.3749
<b>50%</b>	11.134	473.1038	2.014
<b>95%</b>	35.2924	474.7046	5.1225
<b>DEEST (over land)</b>	3.36E+05	1.10E+08	5.29E+04
<b>NSLOT</b>			1.3115

## Bibliography

- Adair, S.C., G.T. Fairley, G.P. Seeley and G.Y. Jumper. "Directed Energy Engagement Scenarios with Low Altitude Optical Turbulence Models." Presented at the Directed Energy Professional Society (DEPS) Conference March 17, 2005, Tampa, FL (2005)
- Alliant Techsystems Mission Research. *ATMtools: A Toolbox for Atmospheric Propagation Modeling. Users Guide Version 2.4.* Mission Research Document ATK/MR-DN-R-05-04. 27 September 2005
- Bartell, R.J., S.T. Fiorino, M. Whitely, and E Magee, "HELEEOS/SHARE Scaling Law Models Short Course", 3rd Annual Directed Energy Professional Society Modeling and Simulation Conference, Tampa, FL, March 2005.
- Beland, R.R. "Propagation through Atmospheric Optical Turbulence," *The Infrared and Electro-Optical Systems Handbook, Vol. 2.* Ed. Frederick G. Smith. Ann Arbor, MI: Infrared Information Analysis Center. 1993
- Boeing. "Airborne Laser Overview." An article. n. pag.  
<http://www.boeing.com/defense-space/military/abl/overview.html>. 25 August 2005
- Buften, J.L. *A Radiosonde Thermal Sensor Technique for Measurement of Atmospheric Turbulence.* NASA TN D-7867, pp. 41. 1975
- Bussey A.J., J.R. Roadcap, R.R. Beland, and G.Y. Jumper. *Master data base for optical turbulence research in support of airborne laser.* Air Force Research Laboratory technical report, AFRL-VS-TR-2000-1545. 2000
- Fiorino, S.T., D.L. Parks. "Regional and worldwide atmospheric profiles for MERIT." *Institute of Environmental Sciences 1995 proceedings, 41<sup>st</sup> Annual Meeting.* 1995
- Fiorino, S.T. Class lecture notes, METG 611, Atmospheric and Space Environmental Effects on Electromagnetic Propagation, School of Engineering and Management, Air Force Institute of Technology, Wright-Patterson AFB OH, Spring Quarter 2005, 2005
- Fiorino, S.T. Thesis Advisor, Air Force Institute of Technology, Wright-Patterson AFB OH. Personal Correspondance. 8 December 2005.
- Fiorino S.T., R.J. Bartell, G.P. Perram, D.W. Bunch, L.E. Gravley, C.A. Rice, Z.P. Manning and M.J. Krizo. "The HELEEOS Atmospheric Effects Package: A Probabilistic Method for Evaluating Uncertainty in Low-Altitude High Energy Laser Effectiveness." Air Force Institute of Technology, Wright-Patterson AFB OH. 2006

- Frederickson, P.A., K.L. Davidson, C.R. Zeisse, and C.S. Bendall. *Estimates of the Refractive Index Structure Parameter ( $C_n^2$ ) over the Ocean Using Bulk Methods*. J. Appl. Meteorol. Vol. 39, pp. 1770. 2000
- GlobalSecurity.org. "Advanced Tactical Laser." An article. n. pag. <http://www.globalsecurity.org/military/systems/aircraft/systems/atl.htm>. 25 August 2005
- Good, R.E., R.R. Beland, E.A. Murphy, J.H. Brown and E.M. Dewan. "Atmospheric Models of Optical Turbulence," *SPIE* Vol. 928, pp. 165-186 (1988)
- Gravley, L.E. Graduate Student at the Air Force Institute of Technology. "My Summer Internship Experience." Presented at the Directed Energy Professional Society (DEPS) Conference, Rockville, MD. 21 October 2004
- Hammel, S., D. Tsintikidis, D. Merritt, J. Fontana. "Atmospheric Characterization for High Energy Laser Beam Propagation in the Maritime Environment." Presented at the Directed Energy Professional Society (DEPS) Conference, Lihue, HI. November 2005
- Hufnagel, R.E. "Propagation Through Atmospheric Turbulence," *The Infrared Handbook*. Eds. William L. Wolfe and George J. Zissis. Ann Arbor, MI: Infrared Information Analysis Center. 1985
- Jumper, G.Y., H.M. Polchlopek, R.R. Beland, E.A. Murphy, P. Tracy, K. Robinson. "Balloon-Borne Measurements of Atmospheric Temperature Fluctuations," *AIAA* 1997-2353, 8pp. 1997
- Jumper, G.Y., J.R. Roadcap, S.C. Adair, G.P. Seeley, and G.T. Fairley. "Atmospheric Considerations in Engagement-Level Simulations of Tactical High-Energy Laser Systems." *Journal of Directed Energy*, Vol. 1 No. 3, pp. 183-201. 2005
- Kaimal, J.C., J.C. Wyngaard, D.A. Haugen, O.R. Cote, and Y. Izumi. *J. Atmos. Sci.* Vol. 33, pp. 2152. 1976
- Koepke, P., M. Hess, I. Schult, and E.P. Shettle. "Global Aerosol Data Set." Max Planck Institute Meteorologie Hamburg Report No. 243, 44 pp. 1997
- Komolgorov, A.N. *Dissipation of Energy in Locally Isotropic Turbulence*. Doklady Akad, Nauk SSSR, 32. 1941
- Magee, Eric P. PhD, MZA Associates Corporation, Dayton OH. Personal Correspondence. 19 December 2005.

- Obukhov, A.M. *On the Distribution of Energy in the Spectrum of Turbulent Flow.*  
Doklady Akad, Nauk SSSR, 32, 19 pp. 1941
- Roadcap J.R., P.J. McNicholl, and R.R. Beland. “Analysis of thermosonde data for high energy laser tactical applications.” Presented at the Battlespace Atmospheric and Cloud Impacts on Military Operations (BACIMO) 2003, NRL Monterey, CA. 2003
- Squires M.F., B.A. Bietler, S.T. Fiorino, D.L. Parks, F.W. youkhana, and H.D. Smith. “A method for creating regional and worldwide datasets of extreme and average values.” *Institute of Environmental Sciences 1995 Proceedings, 41<sup>st</sup> Annual Meeting.* 1995.
- Tunick A. “CN2 model to calculate the micrometeorological influences on the refractive index structure parameter,” *Environmental Modelling and Software*, Vol. 18, pp. 165-171, 2003. 2003
- White, K.O., D.M. Garvey, W.A. Peterson, F.D. Eaton. “Atmospheric Characterization at the HIDL Site CLEAR 1 Program 29 August to 28 September 1984,” *US Army Atmospheric Sciences Laboratory.* AD-B096 306, 70pp. August 1985.
- Whiteley, M.R., D.C. Washburn. “Section 2: Compensation Performance”, *Airborne Laser Advanced Concepts Testbed Dynamic Compensation Experiment (DyCE) Final Report.* May 2000.

## **Vita**

Liesebet E. Gravley graduated from Wittenberg University in 2004 with a Bachelor of Arts in Physics and German. During the summer of 2005, she was hired as a Directed Energy Professional's Society (DEPS) intern, where she did research on characterizing optical turbulence. Currently, she is a graduate student at the Air Force Institute of Technology and studying applied physics.

<b>REPORT DOCUMENTATION PAGE</b>			Form Approved OMB No. 074-0188		
The public reporting burden for this collection of information is estimated to average 1 hour per response, including the time for reviewing instructions, searching existing data sources, gathering and maintaining the data needed, and completing and reviewing the collection of information. Send comments regarding this burden estimate or any other aspect of the collection of information, including suggestions for reducing this burden to Department of Defense, Washington Headquarters Services, Directorate for Information Operations and Reports (0704-0188), 1215 Jefferson Davis Highway, Suite 1204, Arlington, VA 22202-4302. Respondents should be aware that notwithstanding any other provision of law, no person shall be subject to a penalty for failing to comply with a collection of information if it does not display a currently valid OMB control number. <b>PLEASE DO NOT RETURN YOUR FORM TO THE ABOVE ADDRESS.</b>					
<b>1. REPORT DATE (DD-MM-YYYY)</b> 15-03-2006		<b>2. REPORT TYPE</b> Master's Thesis		<b>3. DATES COVERED (From - To)</b> September 2005 - March 2006	
<b>4. TITLE AND SUBTITLE</b>  COMPARISON OF CLIMATOLOGICAL OPTICAL TURBULENCE PROFILES TO STANDARD, STATISTICAL AND NUMERICAL MODELS USING HELEEOS			<b>5a. CONTRACT NUMBER</b>		
			<b>5b. GRANT NUMBER</b>		
			<b>5c. PROGRAM ELEMENT NUMBER</b>		
<b>6. AUTHOR(S)</b>  Gravley, Liesebet E.			<b>5d. PROJECT NUMBER</b>		
			<b>5e. TASK NUMBER</b>		
			<b>5f. WORK UNIT NUMBER</b>		
<b>7. PERFORMING ORGANIZATION NAMES(S) AND ADDRESS(S)</b> Air Force Institute of Technology Graduate School of Engineering and Management (AFIT/EN) 2950 Hobson Way, Building 640 WPAFB OH 45433-8865			<b>8. PERFORMING ORGANIZATION REPORT NUMBER</b>  AFIT/GAP/ENP/06-06		
<b>9. SPONSORING/MONITORING AGENCY NAME(S) AND ADDRESS(ES)</b> N/A			<b>10. SPONSOR/MONITOR'S ACRONYM(S)</b>		
			<b>11. SPONSOR/MONITOR'S REPORT NUMBER(S)</b>		
<b>12. DISTRIBUTION/AVAILABILITY STATEMENT</b>  APPROVED FOR PUBLIC RELEASE; DISTRIBUTION UNLIMITED					
<b>13. SUPPLEMENTARY NOTES</b>					
<b>14. ABSTRACT</b> Optical turbulence within earth's atmosphere plays a significant role in electromagnetic radiation propagation from a high energy laser. The index of refraction structure constant, Cn2, characterizes turbulent spatial fluctuations due to temperature gradients. These changes in the index of refraction affect the intensity of the laser wave front on its intended target. It is important to characterize this parameter throughout the atmosphere, the boundary layer and above, for its applications regarding the Airborne Laser (ABL) and the Advanced Tactical Laser (ATL). There are several ways to obtain values of optical turbulence, including standard and statistical models, physically-based numerical models, and climatological compilations of observed values. The purpose of this paper is to quantifiably compare standard, statistical, and numerical models of Cn2 to climatological values using the High Energy Laser End-to-End Operational Simulation (HELEEOS), to determine whether each model will yield values similar to that of measured optical turbulence data. The study shows that HELEEOS is a powerful tool in atmospheric optical turbulence prediction, not only because it has the capability to use standard optical turbulence profiles like Hufnagel-Valley 5/7 (HV 5/7), but it can incorporate correlated, climatologically-derived turbulence profiles—a technique specifically developed for HELEEOS. The comparative analysis in this research appears to validate the HELEEOS method for correlating climatological Cn2 to other meteorological parameters. Worldwide dwell time estimates vary more than 4 s for tactical low altitude oblique scenarios using this new technique compared to HV 5/7.					
<b>15. SUBJECT TERMS</b> Optical Turbulence, High Energy Lasers, Airborne Laser					
<b>16. SECURITY CLASSIFICATION OF:</b>			<b>17. LIMITATION OF ABSTRACT</b>	<b>18. NUMBER OF PAGES</b>	<b>19a. NAME OF RESPONSIBLE PERSON</b>
<b>a. REPORT</b>	<b>b. ABSTRACT</b>	<b>c. THIS PAGE</b>			<b>19b. TELEPHONE NUMBER (Include area code)</b>
U	U	U	UU	116	Fiorino, Steven T., Lt. Col., USAF (ENP) (937) 255-6565, ext 4506 (steven.fiorino@afit.edu)